#235140
P-100

A COMPUTATIONAL METHOD FOR THE PREDICTION OF THE THREE-DIMENSIONAL VISCOUS FLOW PRESSURE DISTRIBUTION OVER FINITE WINGS USING STRIP ANALYSIS

Gary Leonard Shubert

B.S. in Mechanical Engineering
Michigan State University
1974

A Thesis submitted to
the Faculty of
The School of Engineering and Applied Sciences
of the George Washington University in partial satisfaction
of the requirements for the degree of Master of Science

August 1976

ABSTRACT

A computational method for the prediction of the three-dimensional viscous-flow pressure distribution over finite wings has been developed. In this method, a three-dimensional potential-flow computer program was combined with a two-dimensional swept-wing viscous-flow computer program using strip analysis. A 1- by 3-meter semispan wing of taper ratio 1 with NACA 0012 sections was used as a test case for the method. An experiment was also performed as part of a larger investigation to provide surface pressure data for a comparison with the theoretical results.

Results of the investigation indicate, that by considering only camber effects in the airfoil modification technique, the strip method approached a limiting value of total normal-force coefficient in three iterations in the absence of flow separation. However, if flow separation did occur in the boundary-layer development calculations, the airfoil modification method proved to be inadequate.

Generally, if no separation of the flow occurred in the boundary-layer development calculations, the strip method demonstrated good agreement with experiment at the inboard semispan stations and approached a limiting value of total normal-force coefficient within three to five iterations.

ACKNOWLEDGEMENTS

The author wishes to acknowledge the aid and assistance of the National Aeronautics and Space Administration (NASA) in making this investigation possible. The advice and guidance of Messrs. Richard J. Margason, Jan R. Tulinius, Harry L. Morgan, Jr., and Long P. Yip, NASA, and John P. Campbell, George Washington University, are greatly appreciated. Frances E. Sabo deserves special thanks for her patience in typing this thesis.

TABLE OF CONTENTS

	Page
ABSTRACT	ii
ACKNOWLEDGEMENTS	iii
TABLE OF CONTENTS	iv
LIST OF TABLES	vi
LIST OF FIGURES	vii
LIST OF SYMBOLS	x
Chapter	
I. INTRODUCTION	1
II. METHOD OF ANALYSIS	4
Description of Strip Method	4
Limitations of Strip Method	8
III. EXPERIMENTAL INVESTIGATION	9
Test Procedure	9
Description of Model	9
IV. PRESENTATION OF RESULTS	11
V. RESULTS AND DISCUSSION	14
VI. CONCLUSIONS AND RECOMMENDATIONS	17
APPENDIX	
A - DESCRIPTION OF POTENTIAL-FLOW PROGRAM	19
B - DESCRIPTION OF VISCOUS-FLOW PROGRAM	24

Page

REFERENCES 32

TABLES 34

FIGURES 37

LIST OF TABLES

Table	
I	Design chordwise location of static pressure taps on semispan wing model.
II	Wing span and aspect ratio for semispan wing model at different sweep angles.
III	Spanwise location of static pressure tap rows on semispan wing model.

LIST OF FIGURES

Figure

1. Flow chart of strip method.
2. Coordinate system transformation for the interpolation of pressure coefficients.
3. Modification of airfoil due to boundary-layer displacement thickness.
4. Effect of camber and thickness on section normal-force coefficient for NACA 0012 airfoil.
5. Schematic drawing of semispan wing model.
6. Photograph of 1- by 3-meter semispan wing model in the Langley V/STOL tunnel.
7. Pressure distributions, displacement thickness and camber line developments for five iterations of the strip method. $\Lambda = 0°$, $\alpha = 2.53°$.
8. Total and section normal-force coefficients versus iteration number and semispan station, respectively. $\Lambda = 0°$, $\alpha = 2.53°$.
9. Pressure distributions, displacement thickness and camber line developments for five iterations of the strip method. $\Lambda = 0°$, $\alpha = 6.75°$.
10. Total and section normal-force coefficients versus iteration number and semispan station, respectively. $\Lambda = 0°$, $\alpha = 6.75°$.
11. Pressure distributions, displacement thickness and camber line developments for five iterations of the strip method. $\Lambda = 0°$, $\alpha = 8.85°$.

Figure

12. Total and section normal-force coefficients versus iteration number and semispan station, respectively. $\Lambda = 0°$, $\alpha = 8.85°$.

13. Pressure distributions, displacement thickness, and camber line developments for five iterations of the strip method. $\Lambda = 20°$, $\alpha = 6.76°$.

14. Total and section normal-force coefficients versus iteration number and semispan station, respectively. $\Lambda = 20°$, $\alpha = 6.76°$.

15. Pressure distributions, displacement thickness, and camber line developments for five iterations of the strip method. $\Lambda = 20°$, $\alpha = 8.84°$.

16. Total and section normal-force coefficients versus iteration number and semispan station, respectively. $\Lambda = 20°$, $\alpha = 8.84°$.

17. Pressure distributions, displacement thickness, and camber line developments for five iterations of the strip method. $\Lambda = 40°$, $\alpha = 2.48°$.

18. Total and section normal-force coefficients versus iteration number and semispan station, respectively. $\Lambda = 40°$, $\alpha = 2.48°$.

19. Pressure distributions, displacement thickness, and camber line developments for five iterations of the strip method. $\Lambda = 40°$, $\alpha = 6.65°$.

20. Total and section normal-force coefficients versus iteration number and semispan station, respectively. $\Lambda = 40°$, $\alpha = 6.65°$.

Figure

21. Pressure distributions, displacement thickness, and camber line developments for five iterations of the strip method. $\Lambda = 40°$, $\alpha = 8.73°$.

22. Total and section normal-force coefficients versus iteration number and semispan station, respectively. $\Lambda = 40°$, $\alpha = 8.73°$.

23. Wing planform divided into a typical source and vortex-lattice grid.

24. Vortex distribution on airfoil.

25. Flow about a multi-element infinite swept wing.

LIST OF SYMBOLS

AR	aspect ratio
[A]	aerodynamic influence matrix
b	panel span, m
c_f	local skin-friction coefficient
C, c	chord, m
C_{f_R}	resultant skin-friction coefficient
C_{f_1}	streamwise skin-friction coefficient
C_{f_2}	crossflow skin-friction coefficient
C_p,CP	pressure coefficient
C_n,CN	normal-force coefficient
CNTOT	total normal force coefficient
F	universal function of Curles laminar method
g	correction term to Thwaites laminar method
H	shape factor, δ^*/δ
H_1	shape factor, $(\delta - \delta^*)/\theta$
K	nondimensional pressure gradient parameter

M_∞	reference Mach number
0	origin
q	dynamic pressure, $\frac{1}{2}\rho U^2$, kN/m^2
R_θ	momentum thickness Reynolds number, $U\theta/\nu$
$R_{\theta_{ins}}$	streamwise momentum thickness Reynolds number at instability point
$R_{\theta_{trans}}$	streamwise momentum thickness Reynolds number at transition
$[S_x],[S_y]$	source influence matrix components
S	distance along a streamline, m
$[T_{T_y}]$	actual surface lateral tangent unit vector component matrix
U	local velocity , m/sec
U_S	local streamwise velocity , m/sec
V	total velocity in y direction, m/sec
$\bar{V}_x$	onset flow velocity in x direction, m/sec
V_∞	reference velocity, m/sec
X,Y,Z, x,y,z	global coordinates, m
x',y',z'	components of length in the normal chord, normal and spanwise directions , m

Y_c,CAMBER	camber, z/c
Z_c	perpendicular distance between chord line and mean camber line, m
Z_t	airfoil thickness, m
α,ALPHA	angle of attack, deg
β	angle of sideslip, deg
Γ	horseshoe vortex strength
γ	ratio of specific heats
δ	boundary-layer thickness, cm
δ^*,DELTA*	displacement thickness, cm
δ_2^*, θ_{12}, θ_{21},θ_{22}	three-dimensional boundary-layer thickness parameters defined in equations (31) and (33), cm
η,ETA	spanwise station, 2Y/b
θ	momentum thickness, cm
Λ	sweep angle, deg
ν	kinematic viscosity, m^2/sec

ρ	angle between streamline at outer edge of boundary layer and wing normal chord, deg, or density
Σ	source strength
ϕ	angle between surface streamline and external streamline directions, deg

Subscripts

ave	average value
i	iteration number
ins	instability
k	integer value
l,LO	lower
M	longitudinal direction
m	longitudinal subpanel number
n	lateral subpanel number
T	lateral direction
t	airfoil thickness
total,TOT	total value

trans	transition
u,UP	upper
X,Y,Z	directions
∞	infinity or free-stream value

CHAPTER I

INTRODUCTION

At present, there are several two- and three-dimensional swept-wing viscous-flow programs and several three-dimensional potential-flow programs available to the aerodynamicist (Refs. [1] to [4]). Such programs are being used for the design and analysis of finite wings. In the case of three-dimensional potential-flow programs, the viscous effects present in real fluid flow are not accounted for; therefore, these programs tend to overpredict the pressure distribution and hence the lift of the wing. Accurate prediction of the pressure distribution is necessary to compute the boundary-layer development and profile drag of the wing. Therefore, there has been increasing effort in recent years to develop techniques which will account for the viscous effects of the boundary layer on the pressure distribution.

One such technique is the combining of a two-dimensional swept-wing viscous-flow program with a three-dimensional potential-flow program utilizing a "strip method". The strip method involves computing the three-dimensional surface pressure distribution over a finite wing and then dividing it into a number of chordwise "strips." The surface pressure distribution for each strip is then used to drive the two-dimensional swept-wing viscous-flow program. Each strip is thus treated as an infinite wing. After the boundary-layer development for each

strip is calculated, a new airfoil geometry is determined using the resulting displacement thickness. It was Prandtl who first suggested modifying the airfoil geometry by adding the boundary-layer displacement thicknesses to the original geometry to account for the displacement of the potential-flow streamlines by the boundary layer. The new geometry of the various strips is then used as input to the three-dimensional potential-flow program to compute a new surface pressure distribution. This process can be repeated until convergence is obtained.

The objective of this investigation was to combine one such three-dimensional potential-flow program (Ref. [1]) and two-dimensional swept-wing viscous/potential-flow program (Ref. [2]) in a strip method. These two computer programs were selected because of their availability to the author and their computational efficiency.

An experiment was also performed as part of a larger investigation to provide experimental data for validating new three-dimensional viscous-flow methods (Ref. [5]).

In this experiment, a 1- by 3-meter semispan wing of taper ratio 1 with NACA 0012 sections was tested in the Langley V/STOL tunnel to measure the surface pressure distribution at several sweep angles through an angle-of-attack range of -6° to 20°. These experimental surface pressure distributions were used in this investigation as a means of verifying the strip method results.

During this investigation, an adequate convergence criterion was not established for the strip method; therefore, an arbitrary number of five iterations was performed and comparisons with the experimental

data were made. Results indicated that in most cases five iterations were more than enough to obtain good agreement with the data of Reference [5].

CHAPTER II

METHOD OF ANALYSIS

Description of the Strip Method

A flow chart for the strip method is given in Figure 1. User input data such as geometry and free-stream conditions are read in by the three-dimensional potential-flow program (DERIV) and stored off on random access files. A brief description of this program taken from Reference [1] is given in Appendix A. After the potential-flow pressure calculations are completed, stagnation point locations are calculated for each strip in subroutine STAG by simply scanning the pressure coefficients and determining the x/c location of the largest value. Because of the differing geometry requirements of DERIV and the viscous/potential-flow program (VIP) of Reference [2], the pressure coefficients must then be interpolated to obtain values perpendicular to the leading edge. This is accomplished in subroutine INTRP using conventional, first order, Lagrangian interpolation and a coordinate system transformation as shown in Figure 2. In the case of a configuration with zero sweep, INTRP is bypassed since the pressure distribution is already perpendicular to the leading edge. Section and total normal-force coefficients are then computed by integrating the pressure distributions. Integration is accomplished in subroutine INTEG using a cubic spline under tension. The pressure coefficients and x/c locations for the

various strips are then used as input to the integral boundary-layer calculation method (IBL) of VIP. A brief description of this program taken from Reference [2] is given in Appendix B. IBL then calculates the boundary-layer development perpendicular to the leading edge of the airfoil for each strip and subroutine PRINTER prints the resulting boundary layer, displacement, and momentum thickness developments, and shape factor, crossflow angles, skin-friction coefficient, and velocity profile developments versus x/c. Subroutine BLPLOT then plots the surface pressure distribution and upper and lower surface displacement thickness developments versus x/c.

The next four subroutines (INTRP1, GEOMAD, SMOOY, and GRADNT)deal with the computation of a modified airfoil geometry and constitute the most important step in the iterative process of the strip method. The selection of an adequate airfoil geometry modification method that will insure convergence in a reasonable number of iterations is of utmost importance in terms of computer time and efficiency. In this investigation, the airfoil geometry was modified by computing effective boundary-layer displacement thicknesses for each strip and then adding them to the original camber line of the strip. The effective boundary-layer displacement thicknesses, δ^*_{total}, were computed using the following proportioning technique to prevent over-correction during the initial iterations:

$$(\delta^*_{total})_i = (\delta^*_{ave})_i \qquad \text{for } i = 1 \tag{1}$$

$$(\delta^*_{total})_i = 2/3\ (\delta^*_{ave})_i + 1/3\ (\delta^*_{ave})_{i-1} \qquad \text{for } i = 2,3,4,\ldots \tag{2}$$

where

$$(\delta^*_{ave})_i = 1/2\ (\delta^*_u - \delta^*_\ell)_i \qquad \text{for } i = 1,2,3,... \qquad (3)$$

and i = iteration number.

The addition of the δ^*_{total}'s to the original camber line of each strip of the airfoil has the effect of "uncambering" the airfoil as shown in Figure 3. This uncambering effect can result in very steep, positive gradients of the camber line at the trailing edge. Because of this, the following formula was used to limit the slope of the camber line near the trailing edge:

$$\text{Camber slope limit} = .1875\ \alpha + .125 \qquad (4)$$

where α is the angle of attack in degrees. The boundary layer tends to produce the effect of uncambering and reducing the angle of attack of the section which decreases the lift. Also, the boundary layer tends to produce the effect of thickening the airfoil thereby causing an increase in local surface velocities. The magnitudes of these effects are shown in figure 4 where section normal-force coefficients for a NACA 0012 wing for a range of angle of attacks have been plotted. These values were obtained after five iterations of the two-dimensional, viscous-flow program of Reference [6]. This computer program uses a similar technique to modify the original airfoil to account for the viscous effects of the boundary layer and includes the perturbation velocity effects due to thickness as well as to lift. In Figure 4, the circles represent the potential-flow values of the section normal-force

coefficient, while the squares and diamonds represent the section C_N's considering only camber and camber plus thickness effects, respectively. It can be seen that the perturbation velocity due to the camber effects alone account for most of the sectional normal force. The effect of the boundary layer on the basic thickness of the NACA 0012 airfoil is thus of secondary importance and therefore was not included in the present investigation.

As shown in Figure 1, subroutine INTRP1 interpolates the displacement thicknesses to locations on the wing which are parallel to the free-stream flow, using first order Lagrangian interpolation. This interpolation is necessary to obtain values of the displacement thicknesses which are compatible with the geometry requirements of DERIV. Subroutine INTRP1 is divided into two parts. The first part takes the calculated values of the displacement thicknesses from IBL and interpolates to obtain values perpendicular to the leading edge at the user specified control point locations. The second part then interpolates these values to locations on the wing which are parallel to the free-stream flow direction. This second part is bypassed for a configuration with zero sweep. It should be noted that whenever any interpolation is performed the original x/c and spanwise spacing, input by the user, is preserved. After the displacement thicknesses have been interpolated to locations compatible with the geometry requirements of DERIV, subroutine GEOMAD is called and computes the δ^*_{total}'s for each strip at each of the specified x/c locations. These displacement thicknesses, which form the new camber lines of each strip of the airfoil, are then smoothed twice

using a standard least squares smoothing technique and plotted. Subroutine GRADNT then computes the slopes of the smoothed camber lines using finite difference techniques. The program then tests to see if the number of user-specified iterations have been completed. If they have not, the computed slopes for each camber line are used as the new geometry input to DERIV. All other geometry and free-stream flow information input by the user remains the same. The entire process is then repeated until the required number of iterations is completed.

Limitations of the Strip Method

Currently, this method is limited to configurations with one component (that is, no slats or flaps), although there are plans to extend its capability to include multi-element configurations using an alternate potential-flow program (Ref. [4]). The program is limited to angles of attack below that angle where turbulent separation occurs in the integral boundary-layer calculation method (approximately 10° at 40° sweep) and only one angle-of-attack case can be run at a time. Since this program is a pilot code to demonstrate the potential value of a strip method in predicting the three-dimensional flow properties of finite wings, the program has not been optimized, and consequently, it is inefficient and requires approximately 80 seconds of CPU time per iteration on the CYBER 175T computer. (This time is based on a configuration modeled with 20 chordwise subpanels and 10 spanwise subpanels.)

CHAPTER III

EXPERIMENTAL INVESTIGATION

Test Procedure

An experimental investigation (Ref. [5]) was conducted to provide pressure distributions on a 1- by 3-meter semispan wing with taper ratio of 1.0 at various sweep angles. The semispan pressure wing was tested in the Langley V/STOL tunnel at five different sweep angles (0° to 40°) and through an angle-of-attack range of -6° to 20°. Pressure data were obtained at 600 pressure tap locations with 60 pressure taps distributed at each of 10 spanwise stations. The semispan wing was tested at free-stream dynamic pressures of 1.44 kN/m^2 and 2.39 kN/m^2 with a corresponding Reynolds number based on a 1-meter chord of 3.36×10^6 and 4.27×10^6, respectively.

Description of Model

The semispan wing model was constructed with NACA 0012 airfoil sections. The NACA 0012 airfoil section was selected because of its good low- and high-speed performance characteristics and because of the available of additional test data over a wide range of test conditions (Refs. [7],[8],and [9]). Coordinates of the NACA 0012 are given in Reference [7] and are also presented in Table I at the design pressure tap locations. A schematic drawing of the model and support system is shown in Figure 5. The range of sweep angles, 0° to 40°, was made possible by

the movement in the pitch mechanisms of the model support system with the addition of one of two wedge blocks (12° or 33°) at the wing root. Values of wing span and aspect ratio for the wing at different sweep angles are presented in Table II. The wing slot inserts prevented flow through the reflection plate. The wing tips were kept parallel to the free stream as the wing was swept by attaching appropriate wing-tip fairing. These tip fairings did not contain static pressure taps.

The spanwise locations of the pressure taps are presented in Table III and were determined by the following equation for $\Lambda = 0°$:

$$\eta = .05 + .95 \cos\left[\frac{\pi(10-k)}{20}\right] \qquad 0 \leq k \leq 9 \tag{5}$$

where k is the station number starting near the wing root. This distribution allowed for a concentration of pressure taps at the outboard portion of the wing where the pressure gradients are the largest.

A circular reflection plate with a diameter of 3.05 m was added to the model to simulate a full-span wing and to shield the model from the influence of the tunnel wall boundary layer.

The wing model was fabricated by covering a solid aluminum spar with a fiber-glass skin. The pressure tubings were embedded in the fiber-glass skin and routed to a set of scanivalves attached to the sting mount below the reflection plate. A transition strip was installed on the upper and lower wing surfaces at 0.05 x/c. All theoretical results were tripped at the same x/c location. A photograph of the model in the Langley V/STOL tunnel is shown in Figure 6.

CHAPTER IV

PRESENTATION OF RESULTS

Theoretical boundary layer and surface pressure distributions were obtained for a 1- by 3-meter semispan wing with NACA 0012 airfoil sections over a range of sweep angles from 0° to 40° for an angle-of-attack range of 0° to 9°. Because of the large volume of data, only eight cases are presented with tabulated results omitted. These eight cases are compared with experimental results (Ref. [5]) and are presented as indicated in the following table:

Surface Pressure and Displacement Thickness Distributions						
Sweep Angle, deg	Angle of Attack, deg	q_∞ (kN/m^2)		M_∞		Figure
		Theory	Data	Theory	Data	
0	2.53,6.75 8.85	2.39	1.44	.18	.14	7,9,11
20	6.76,8.84	2.39	2.39	.18	.18	13,15
40	2.48,6.65 8.73	2.39	1.44	.18	.14	17,19,21

The theoretical value of the Reynolds number was 3.97×10^6 based on a wing chord of 1 meter.

The results are plotted using a format of four graphs per semispan station. The first graph is a plot of pressure coefficient versus x/c. Experimental values of pressure coefficient are plotted along with the theoretical values for five iterations. Below this graph, the displacement thickness developments for the upper and lower surfaces of the strip are plotted in terms of z/c versus x/c for five iterations. IBL calculates the displacement thickness development for each surface of each strip at 200 values of x/c. For purposes of graphical clarity, only every fourth point is plotted. The bottom graph is a plot of the camber line z/c values versus x/c location for six iterations. It should be mentioned that only the camber line is plotted for the sixth iteration as a further indication of the numerical stability or instability of the strip method. In the symbol key, the open circles represent the first iteration or potential-flow solution (that is, neglecting viscous effects), and the other symbols represent successive iterations which include the effects of the boundary layer. Due to the scale of the plotted results, the different symbols are difficult to distinguish.

A summary of the theoretical results is presented in the even-numbered figures 8 through 22 where the total value of the normal-force coefficient is plotted versus iteration number, and the normalized section normal-force coefficients are plotted for every iteration versus semispan location. Experimental results from Reference [5] are plotted on the latter graph for a comparison.

All results are plotted perpendicular to the leading edge of the wing. For a nonzero sweep case, the plotted values of pressure coefficient have been interpolated from their corresponding streamwise values using first order Lagrangian interpolation.

CHAPTER V

RESULTS AND DISCUSSION

In most cases presented, the strip method approached a limiting value of total normal-force coefficient after five iterations, and the final iteration results were not much different from the initial iteration results. In fact, the initial iteration results (that is, not including boundary-layer effects) agreed very well with the data in most cases. One reason for this may be due to the fact that the configuration run in the strip program was a symmetric airfoil with no twist, taper, etc. More complicated configurations (for example, a supercritical section) could very well yield more dramatic results. Another reason could be due to the linearized boundary conditions of the potential-flow program. This approximation results in a lower calculated value of the surface velocity which results in a lower value of the pressure coefficient. Figures 8, 10, 12, 14, 16, 18, 20, and 22, where the total normal-force coefficient is plotted versus iteration number, demonstrate that the strip method approached a limiting value of C_N after three iterations in most cases. However, in the absence of flow separation in the boundary-layer development calculations, the strip method approached a limiting value of C_N even sooner (Fig. 22). If separation does occur, the displacement thicknesses must be extrapolated to the trailing edge. This can lead to unpredictable

camber line calculations and oscillating pressure distributions. This effect can be clearly seen in Figures 7(g), 7(h), 9(d), 9(e), 11(g), 11(h), and 13(d) where separation is evident in the random values of the displacement thicknesses near the trailing edge. Since the airfoil modification method employs a proportioning technique using present and previous iteration values of the displacement thicknesses, this effect can be transmitted to succeeding iterations and is evident in the previously mentioned figures.

Poor agreement with experiment in section normal-force coefficient as computed by the strip method for cases with 40° sweep (Figs. 18, 20, and 22) can be attributed to the interpolation of the pressure coefficients. In all cases, the experimental section normal force is decreased near the root by the ineffectiveness of the reflection plate. This result indicates that the reflection plate was not large enough to fully reflect the properties of a full-span wing. The wing-tip vortex flow is evident from the increase in trailing-edge suction pressure in the experimental surface pressure data in Figures 9(h) and 11(h).

Poor agreement with experiment in surface pressure distributions as computed by the strip method at low angles of attack can be attributed to the inaccuracy of the potential-flow program in taking into account the spanwise component of flow near the leading edge (Fig. 17).

Generally, if no separation of the flow occurred in the boundary-layer development calculations, the strip method demonstrated good agreement with experiment at the inboard semispan stations and approached a limiting value of total normal-force coefficient within three to five iterations.

CHAPTER VI

CONCLUSIONS AND RECOMMENDATIONS

A computational method for the prediction of the three-dimensional viscous-flow pressure distribution over finite wings has been developed. A 1- by 3-meter semispan wing of taper ratio 1 with NACA 0012 sections was used as a test case for the method. An experiment was also performed as part of a larger investigation to provide data for a comparison with the theoretical results. Results of the investigation indicate, that by considering only camber effects in the airfoil modification technique, the strip method approached a limiting value of total normal-force coefficient in three iterations in the absence of flow separation. However, if flow separation did occur, the airfoil modification method proved to be inadequate. Two possible solutions to this problem are: (1) modifying the integral boundary-layer calculation method to compute through separation to the trailing edge and (2) devising a new airfoil modification method altogether. One such alternate method would be the calculation of a source distribution as a function of the displacement thicknesses to represent the boundary layer. This approach has the added advantage of being computationally faster than the method used in this investigation.

In the future, any strip method should use potential- and viscous-flow programs that have similar geometry input so that no interpolation of the input and output is necessary. Execution time and overall

accuracy of the results would thus be enhanced. A potential-flow program such as Reference [4] would also be much better because it satisfies the boundary conditions on the surface of the airfoil instead of on the chordal plane.

The stagnation point location technique in the strip method is very dependent on the number of chordwise control points used to solve for the boundary conditions. Therefore, a more accurate technique should be devised. Adequate convergence criterion also needs to be defined. Testing the difference in total normal-force coefficient for two successive iterations and setting a lower limit on this difference is one such criterion that may be promising.

APPENDIX A

DESCRIPTION OF THE POTENTIAL-FLOW PROGRAM

General Description

The potential-flow program of Reference [1] is an analysis method for the prediction of the static and rotary stability derivatives for a complete airplane configuration. The perturbation flow about the configuration is represented by a grid of quadrilateral vortex and horseshoe vortex and source singularities. Surface pressures and integrated section and total loads and moments are computed. Subcritical compressibility is accounted for by means of the Goethert similarity rule.

A smaller version of this program, for the computation of the surface pressure distribution over a wing only, was used in the present investigation since the study of the flow over finite wings and computing efficiency were of prime interest. Because of this, only the method and features of the program relating to the potential-flow pressure distribution calculations over a finite wing will be discussed. The program is primarily written in FORTRAN IV (several sections are written in Compass Assembly language to minimize CPU time) for the CDC 6000 series computers. It uses 71,000 octal words of storage and operates in the overlay mode.

Wing Alone Version Description

The wing is divided into a number of subpanels with a typical source and vortex lattice grid as shown in Figure 23. Wing singularities are placed on the chordal plane instead of the external surface of the wing.

After the coordinates of the subpanel corner points are calculated, the coordinates of the source and vortex lattices, used to represent the perturbation velocity due to thickness and lift, respectively, are determined. The wing bound vortices and control points are placed on the quarter and three-quarter chord of the subpanels, respectively. The trailing edges of the horseshoe vortices are placed along the subpanel side edges and are straight lines in the X-direction going off to infinity. The source strengths Σ are defined by the change in thickness over that portion of the subpanel it represents, so that

$$\frac{\Sigma}{V_\infty} = \frac{2\sqrt{1-M_\infty^2}\; Z_t}{\sqrt{\dfrac{1+(\tan\Lambda)^2}{1-M_\infty^2}}} \frac{\bar{V}_X}{V_\infty} \tag{6}$$

where Λ is the sweep of the source line and $\bar{V}_X$ is the total free-stream onset velocity in the X-direction. The horseshoe vortex strengths Γ must be solved for utilizing the boundary condition that a minimum of flow passes through the chordal surface of the wing panel at a finite number of control points. In order to satisfy this boundary condition, the total flow due to all the singularities and the free-stream onset flow is summed at each control point, and the scalar product of this sum is minimized. This results in a set of linear aerodynamic influence equations which are solved for the unknown vortex strengths using Householder's method.

The influence equations are given by:

$$\left[A\right] \left\{\frac{\Gamma}{V_\infty}\right\} - \left[\alpha\right] = \left\{e\right\} \tag{7}$$

where [A] is the aerodynamic influence matrix. The vector {e} is the flow through the mean camber surface of the wing at the control points. This vector is zero for a discrete point solution (same number of unknowns as equations). Each element of the above aerodynamic influence matrix is associated with the influence of a singularity on a control point. The singularities and control points are ordered such that all of the longitudinal stations for the first lateral station are considered first, and then all the longitudinal stations for the second lateral station are considered second, etc. The longitudinal stations start at the leading edge of the wing and go toward the trailing edge; the lateral stations start at the root of the wing and go toward the tip.

The velocity tangent to the wing surface in the longitudinal direction is given by:

$$\left(\frac{V_M}{V_\infty}\right)_{mn} = \left[\frac{1}{\left[1 + (1+\tan^2\Lambda)_{mn}\left(\frac{dZ_T}{dx} \pm \frac{dZ_C}{dx}\right)^2_{mn}\right]^{1/2}}\right]\left[\frac{1}{(1-M_\infty^2)}\left[S_X\right]\left\{\frac{\Sigma}{V_\infty}\right\}\right]$$
$$\pm \frac{1}{(1-M_\infty^2)}\left[\left(\frac{\Delta V_M}{V_\infty}\right)_{mn}\right]\left[(1) + \left[\sqrt{1+\tan^2\Lambda_{mn}}\right]\left[S_X\right]\left[\left\{\frac{\Sigma}{V_\infty}\right\} - \left\{\frac{\Sigma'}{V_\infty}\right\}\right]\right] \tag{8}$$

where

$$\left(\frac{\Delta V_M}{V_\infty}\right)_{mn} = \left[\frac{\frac{\Gamma_{b_{mn}}}{V_\infty}}{\frac{3}{4}\,\bar{\ell}_{M_{(m-1)n}} + \bar{\ell}_{M_{mn}} + \frac{1}{4}\,\bar{\ell}_{M_{(m+1)n}}}\right]\left[\frac{\bar{\ell}_{M_{mn}} + \bar{\ell}_{M_{(m+1)n}}}{3\,\bar{\ell}_{M_{mn}} + \bar{\ell}_{M_{(m+1)n}}}\right] + \left[\frac{\left(\Gamma_{b_{(M+1)}}\right)/V_\infty}{\frac{3}{4}\,\bar{\ell}_{M_{mn}} + \bar{\ell}_{M_{(m+1)n}} + \frac{1}{4}\,\bar{\ell}_{M_{(m+2)n}}}\right]\left[\frac{2\,\bar{\ell}_{M_{mn}}}{3\,\bar{\ell}_{M_{mn}} + \bar{\ell}_{M_{(m+1)n}}}\right] \tag{9}$$

$$\frac{\Sigma'}{V_\infty} = \left[\frac{\frac{Z_T}{C}}{(X/C)\,(1-X/C)}\right]\left[\frac{\frac{\bar{V}_X}{V_\infty}}{\sqrt{1 + \frac{\tan^2\Lambda}{(1-M_\infty^2)}}}\right]\frac{\bar{\ell}_M}{2} \tag{10}$$

and where X/C is the local percent chord and $\bar{\ell}_M$ is the length of the subpanel in the longitudinal direction.

The velocity tangent to the wing surface in the lateral direction is given by:

$$\left(\frac{V_T}{V_\infty}\right)_{mn} = \left[\frac{1}{\left(1 + (1+\tan^2\Lambda)_{mn}\left(\frac{dZ_t}{dx} \pm \frac{dZ_c}{dx}\right)^2_{mn}\right)^{1/2}}\right]\left\{\frac{1}{\sqrt{1-M_\infty^2}}\left[T_{T_Y}\right]\left[S_Y\right] \pm \frac{1}{\sqrt{1-M_\infty^2}}\left[\left(\frac{\Delta V_T}{V_\infty}\right)_{mn}\right]\left[\{1\} + \left[\sqrt{1+\tan^2\Lambda_{mn}}\right]\left[T_{T_Y}\right]\left[S_Y\right]\left[\left\{\frac{\Sigma}{V_\infty}\right\} - \left\{\frac{\Sigma'}{V_\infty}\right\}\right]\right]\right\} \tag{11}$$

where $[S_X]$ and $[S_Y]$ are the influence matrices defined by the components of perturbation velocity induced by the unit strength sources in the X- and Y-directions, respectively, and

$$\left(\frac{\Delta V_T}{V_\infty}\right)_{mn} = \frac{1}{2}\left[\frac{\frac{\Gamma_{T_m}\left(n - \frac{\Delta n}{2}\right)}{V_\infty}}{\left(\bar{\ell}_{T_{mn}} + \bar{\ell}_{T_{m(n-1)}}\right)} + \frac{\frac{\Gamma_{T_m}\left(n + \frac{\Delta n}{2}\right)}{V_\infty}}{\left(\bar{\ell}_{T_{mn}} + \bar{\ell}_{T_{m(n+1)}}\right)}\right] + \left[\left(\frac{\Delta V_M}{V_\infty}\right) \tan\Lambda\right]_{mn} \tag{12}$$

where $\bar{\ell}_T$ is the length of the subpanel in the lateral direction.

Note, in equations (8) and (11), the top sign is used to compute the velocity on the upper surface and the bottom sign the lower surface in those terms which have a plus and minus in front.

The surface pressure coefficients at each of the control points on the wing are then computed using the following expression:

$$C_{P_{mn}} = \frac{2}{\gamma M_\infty^2}\left[\left\{1 + \frac{\gamma-1}{2} M_\infty^2 \left[1 - \left(\frac{V_M}{V_\infty}\right)_{mn}^2 - \left(\frac{V_T}{V_\infty}\right)_{mn}^2\right]\right\}^{\frac{\gamma}{(\gamma-1)}}\right] \tag{13}$$

where γ is the ratio of specific heats.

APPENDIX B

DESCRIPTION OF THE VISCOUS-FLOW PROGRAM

General Description

The viscous/potential-flow program of Reference [2] is composed of a two-dimensional, boundary-layer segment and a two-dimensional potential-flow segment. A brief description of the complete program will be given followed by a detailed description of the two-dimensional, integral approach used in the viscous-flow segment since this approach was used in the present investigation.

The program can handle at most a configuration composed of four elements (that is, a slat, main component, and at most two flaps, slotted or unslotted). All program input and output are in the normal chord direction, that is, perpendicular to the leading edge.

The two-dimensional potential-flow segment employs a vortex-lattice surface singularity technique. The airfoil is approximated by a number of planar segments with the endpoints located on the actual airfoil surface. A triangular distribution of vorticity is then placed on the upper and lower surfaces as indicated in Figure 24 (taken from Ref. [2]).

The viscous-flow segment uses either a finite differencing or integral boundary-layer technique depending on the configuration region. The boundary-layer development of the main component and all lower surfaces are computed using an integral approach, while slot regions are

computed via finite difference methods as shown in Figure 25 (taken from Ref. [2]). The viscous/potential-flow interaction is accomplished by calculating a source distribution as a function of the displacement thicknesses and pressure distribution. This source distribution is then included in the second calculation of the potential flow and represents the effect of the boundary layer in the modification of the potential flow. This procedure is repeated until convergence is obtained.

The program is written in FORTRAN IV for the CDC 6600 and 7600 series of computers. It uses 100,000 octal words of storage and operates in the overlay mode.

Integral Boundary-Layer Method Description

The boundary-layer development is calculated from the stagnation line back to the trailing edge for each surface of the configuration and is divided thus: (A) Laminar Development, (b) Instability and Transition Calculations, and (c) Turbulent Development.

Laminar Development. - The laminar boundary-layer calculation is a modified Thwaites method (Ref. [10]) using a two-dimensional integral approach along external streamlines. In Thwaites method, the momentum integral equation

$$d\theta/dx' = C_f/2 - (H + 2)\ \theta/U\ (dU/dx') \tag{14}$$

is written in the form:

$$d/dx'\ (K/U) = L/U \tag{15}$$

where

$$K = \theta^2/\nu \, (dU/dx')$$
$$L = [\ell - K \, (H + 2)] \tag{16}$$
$$\ell = \theta/U \, (\partial U/\partial y')\big| \, y = 0$$

To determine the relationship between L and K, Thwaites used exact solutions to a variety of laminar flows to obtain

$$L = 0.45 - 6K \tag{17}$$

Curle (Ref. [11]) suggested a modification of equation (17) since it was shown to be inadequate in flows approaching separation:

$$L = 0.45 - 6.K + g(K,\mu) \tag{18}$$

where

$$\mu = K^2 \, U \, (d^2 U/dx'^2)/(dU/dx')^2 \tag{19}$$

If equation (18) is substituted into equation (15) and integrated, the following is obtained

$$\theta^2 = 0.45 \, \nu/U^6 \int_0^x (1 + 2.22g) \, U^5 \, dx' \tag{20}$$

With g initially equal to zero, equation (20) is easily solved by iteration. At each step of the calculation, the shape factor H can be determined using equation (16). Then with the aid of equation (20), the displacement thicknesses can be calculated by

$$\delta^* = H\theta \tag{21}$$

The calculations proceed until laminar separation occurs or until the end of the airfoil is reached. The boundary-layer development is then searched to determine if transition or separation has occurred, in which case the flow is assumed to be turbulent.

Instability and Transition Calculations. - Boundary-layer instability and transition are not well understood, and there is as yet no reliable theoretical method for their prediction. It is known, however, that a boundary layer becomes unstable when small disturbances are permitted to grow. The amplication of these disturbances causes the flow to become turbulent. Granville (Ref. [12]) has developed an empirical procedure based on determining the neutral stability and transition points. The neutral stability point is defined as that point downstream of which small disturbances are amplified within the boundary layer. This point is reached when the Reynolds number based on local flow properties reaches some critical value R_{INS}. Schlicting and Ulrich (Ref. [13]) have correlated R_{INS} with the local pressure gradient parameter

$$K = \theta^2/\nu \, (dU/dS) \tag{22}$$

Correlations of K by Smith (Ref. [14]) and others were reduced to analytical form as follows:

$$K = -0.4709 + 0.11066/\ln R_\theta - 0.0058591/\ln^2 R_\theta$$

$$\text{for} \quad 0 < R_{\theta_{INS}} \leq 650 \tag{23}$$

$$K = 0.69412 - 0.23992/\ln R_\theta + 0.0205/\ln^2 R_\theta$$

$$\text{for } 650 < R_{\theta_{INS}} \leq 10{,}000 \qquad (24)$$

For a given R_θ, if the calculated value of K is greater than that determined by the boundary-layer development, the flow has passed from a stable to an unstable region and the transition process begins.

Granville has developed a similar correlation to determine the transition point by defining an average pressure gradient parameter

$$\overline{K} = \frac{\int_{S_{ins}}^{S_{trans}} K dS}{S_{trans} - S_{ins}} \qquad (25)$$

or expressed analytically:

$$\overline{K} = -0.0925 + 7.0 \times 10^{-5} R_\theta \quad \text{for } 0 < R_{\theta_{trans}} \leq 750 \qquad (26)$$

$$\overline{K} = -0.12571 + 1.14286 \times 10^{-4} R_\theta \quad \text{for } 750 < R_{\theta_{trans}} \leq 1100 \qquad (27)$$

and

$$\overline{K} = 1.59381 - 0.45543/\ln R_\theta + 0.032534/\ln^2 R_\theta \qquad (28)$$

$$\text{for } 1100 < R_{\theta_{trans}} \leq 3000$$

When the calculated value of $\overline{K}$ for a given R_θ is greater than that value given by the boundary-layer development, transition is predicted and the turbulent boundary-layer calculations begin.

Turbulent Development. - The turbulent boundary-layer calculation method is the method of Cumpsty and Head (Ref. [15]). This method uses an orthogonal curvilinear system of coordinates based on the projection of external streamlines on the surface of the airfoil. In this system, streamwise turbulent boundary-layer profiles resemble two-dimensional profiles. Therefore, when the streamwise profiles are known, the crossflow profiles can be determined as functions of the streamwise profiles and the angle between the surface streamline and the projection of the external streamline on the surface (the angle ϕ).

Cumpsty and Head wrote the streamwise and crossflow momentum equations as follows:

Streamwise Momentum Equation

$$\frac{\partial \theta_{11}}{\partial s} - k\frac{\partial \theta_{12}}{\partial s} + \frac{1}{U_s}\frac{\partial U_s}{\partial s}(2 + H)\,\theta_{11} - \frac{\partial \rho}{\partial s}(\theta_{11} - \theta_{22})\,k = \frac{C_{f_1}}{2} \qquad (29)$$

Crossflow Momentum Equation

$$\frac{\partial \theta_{21}}{\partial s} - k\frac{\partial \theta_{22}}{\partial s} + \frac{2}{Us}\frac{\partial U_s}{\partial s}\theta_{21} - \frac{k}{U_s}\frac{\partial U_s}{\partial s}\{\theta_{11}(H+1) + \theta_{22}\} - 2k\frac{\partial \rho}{\partial s}\theta_{21} = \frac{C_{f_2}}{2} \qquad (30)$$

where $k = \tan\rho$, and

$$\theta_{12} = \theta_{11}\,J(H)\,\tan\phi\,;\; J(H) = -(H + H_1)\left[\frac{1}{H} - \frac{4}{H+1} + \frac{1}{H+2} + \frac{4}{H+3} - \frac{2}{H+5}\right]$$

$$\theta_{21} = \theta_{11}\,E(H)\,\tan\phi;\; E(H) = -(H + H_1)\left[\frac{1}{H} - \frac{2}{H+1} + \frac{1}{H+2}\right]$$

$$\theta_{22} = \theta_{11}\,C(H)\,\tan\phi;\; C(H) = -(H + H_1)\left[\frac{1}{H} - \frac{4}{H+1} + \frac{6}{H+2} - \frac{4}{H+3} + \frac{1}{H+4}\right] \qquad (31)$$

This system of equations contains more unknowns than equations; hence further relationships are required.

The needed relationships are obtained by using Cumpsty and Head's entrainment equation:

$$\frac{\partial(\delta-\delta_1^*)}{\partial s} + k\frac{\partial \delta_2^*}{\partial s} = F(H_1) + (\delta-\delta_1^*)\left(k\frac{\partial \rho}{\partial s} - \frac{1}{U_s}\frac{\partial U_s}{\partial s}\right) \tag{32}$$

where $H_1 = (\delta-\delta^*_1)/\theta_{11}$

$$\delta_2^* = \theta_{11}\, D(H)\, \tan\phi \quad ; \quad D(H) = -(H + H_1)\left[\frac{2}{H+1} - \frac{4}{H+3} + \frac{2}{H+5}\right]$$

$$F(H_1) = \exp\left[-3.512 - 0.617 \ln (H_1 - 3)\right], \tag{33}$$

and Thompson's two parameter skin-friction law (Ref. [16]):

$$C_{f_1} = f(H, R_\theta) \tag{34}$$

and is given by

$$C_{f_1} = \exp(A + HB) \tag{35}$$

where

$$A = 0.01952 - 0.3868\, Z + 0.02834\, Z^2 - 0.0007\, Z^3$$

$$B = 0.19151 - 0.8349\, Z + 0.06259\, Z^2 - 0.001953\, Z^3$$

$$Z = \ln R_\theta \tag{36}$$

The crossflow skin-friction coefficient C_{f_2} is then determined from the streamwise skin-friction coefficient C_{f_1} by

$$C_{f_2} = C_{f_1} \tan\phi \tag{37}$$

and the resultant skin-friction coefficient C_{f_R} by

$$C_{f_R} = \frac{C_{f_1}}{\cos\phi} \tag{38}$$

With the initial values of θ_{11} and H_1 known from the laminar equations or stagnation line initial conditions, equations (29), (30), and (32) are then integrated. The calculation procedure continues until the sum of the angles ρ and ϕ reaches 90°. The angle ρ is defined as the angle between the external streamline and wing normal chord. The angle ϕ, as previously defined, is the angle between the surface streamline and the projection of an external streamline on the surface of the airfoil. When the sum of ρ and ϕ reaches 90°, the flow is completely spanwise, and by definition, separation has occurred. The calculations are then stopped and a message is printed indicating the occurence of turbulent separation.

REFERENCES

[1] Tulinius, J., Clever, W., Niemann, A., Dunn, K., and Gaither, B. Theoretical Prediction of Airplane Stability Derivatives at Subcritical Speeds. NACA CR 132681, 1975

[2] Dvorak, F. A., and Woodward, F. A. A Viscous/Potential Flow Interaction Analysis Method for Multi-Element Infinite Swept Wings. NASA CR 2476, 1974

[3] Cebici, T., Kaups, K., Ramsey, J., and Moser, A. "Calculation of Three-Dimensional Compressible Boundary Layers on Arbitrary Wings." NASA SP 347, pt. 1, 1975, pp. 41-76

[4] Hess, J. Calculation of Potential Flow About Arbitrary Three-Dimensional Lifting Bodies. Rep. No. MDC J5679-01, McDonnell-Douglas Co., 1972

[5] Yip, L. P., and Shubert, G. L. Pressure Distributions on a 1- by 3-Meter Semispan Wing at Sweep Angles from 0° to 40° in Subsonic Flow. NASA TN D-8307, 1976

[6] Smetana, F. O., Summey, D. C., Smith, N. L., and Carden, R. K. Light Aircraft Lift, Drag, and Moment Prediction - A Review and Analysis. NASA CR 2523, 1975

[7] Abbott, I. H., and von Doenhoff, A. E. Theory of Wing Sections. Dover Publications, Inc., New York, 1959

[8] Gregory, N., and Wilby, P. G. NPL 9615 and NACA 0012 - A Comparison of Aerodynamic Data. C.P. No. 1261, Brit. A.R.C., 1973

[9] Gregory, N., and O'Reilly, C. L. Low-Speed Aerodynamic Characteristics of NACA 0012 Aerofoil, Including the Effects of Upper-Surface Roughness Simulating Hoar Frost. R&M No. 3726, Brit. A.R.C., 1973

[10] Thwaites, B. "Approximate Calculation of the Laminar Boundary Layer." Aeronaut. Quart., vol. 1, 1949, pp. 245-280

[11] Curle, N. "A Two Parameter Method for Calculating the Two-Dimensional Incompressible Laminar Boundary Layer." J. Roy. Aeronaut. Soc., vol. 71, Feb. 1967, pp. 117-123

[12] Granville, P. S. The Calculation of the Viscous Drag of Bodies of Revolution. David W. Taylor Model Basic Rep. 849, 1953

[13] Schlichting, H., and Ulrich, A. "Zur Berechnung des Umschlages Laminar-Turbulent (On the Calculation of Laminar-Turbulent Transition)." Jahrbuch 1942 der Deutchen Luftfahrt-Forschung, 1942, pp. 8-35

[14] Smith, A. M. O., and Gamberoni, N. Transition, Pressure Gradient and Stability Theory. Rep. No. ES 26388, Douglas Aircraft Co., Aug. 1956

[15] Cumpsty, N. A., and Head, M. R. "The Calculation of Three Dimensional Turbulent Boundary Layers, Pt. 1: Flow Over the Rear of an Infinite Swept Wing." Aeronau. Quart., vol. 18, Feb. 1967, pp. 55-84

[16] Thompson, B. G. J. A New Two Parameter Family of Mean Velocity Profiles for Incompressible Turbulent Boundary Layers on Smooth Walls. R&M No. 3463, Brit. A.R.C., 1965

TABLE I

DESIGN CHORDWISE LOCATION OF STATIC PRESSURE TAPS

ON SEMISPAN WING MODEL

x/c	z/c Upper Surface	z/c Lower Surface
0.0	0.0	0.0
.001938	.007786	-.007786
.005101	.012371	-.012371
.008412	.015751	-.015751
.012003	.018643	-.018643
.015533	.021081	-.021081
.020164	.023692	-.023692
.026691	.026927	-.026927
.043449	.033474	-.033474
.068029	.040393	-.040393
.096415	.046215	-.046215
.127694	.050912	-.050912
.161629	.054573	-.054573
.197963	.057260	-.057260
.236335	.059018	-.059018
.276981	.059893	-.059893
.319422	.059933	-.059933
.363751	.059168	-.059168
.410335	.057631	-.057631
.458507	.055365	-.055365
.508984	.052366	-.052366
.561119	.048693	-.048693
.615491	.044342	-.044342
.671552	.039352	-.039352
.728190	.033838	-.033838
.785998	.027770	-.027770
.843881	.021246	-.021246
.900483	.014420	-.014420
.956240	.007242	-.007242
.99619	.001260	-.001260
1.0000	0.0	0.0

TABLE II

Wing Span and Aspect Ratio for Semispan Wing Model at Different Sweep Angles

Sweep	b/2, m	AR
0^0	2.95	5.90
10^0	2.98	5.87
20^0	2.91	5.47
30^0	2.83	4.90
40^0	2.53	3.88

TABLE III - Spanwise Location of Static Pressure Tap Rows On Semispan Wing Model

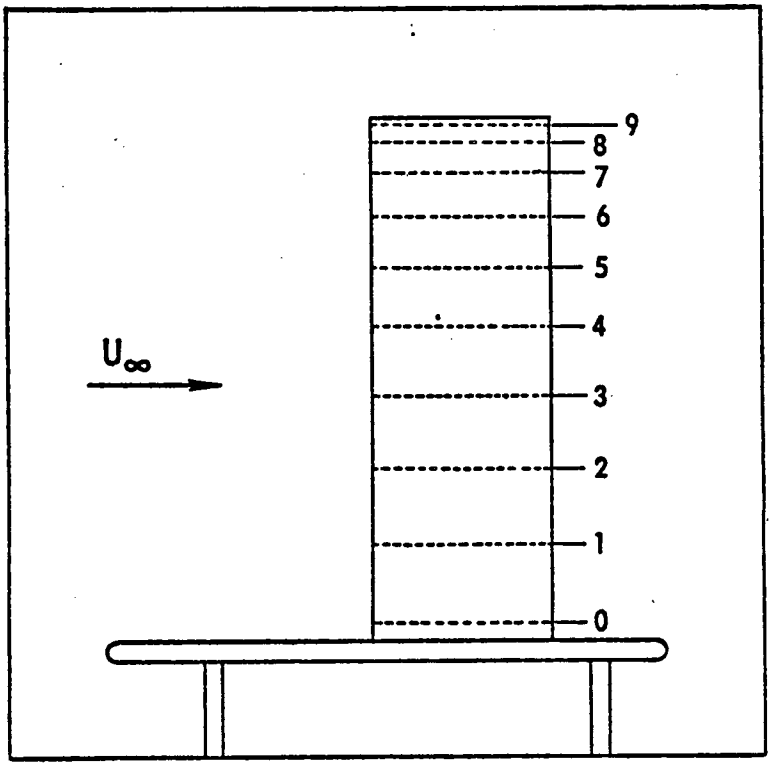

Pressure station	$\eta(\Lambda = 0^0)$
0	.05
1	.1986
2	.3436
3	.4813
4	.6084
5	.7218
6	.8186
7	.8965
8	.9539
9	.9883

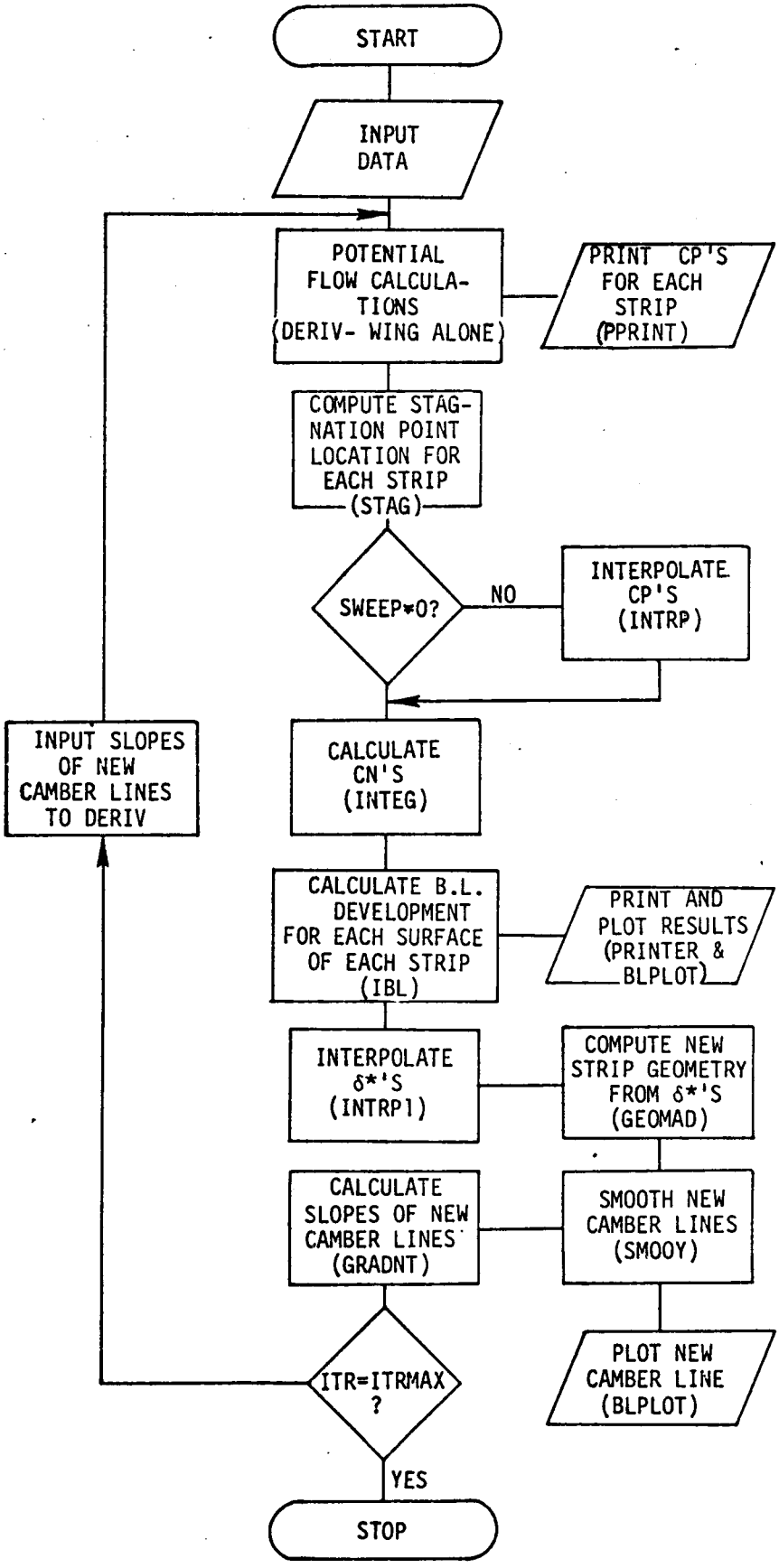

Figure 1. - Flow chart of strip method.

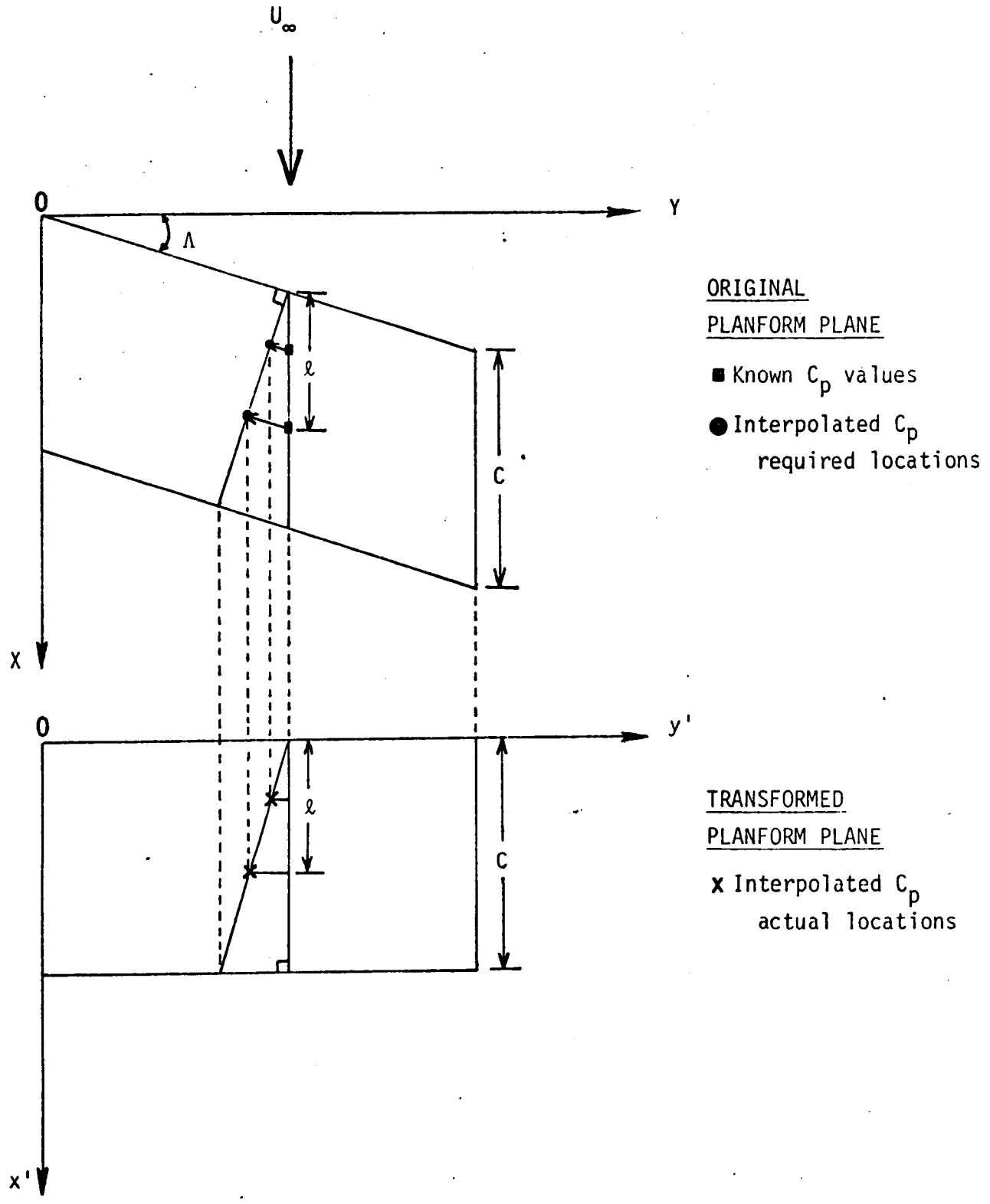

Figure 2. - Coordinate system transformation for the interpolation of pressure coefficients.

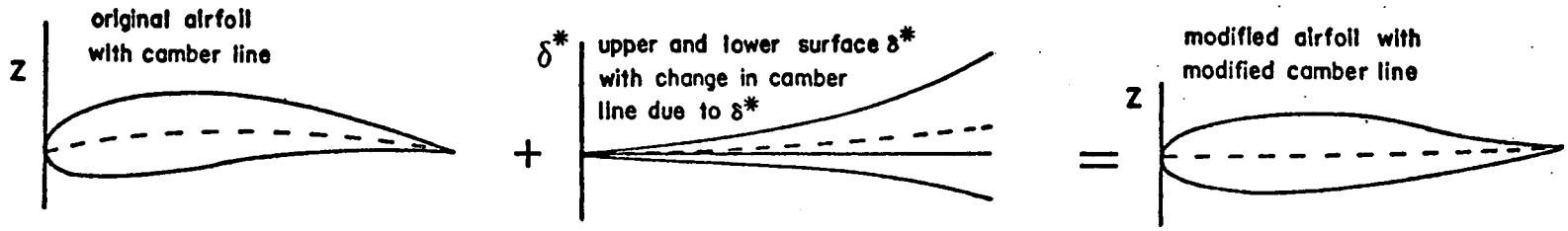

Figure 3. - Modification of airfoil due to boundary-layer displacement thickness.

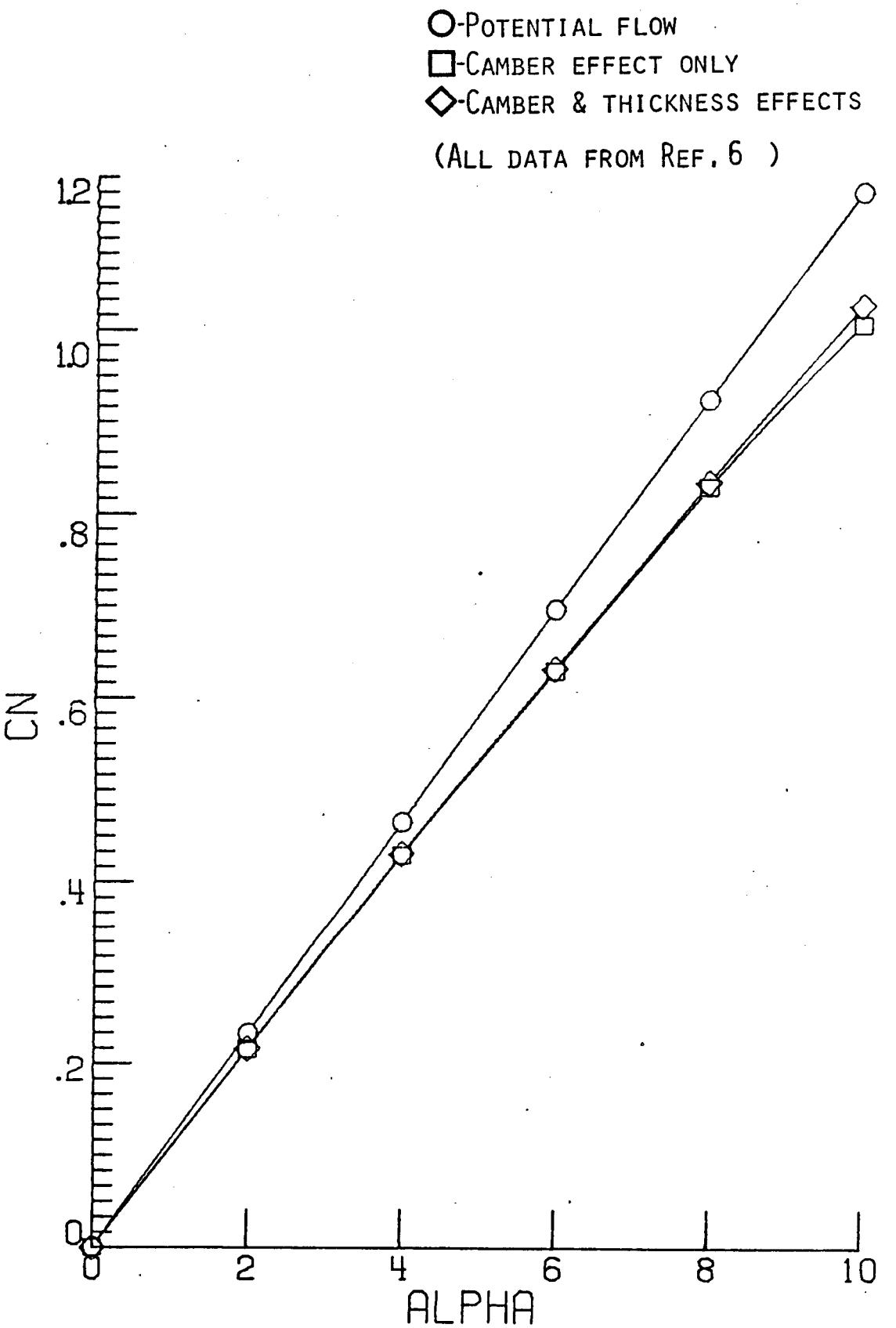

Figure 4. - Effect of camber and thickness on section normal force coefficient for NACA 0012 airfoil.

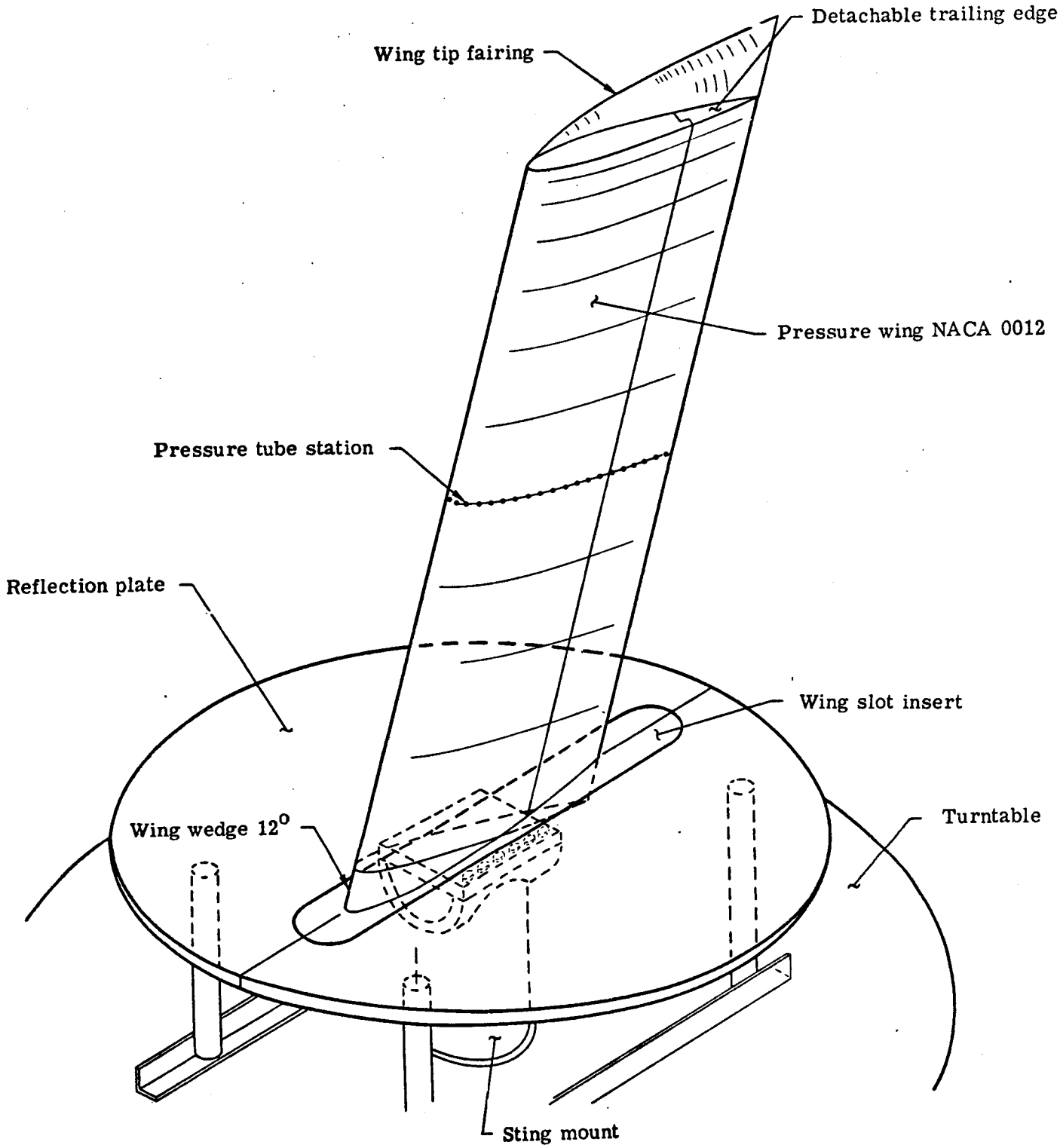

Figure 5. - Schematic drawing of semispan wing model.

NASA
L-75-3700

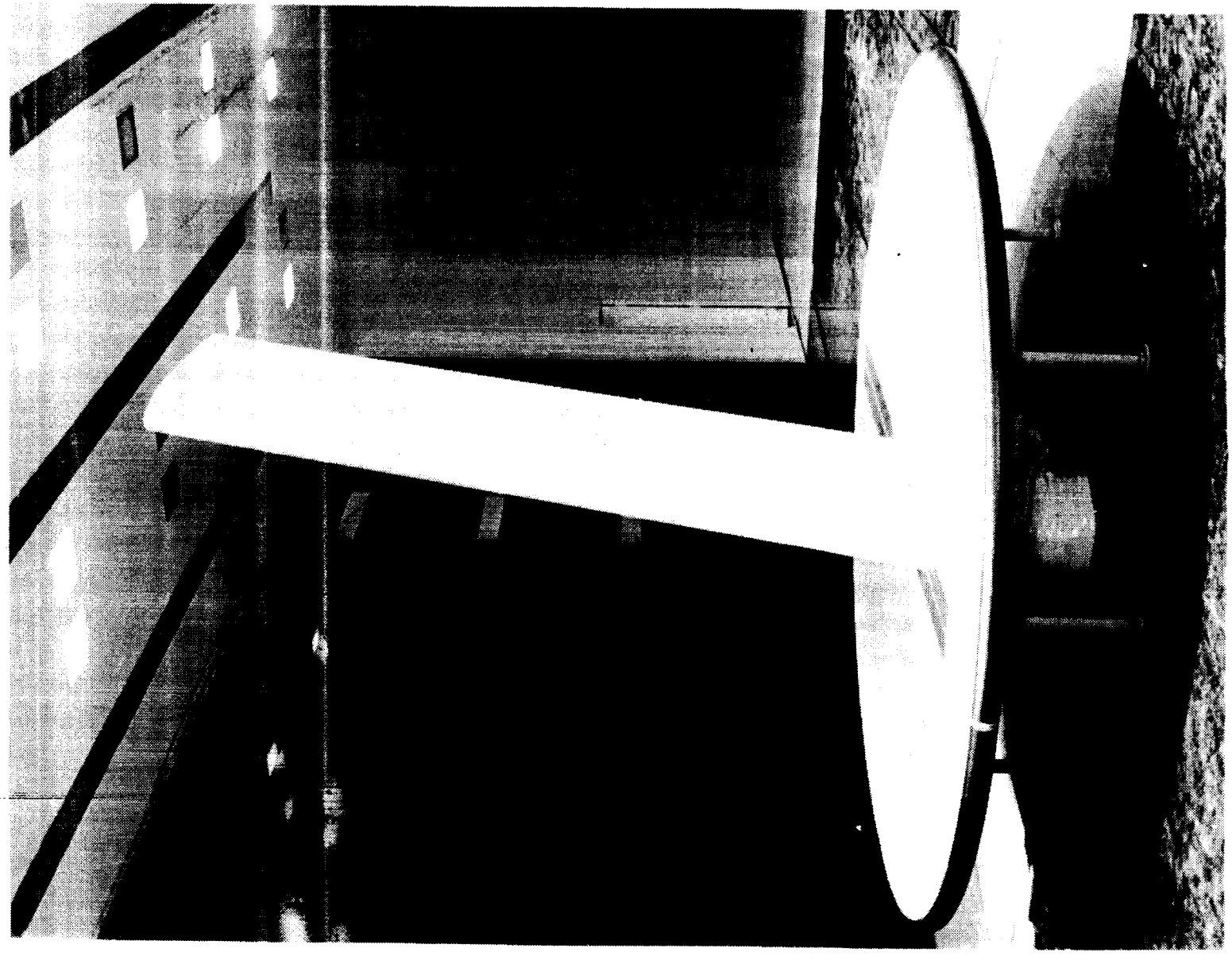

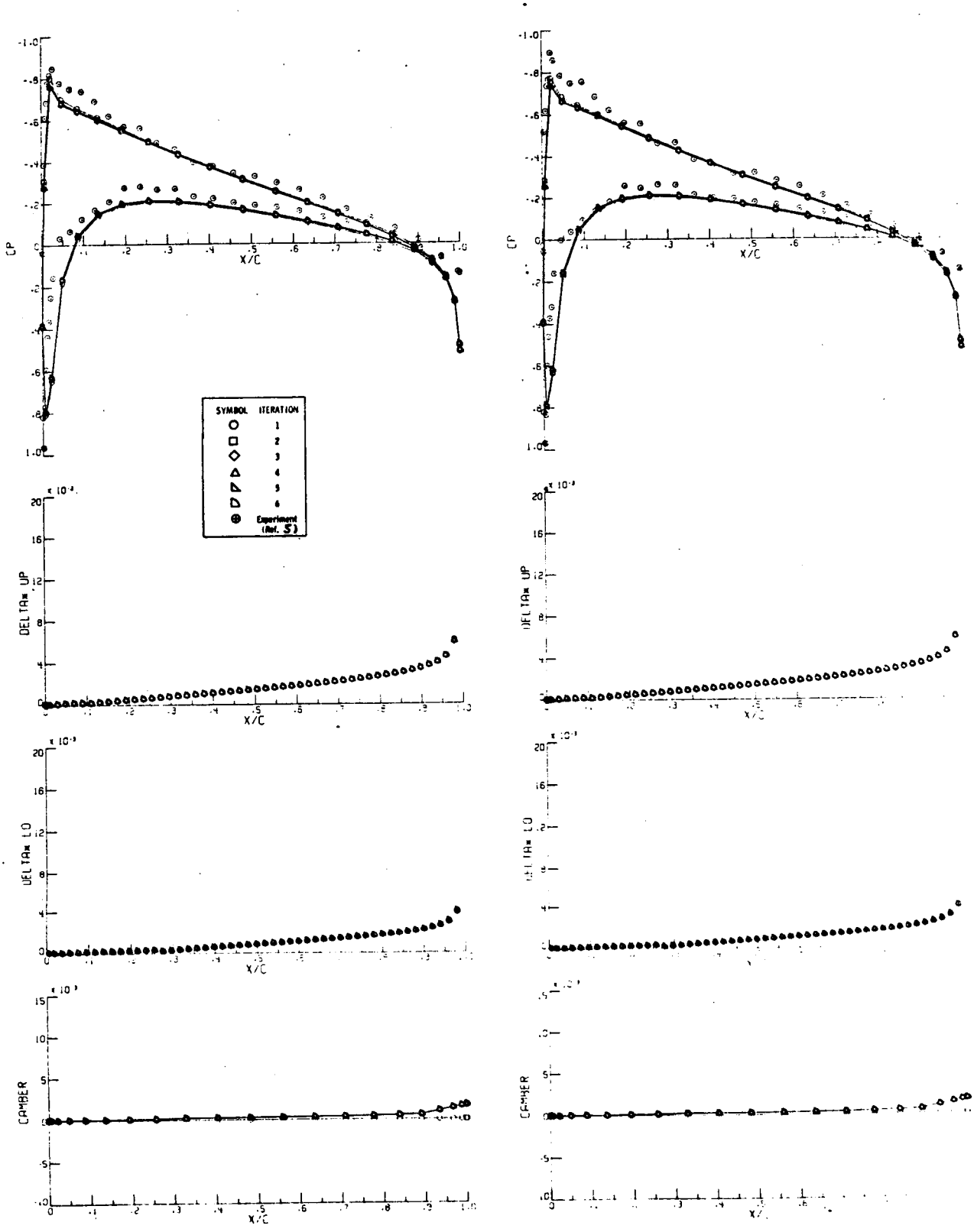

(a) η = .34

(b) η = .48

Figure 7. - Pressure distributions, displacement thickness, and camber line developments for five iterations of the strip method. $\Lambda = 0^{o}$, $\alpha = 2.53^{o}$.

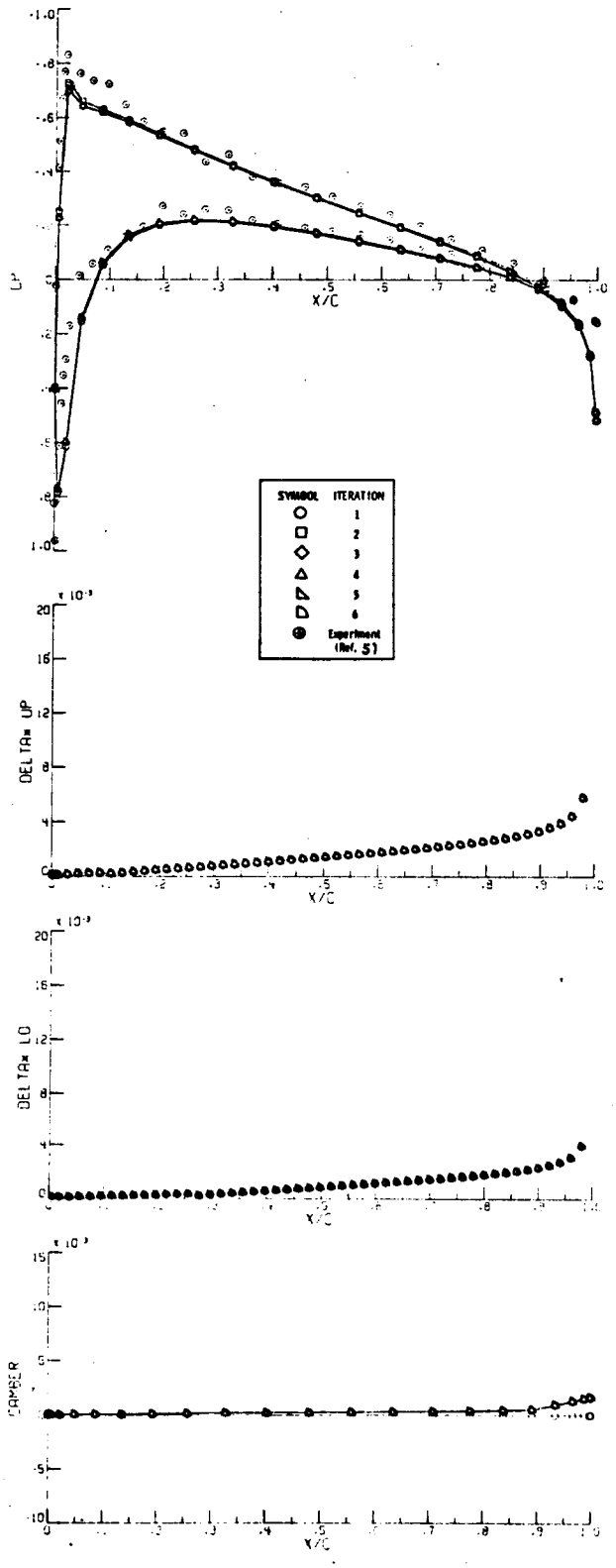

(c) η = .61

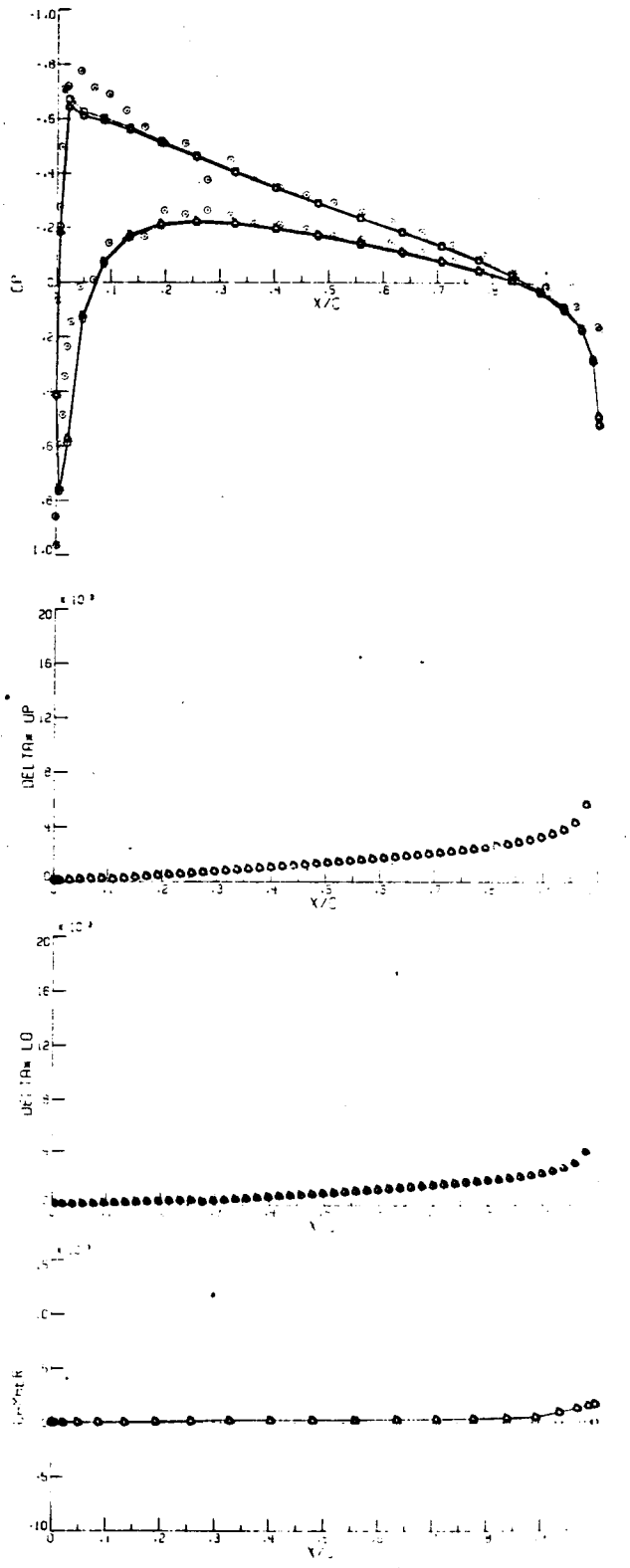

(d) η = .72

Figure 7. - Continued.

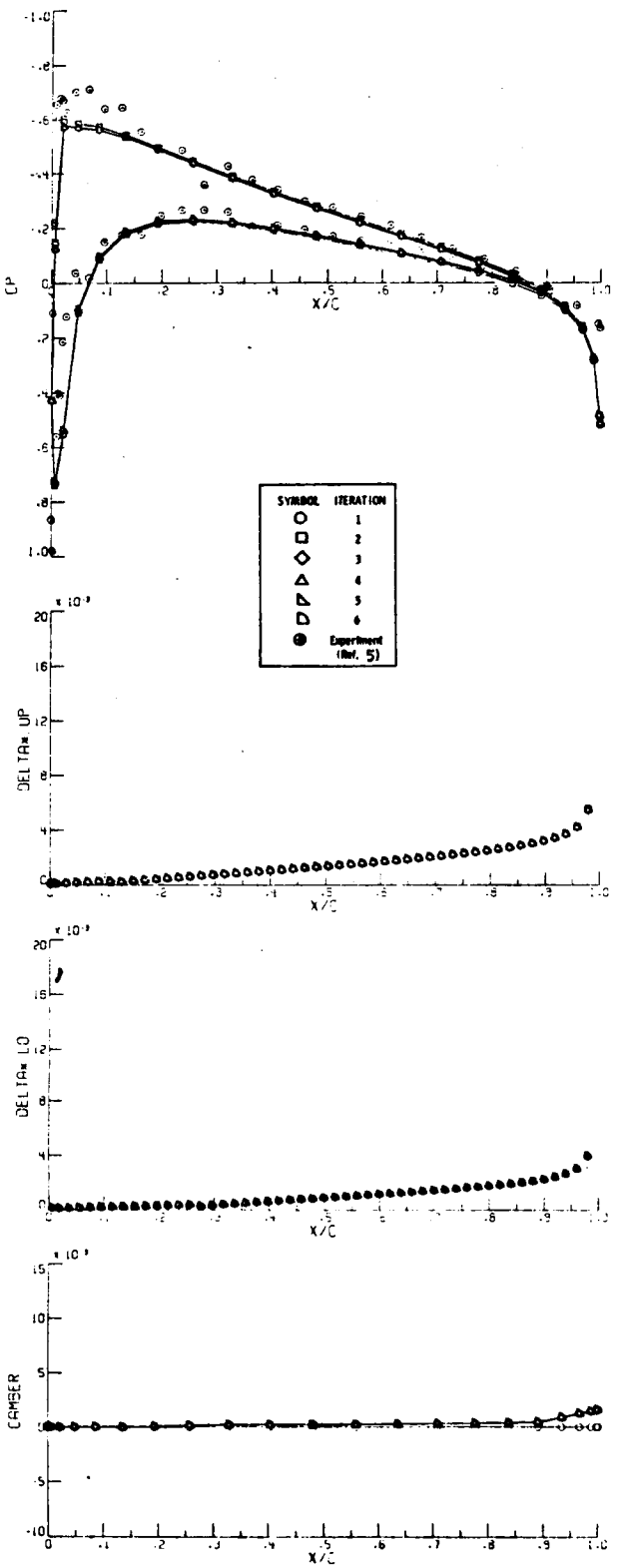

(e) η = .82

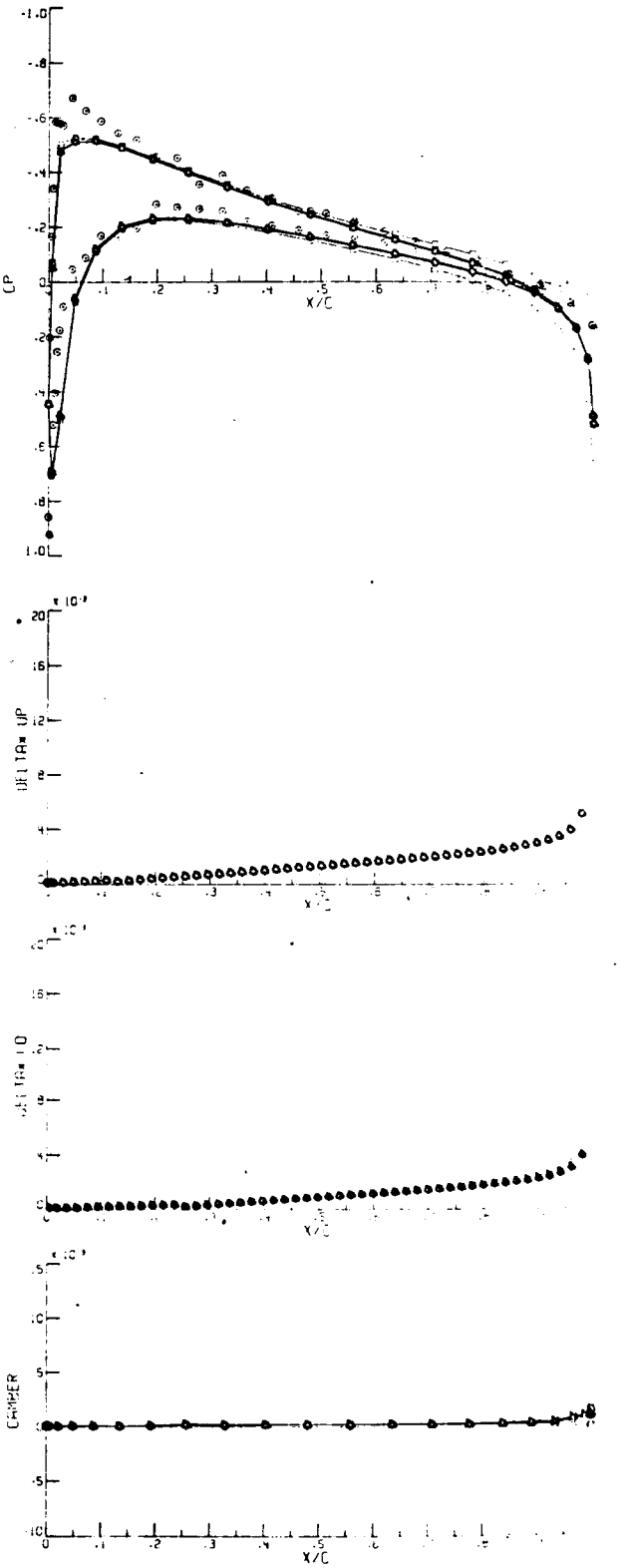

(f) η = .90

Figure 7. - Continued.

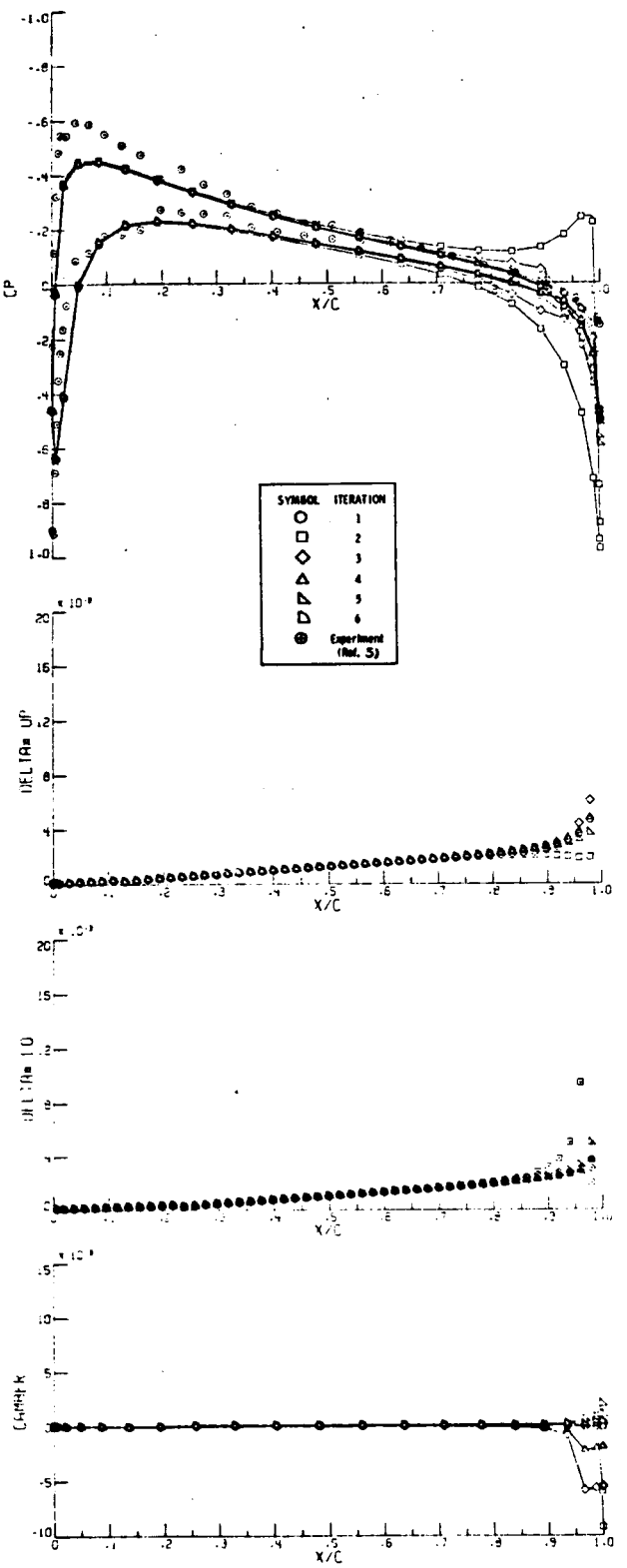

(g) η = .95

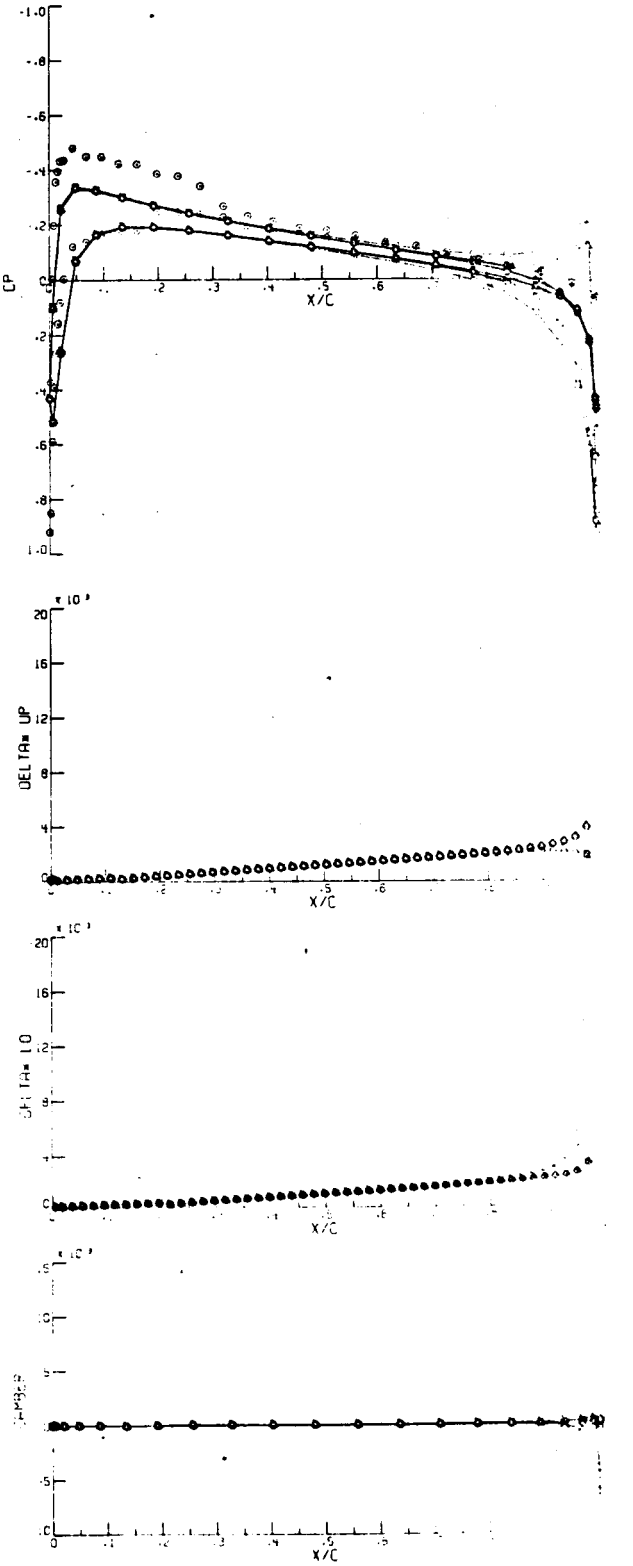

(h) η = .99

Figure 7. - Concluded.

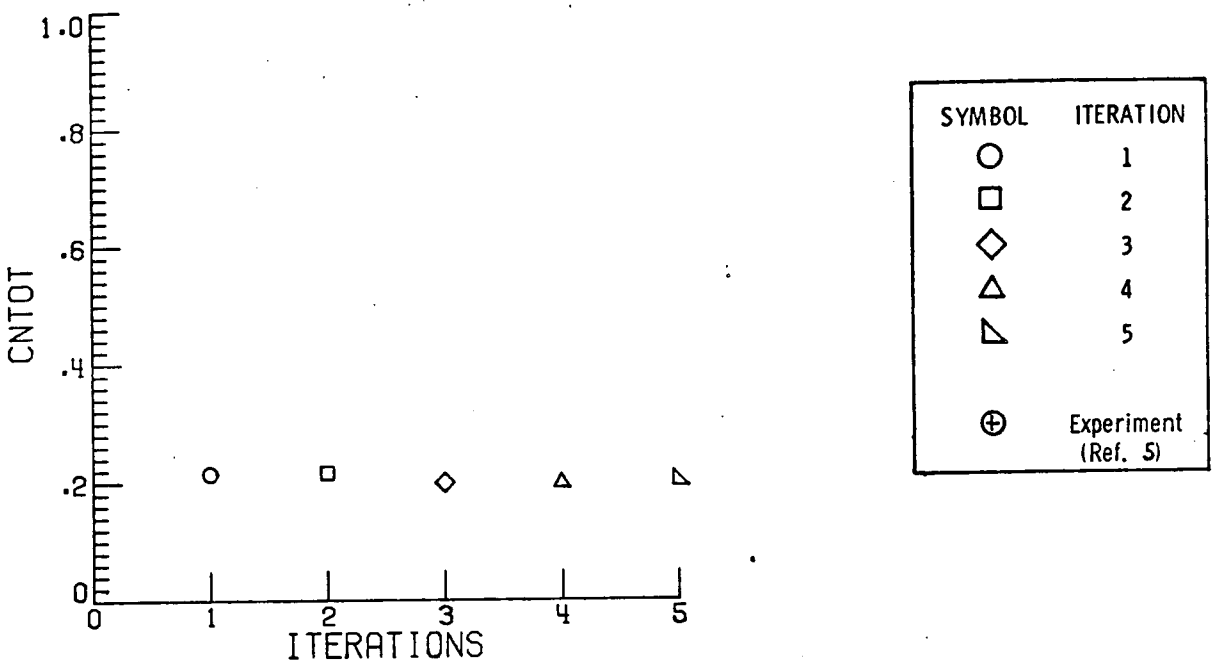

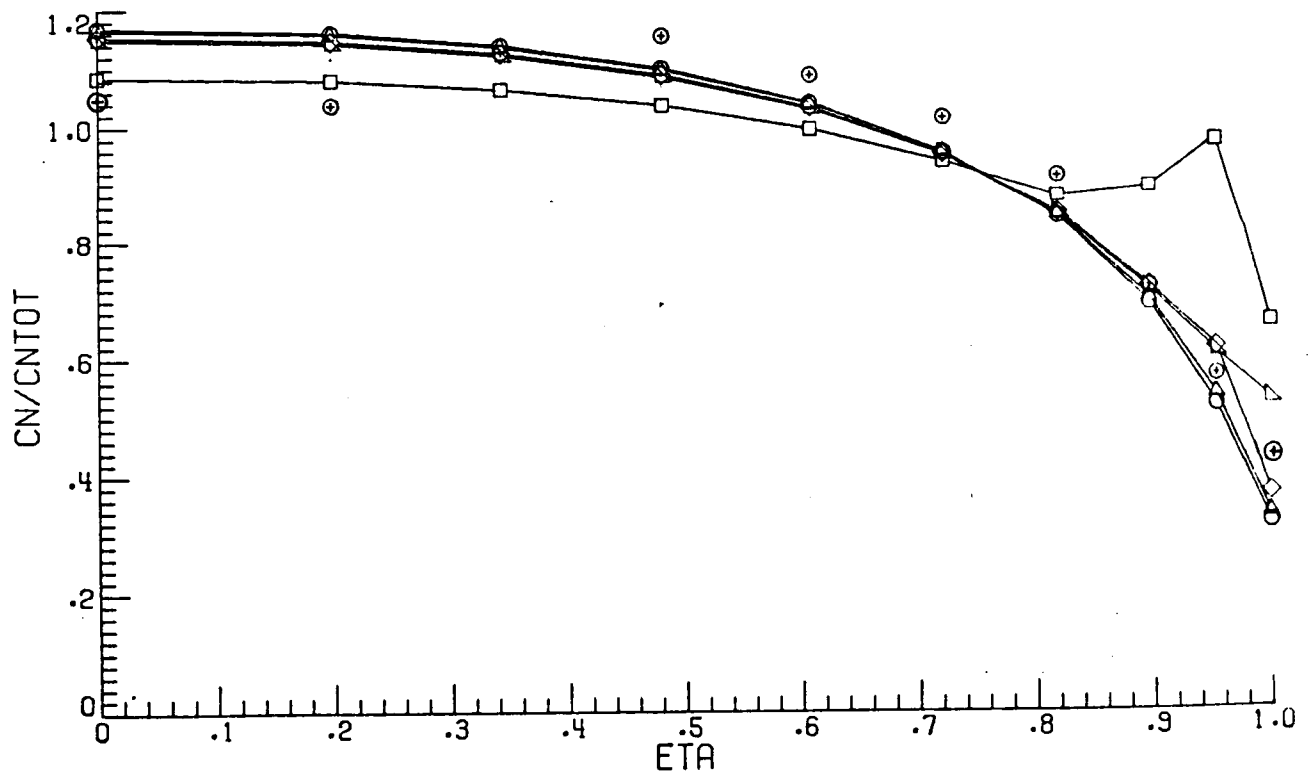

Figure 8. - Total and section normal-force coefficients versus iteration number and semispan station, respectively. $\Lambda = 0^{o}$, $\alpha = 2.53^{o}$.

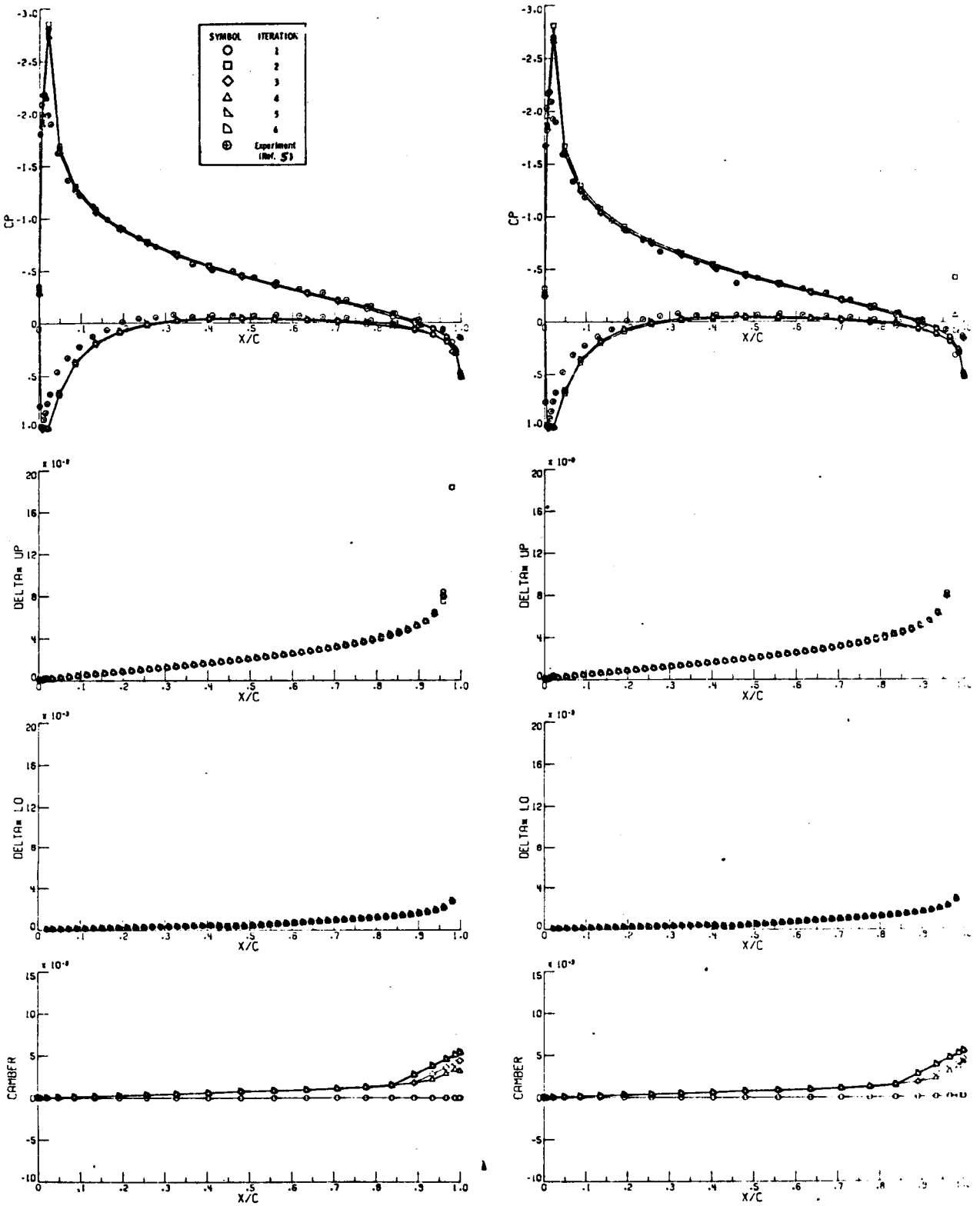

(a) η = .34 (b) η = .48

Figure 9. - Pressure distributions, displacement thickness, and camber line developments for five iterations of the strip method. $\Lambda = 0^{o}$, $\alpha = 6.75^{o}$.

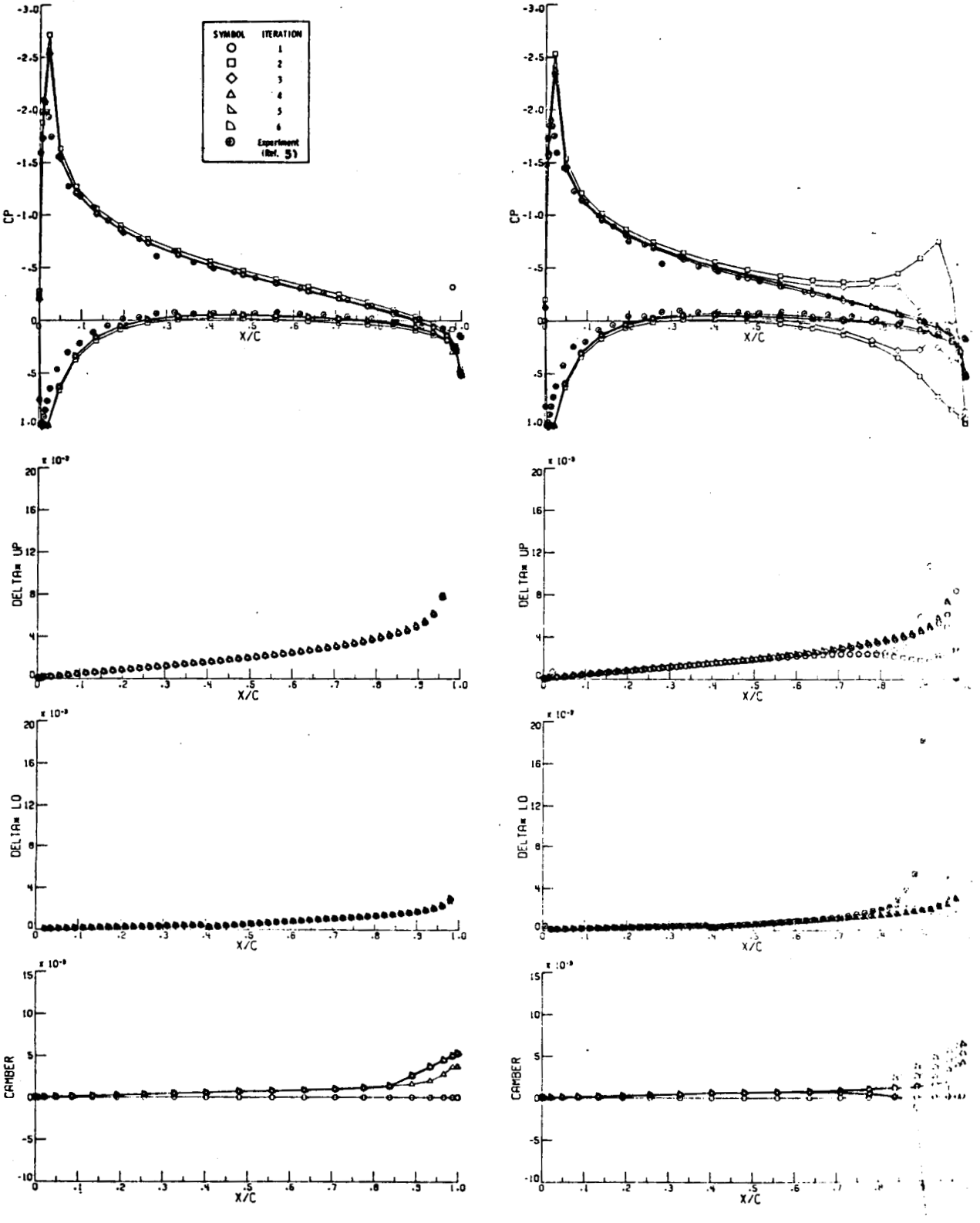

(c) η = .61

(d) η = .72

Figure 9. - Continued.

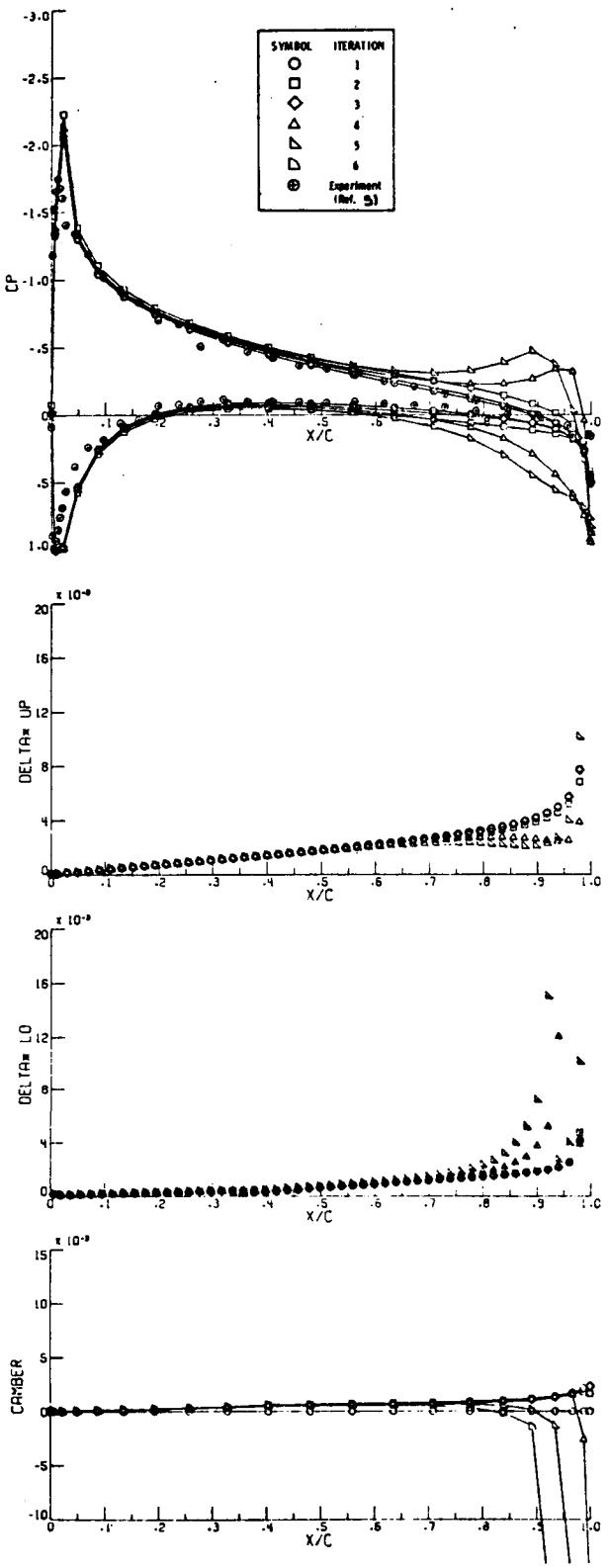

(e) η = .82

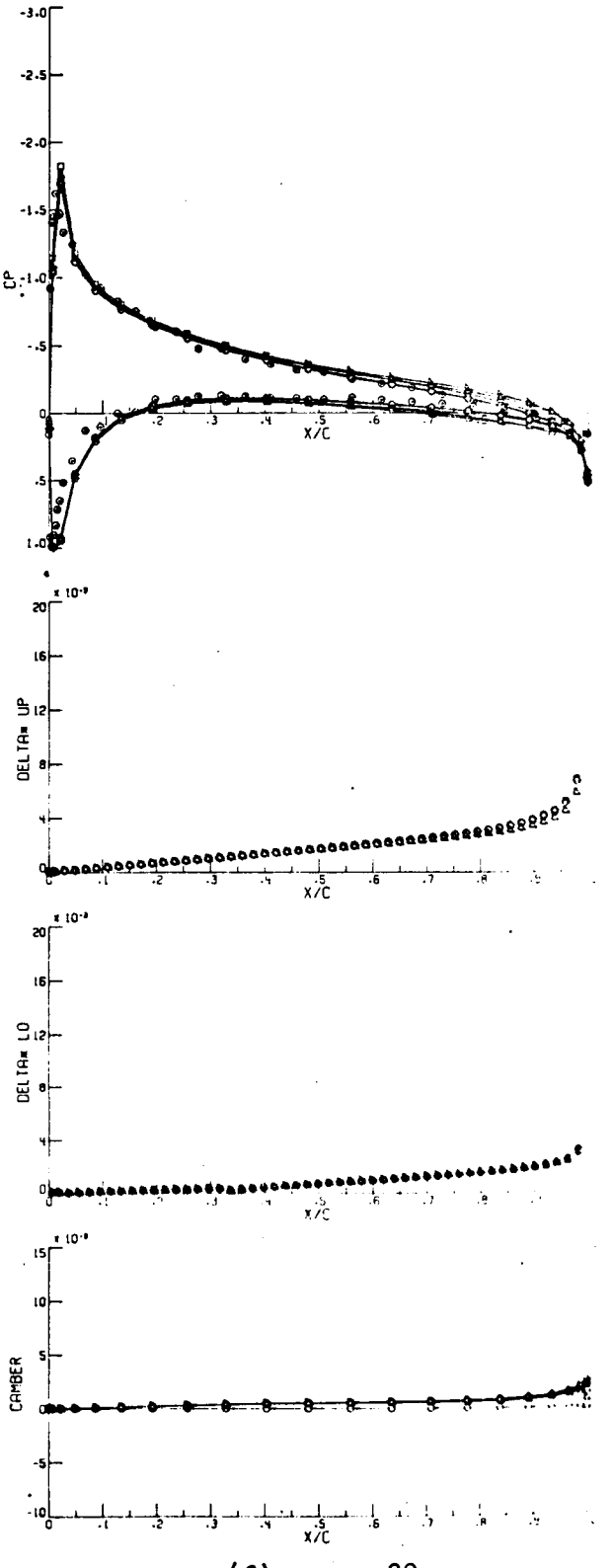

(f) η = .90

Figure 9. - Continued.

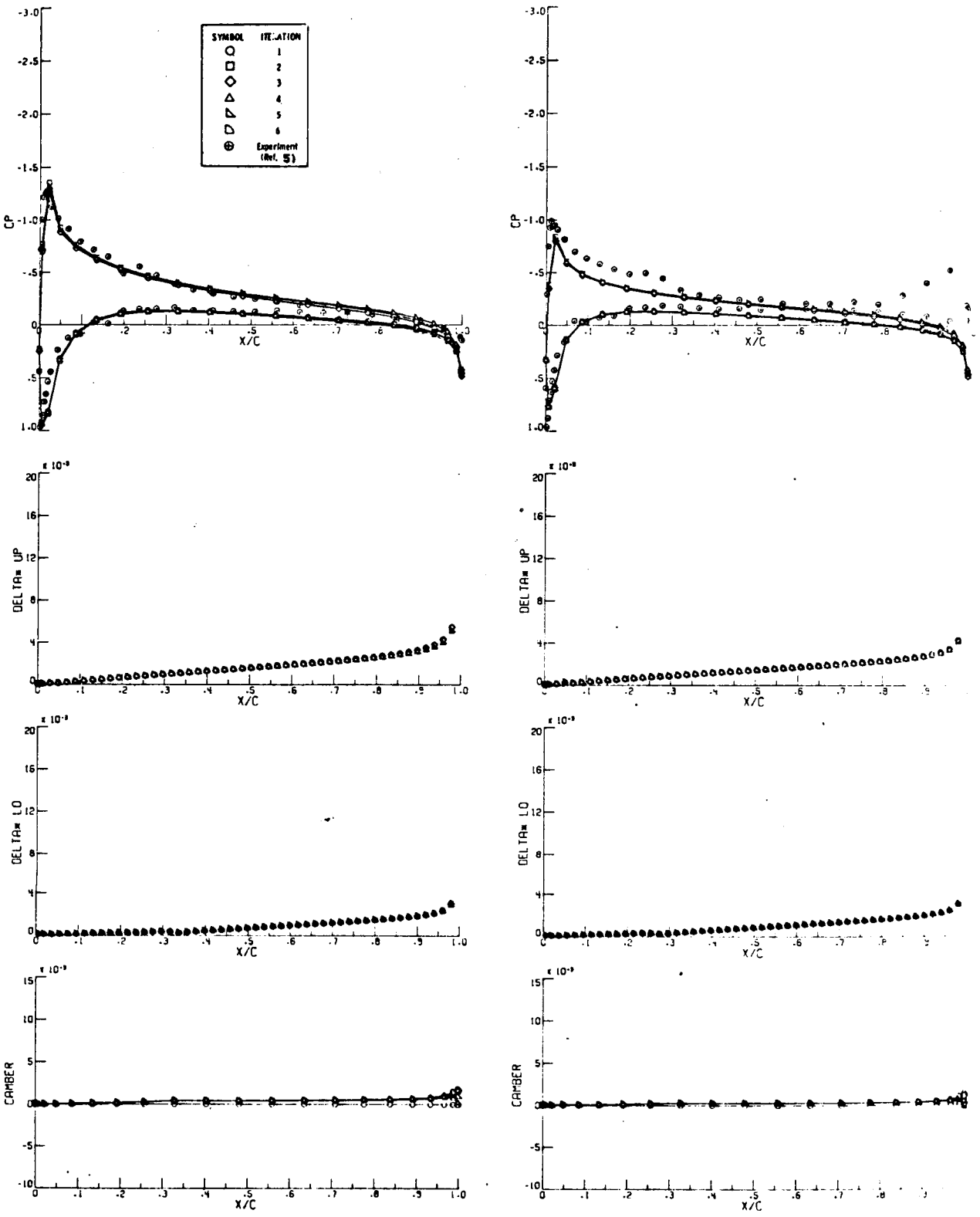

(g) η = .95

(h) η = .99

Figure 9. - Concluded.

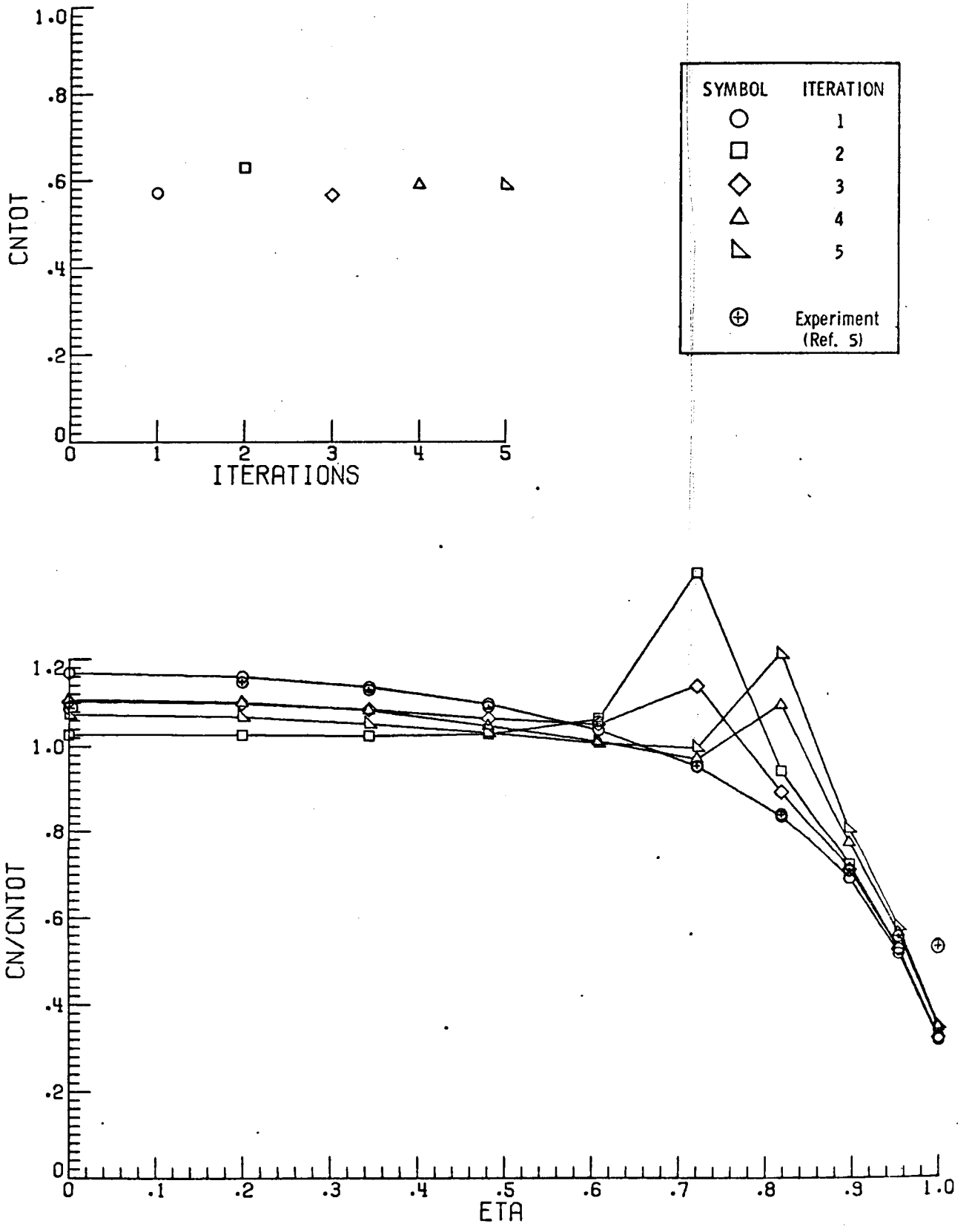

Figure 10. - Total and section normal-force coefficients versus iteration number and semispan station, respectively. $\Lambda = 0^{o}$, $\alpha = 6.75^{o}$.

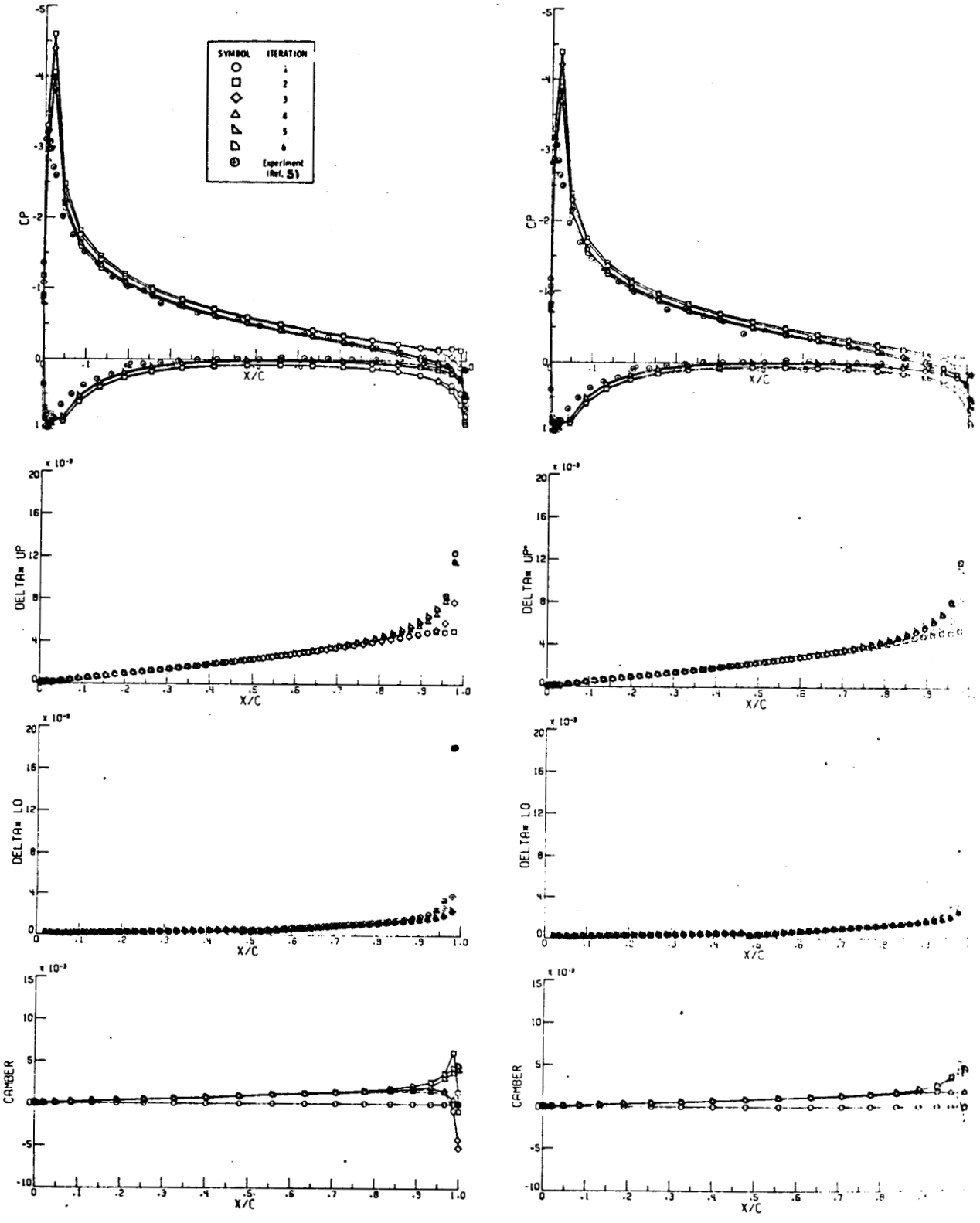

(a) η = .34 (b) η = .48

Figure 11. - Pressure distributions, displacement thickness, and camber line developments for five iterations of the strip method. $\Lambda = 0^{o}$, $\alpha = 8.85^{o}$.

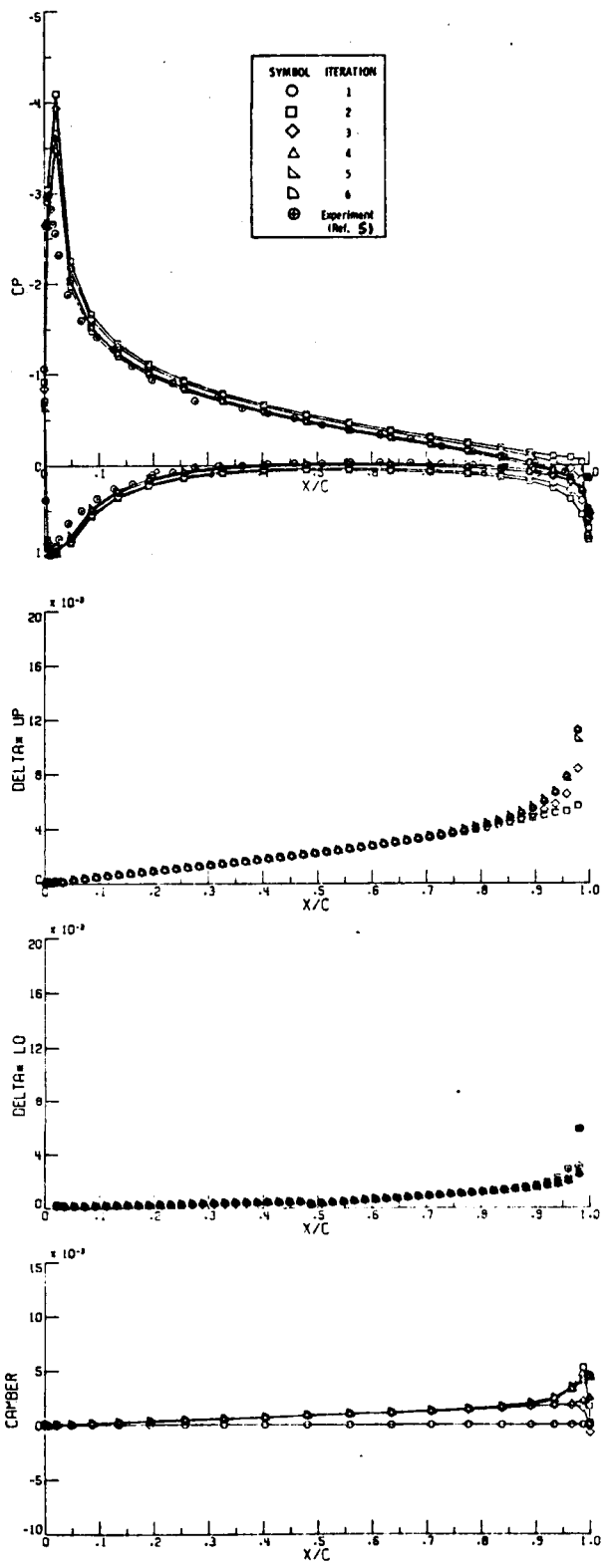

(c) η = .61

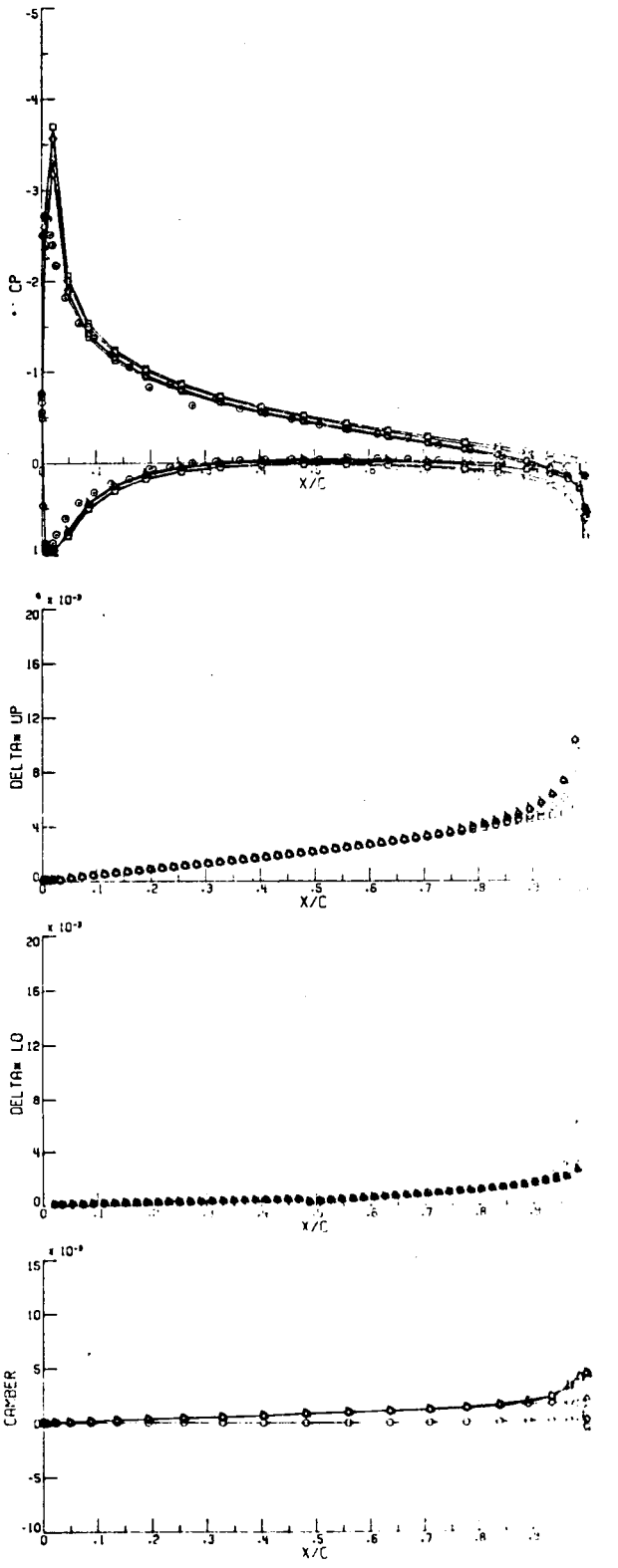

(d) η = .72

Figure 11. - Continued.

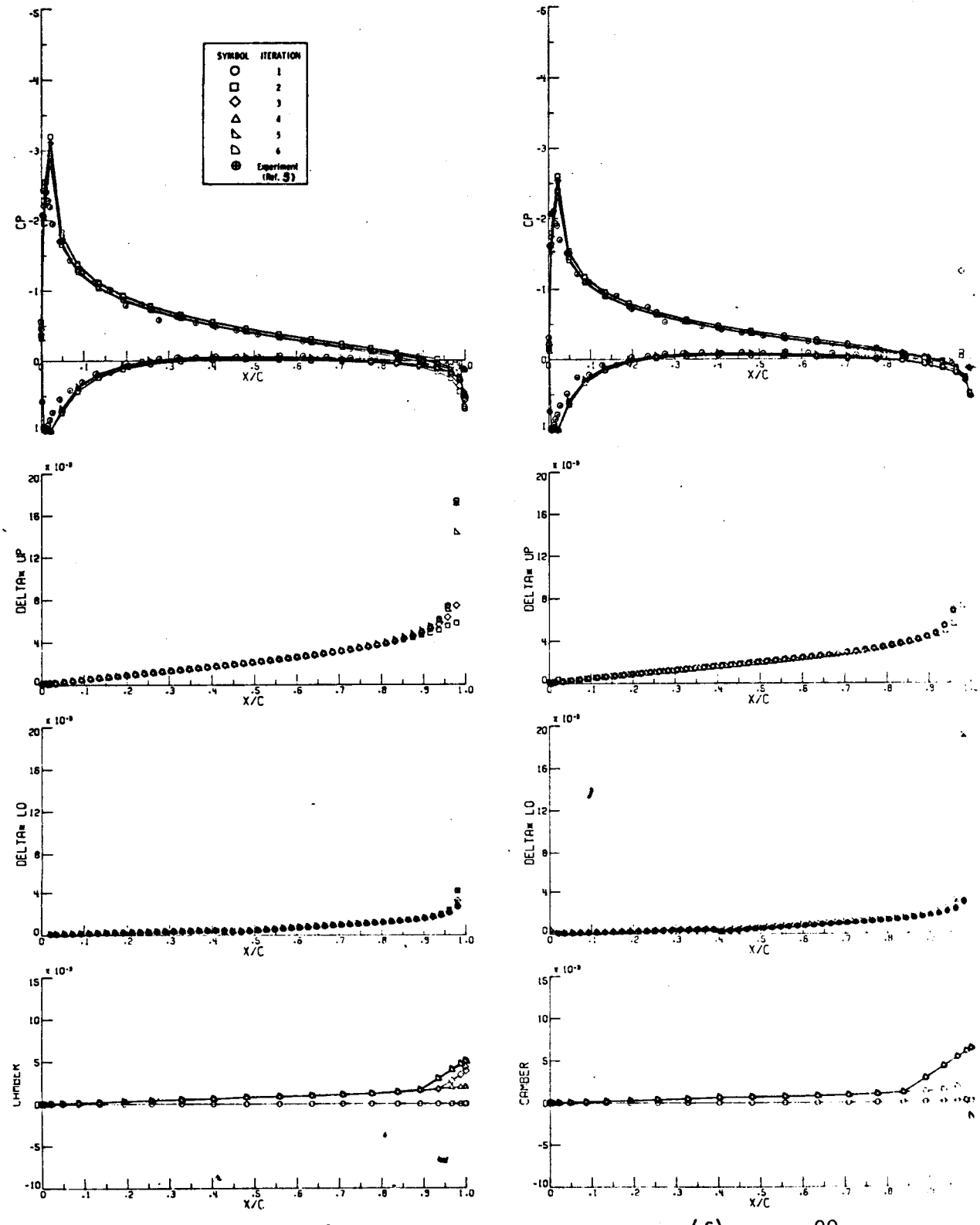

(e) η = .82

(f) η = .90

Figure 11. - Continued.

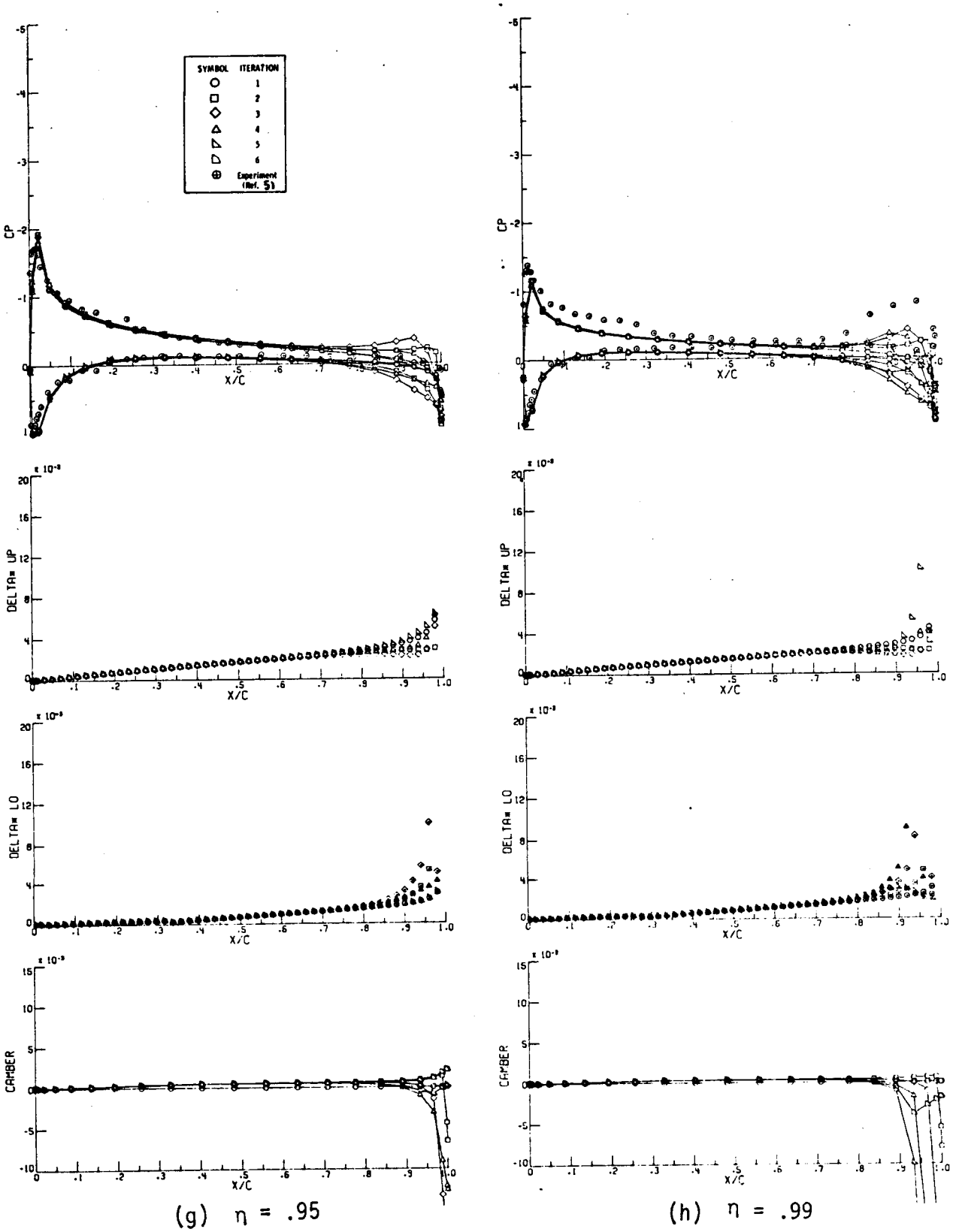

(g) η = .95

(h) η = .99

Figure 11. - Concluded.

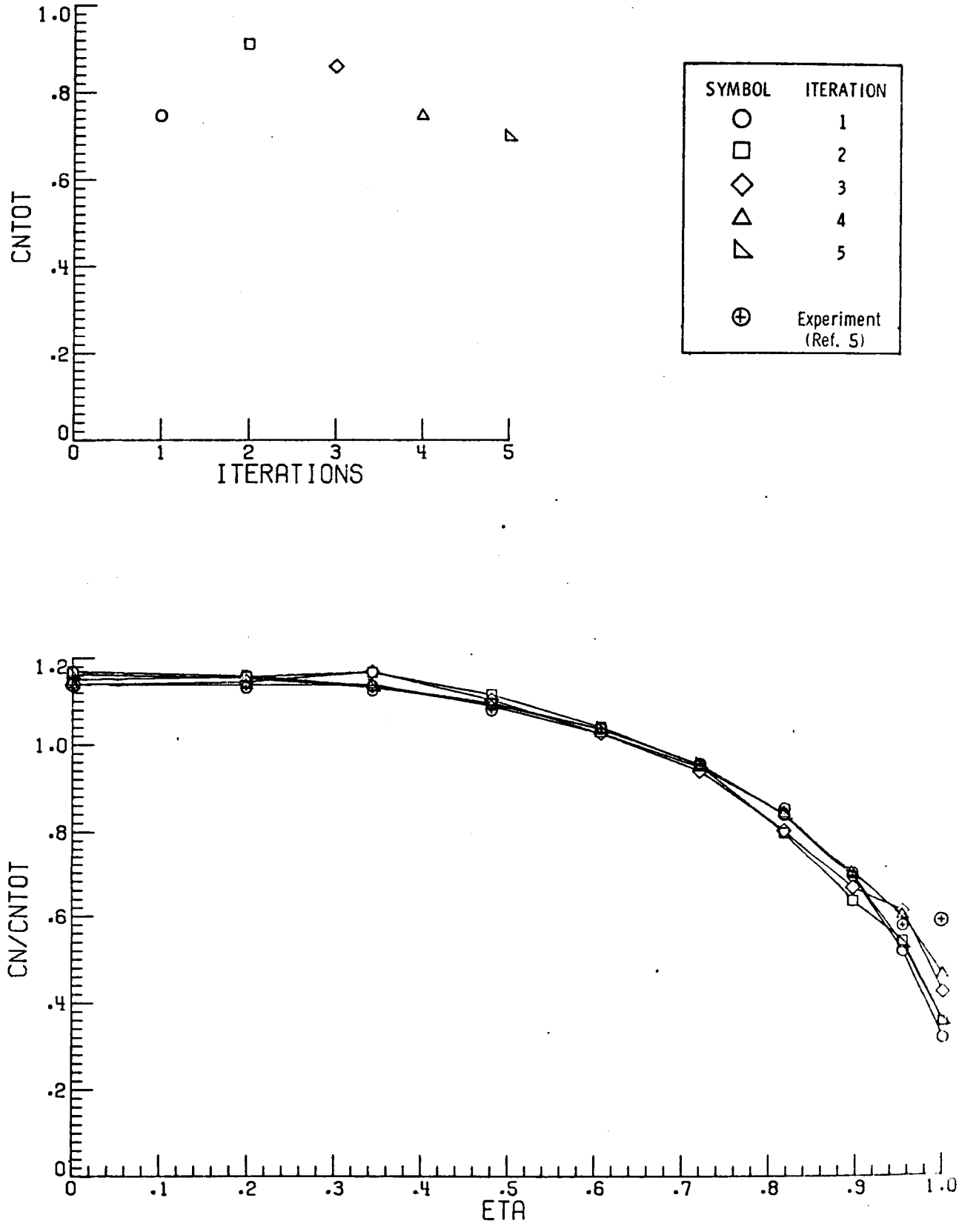

Figure 12. - Total and section normal-force coefficients versus iteration number and semispan station, respectively. $\Lambda = 0^{o}$, $\alpha = 8.85^{o}$.

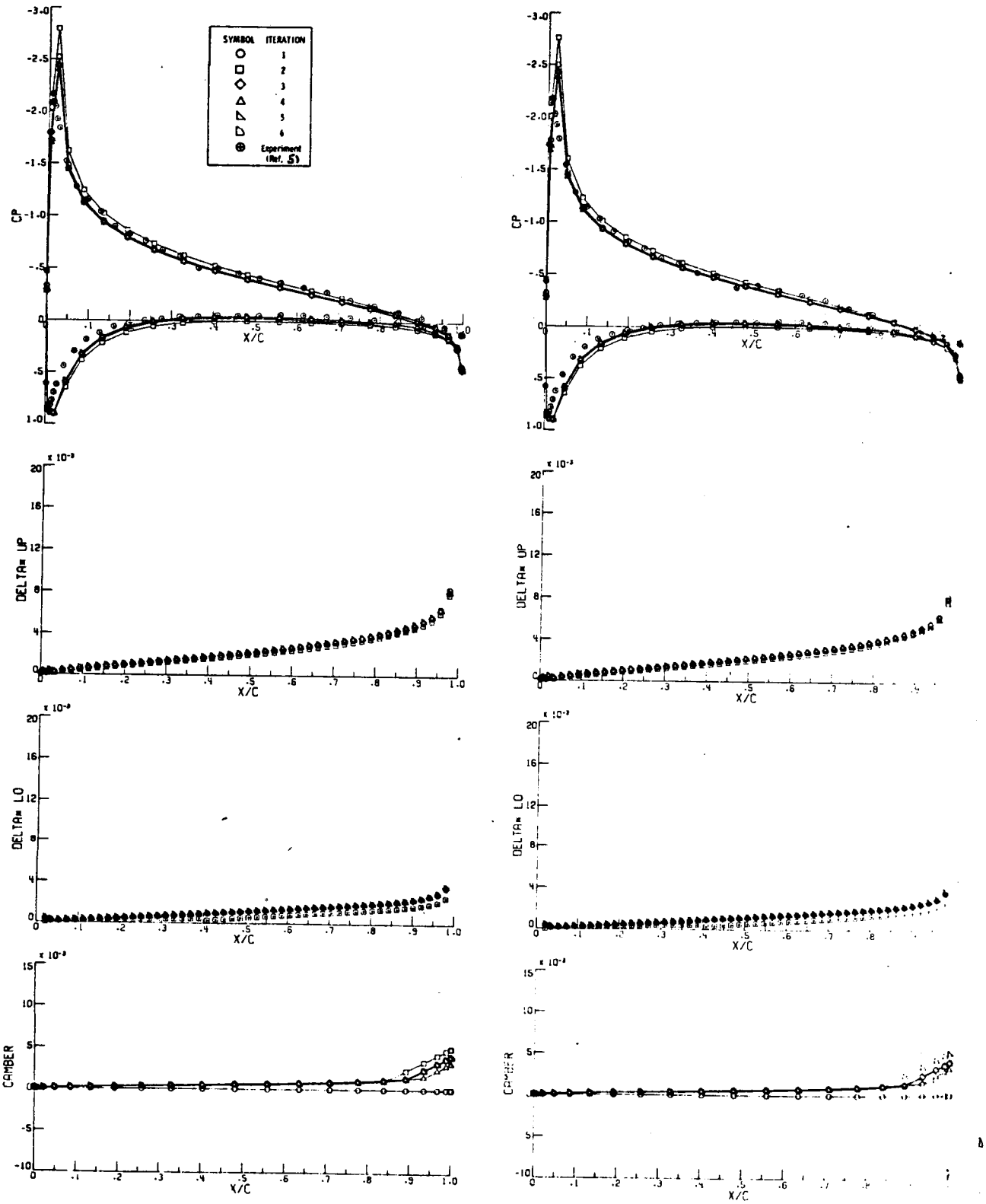

(a) η = .34

(b) η = .48

Figure 13. - Pressure distributions, displacement thickness, and camber line developments for five iterations of the strip method. $\Lambda = 20^{o}$, $\alpha = 6.76^{o}$.

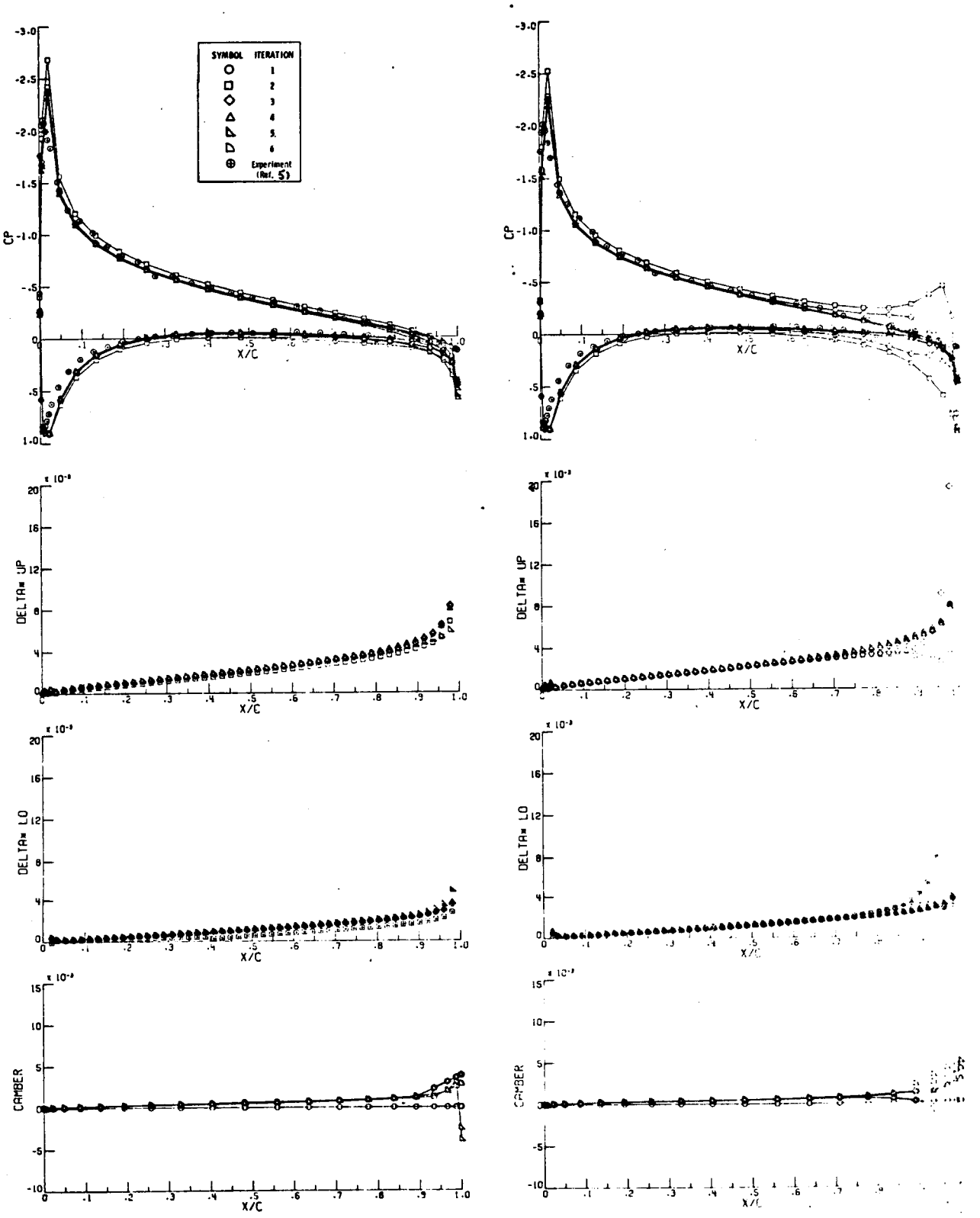

(c) η = .61

(d) η = .72

Figure 13. - Continued.

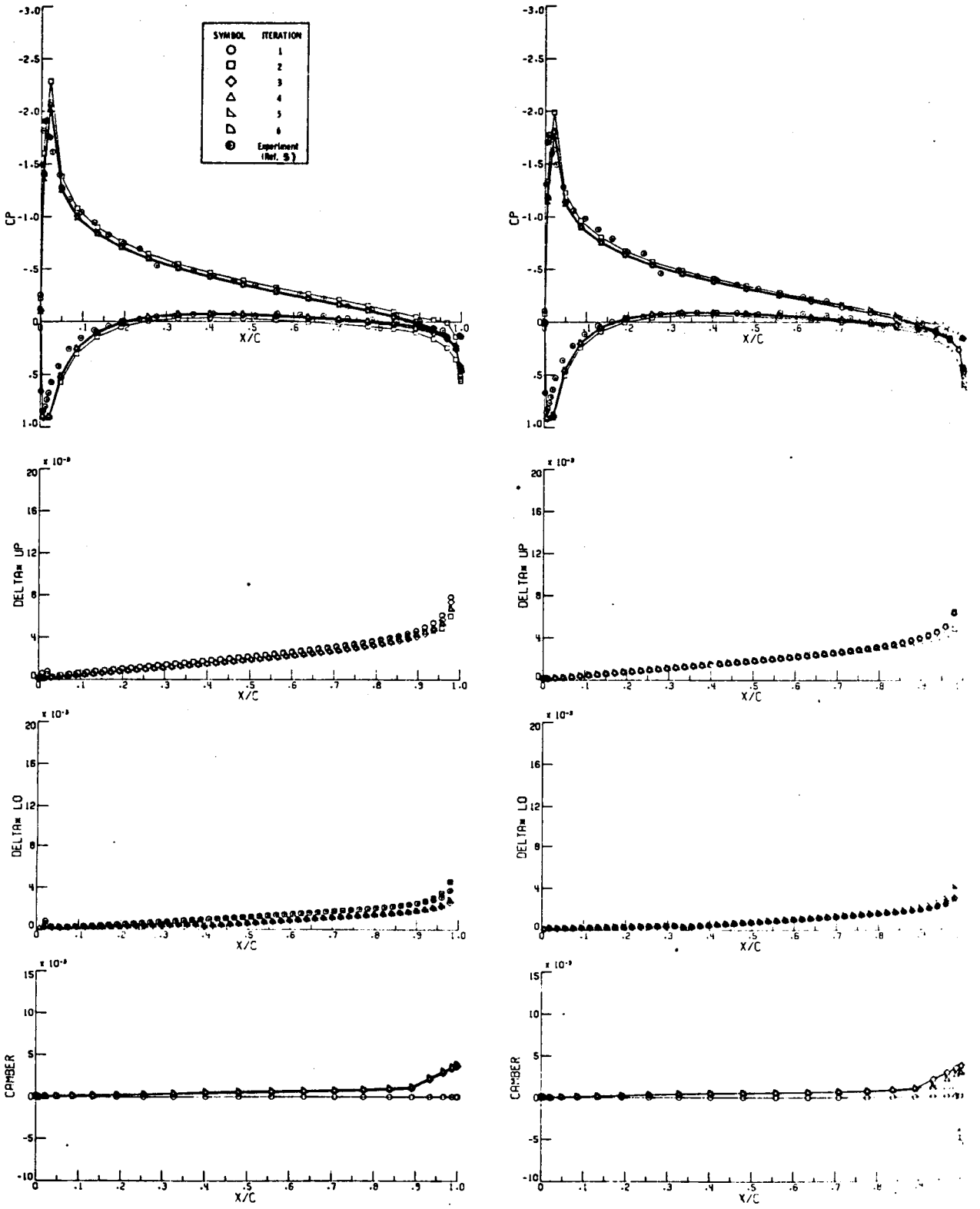

(e) η = .82

(f) η = .90

Figure 13. - Continued.

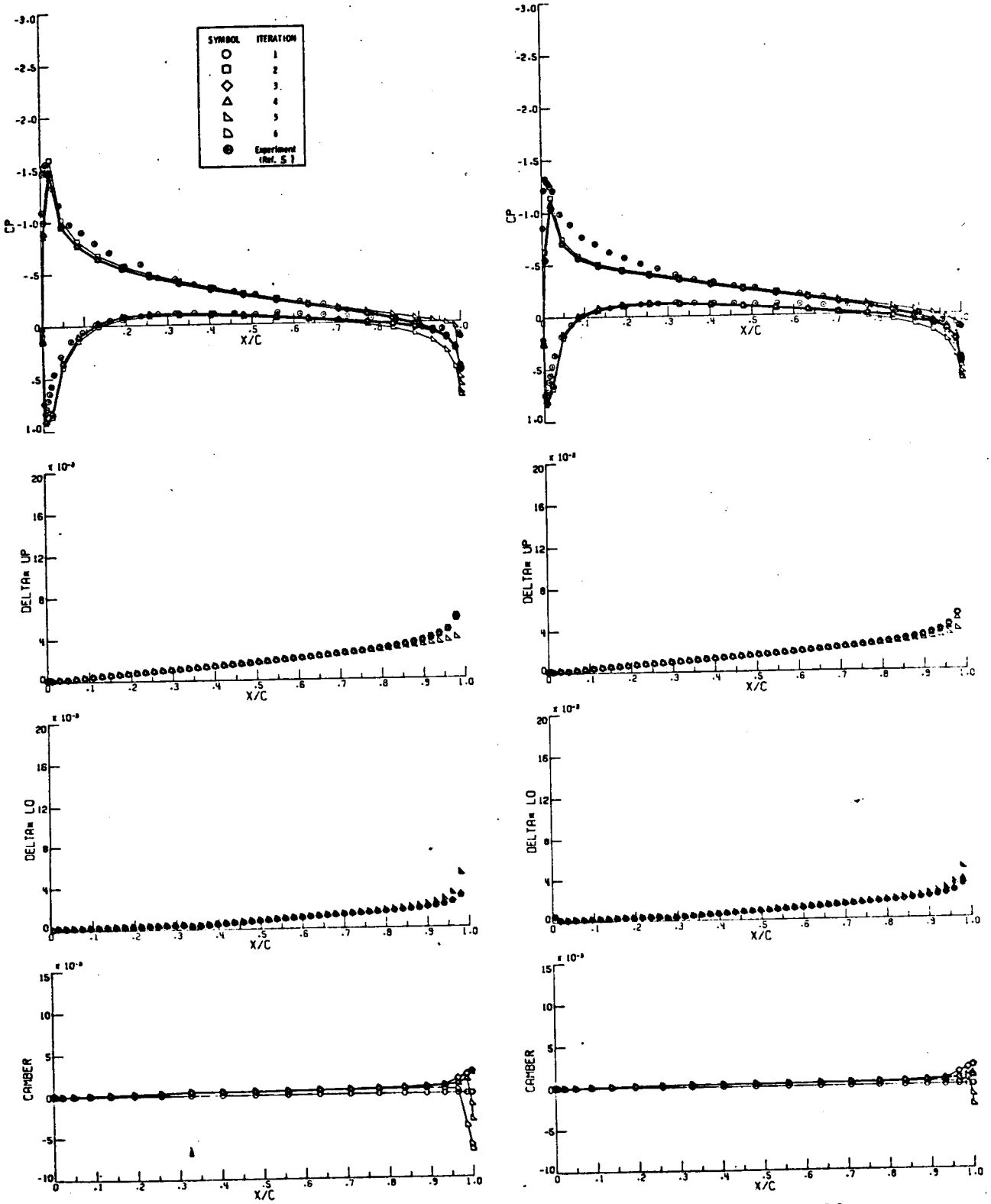

(g) η = .95

(h) η = .99

Figure 13. - Concluded.

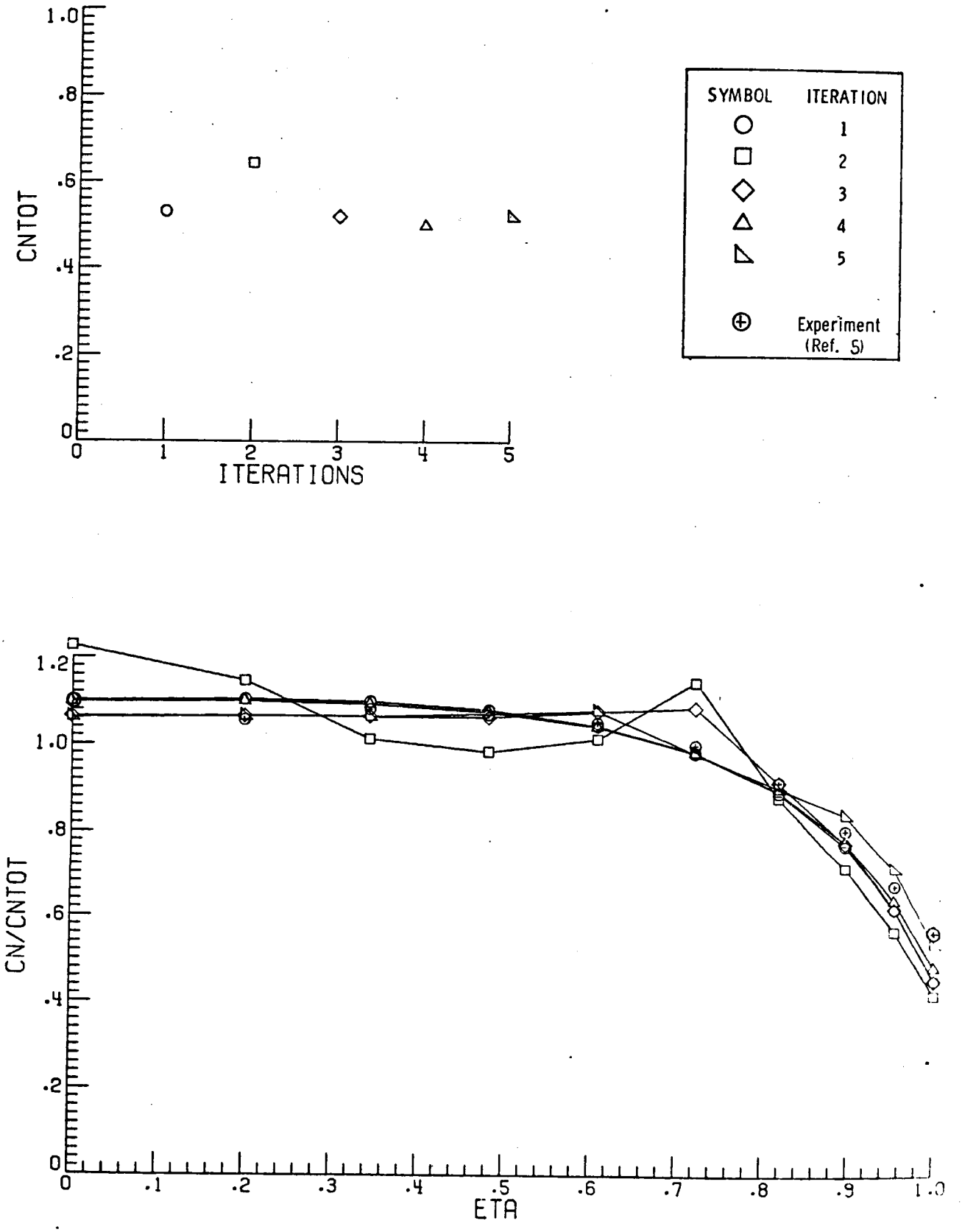

Figure 14. - Total and section normal-force coefficients versus iteration number and semispan station, respectively. $\Lambda = 20^{\circ}$, $\alpha = 6.76^{\circ}$.

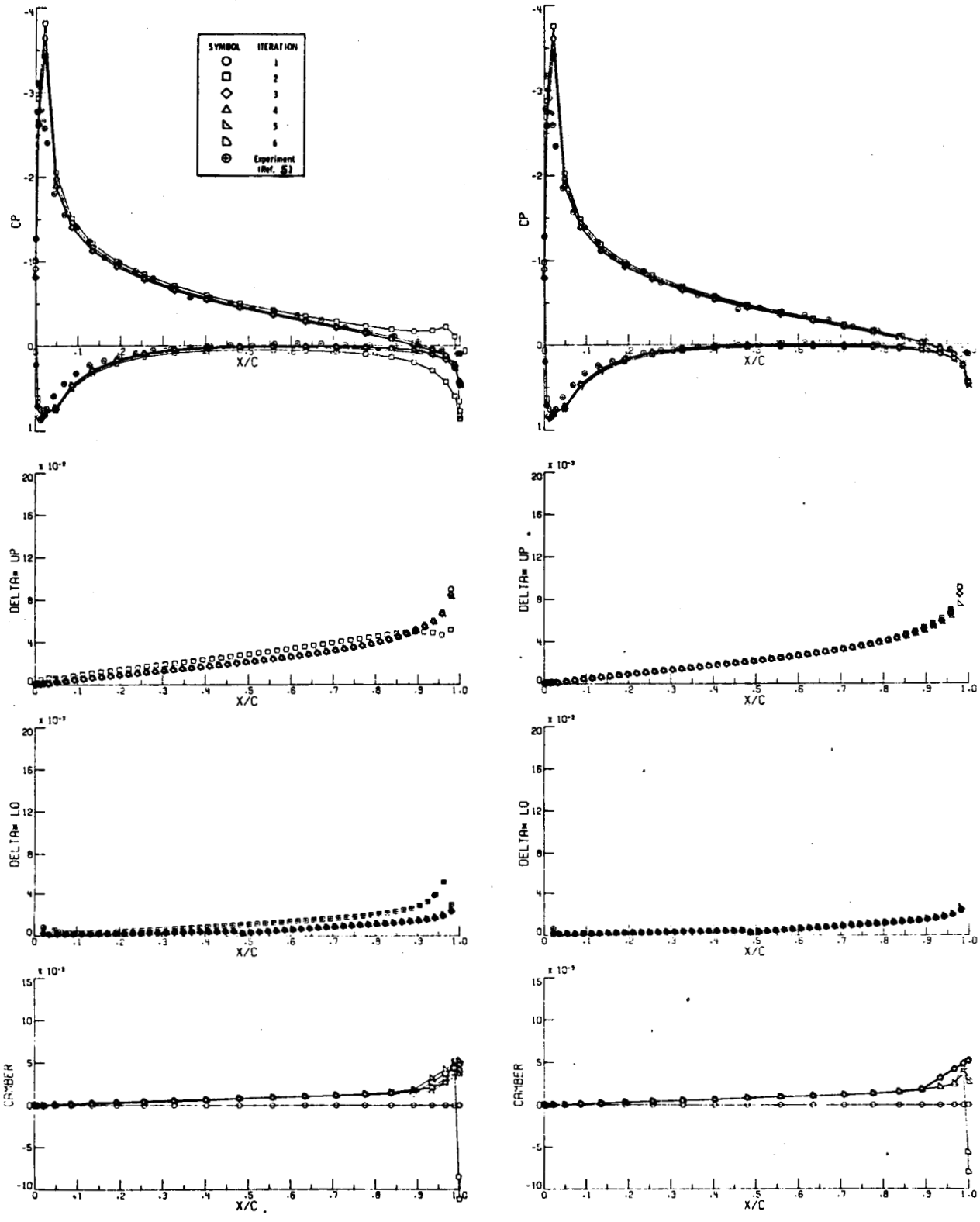

(a) η = .34 (b) η = .48

Figure 15. - Pressure distributions, displacement thickness, and camber line developments for five iterations of the strip method. $\Lambda = 20^{o}$, $\alpha = 8.84^{o}$.

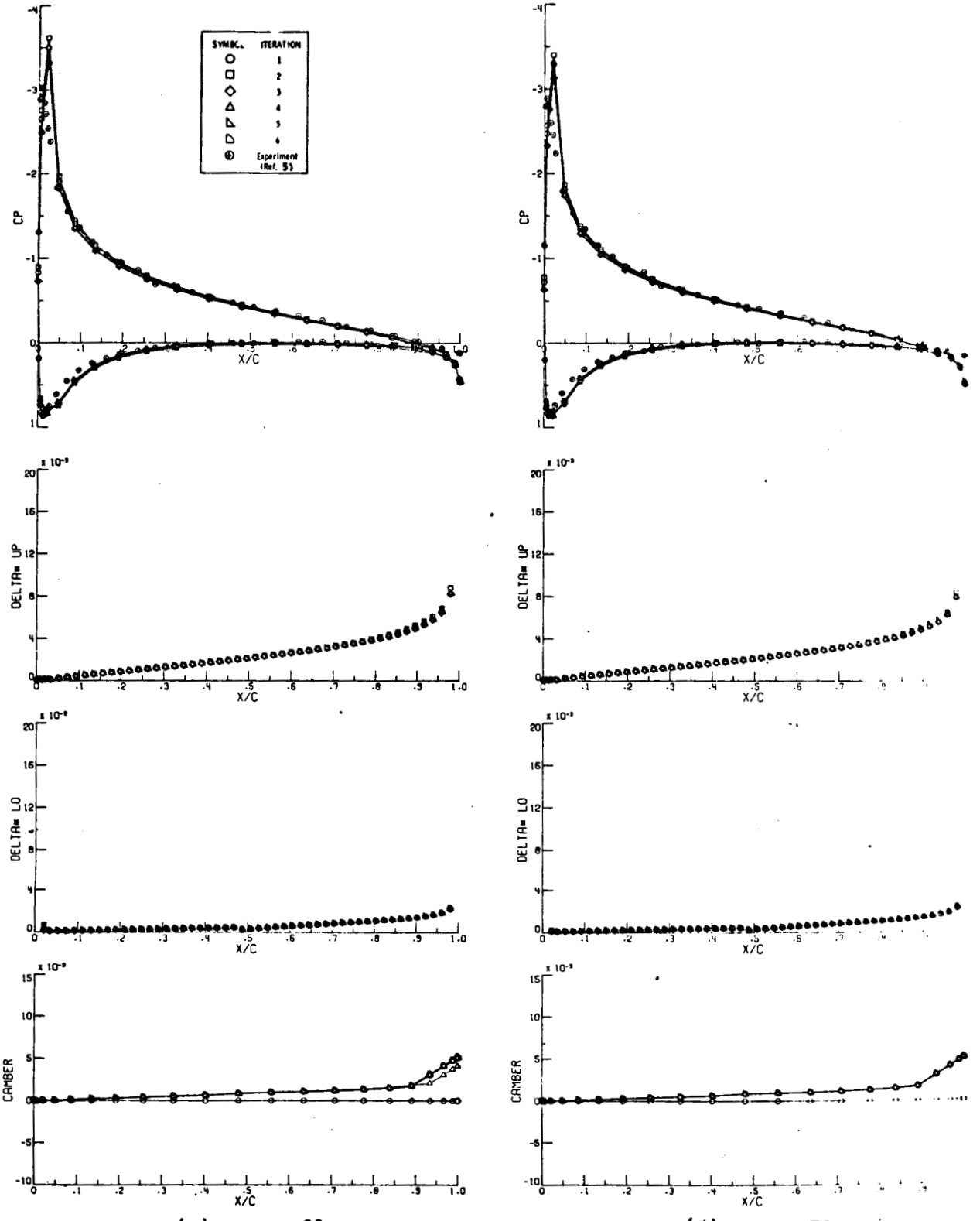

(c) η = .61

(d) η = .72

Figure 15. - Continued.

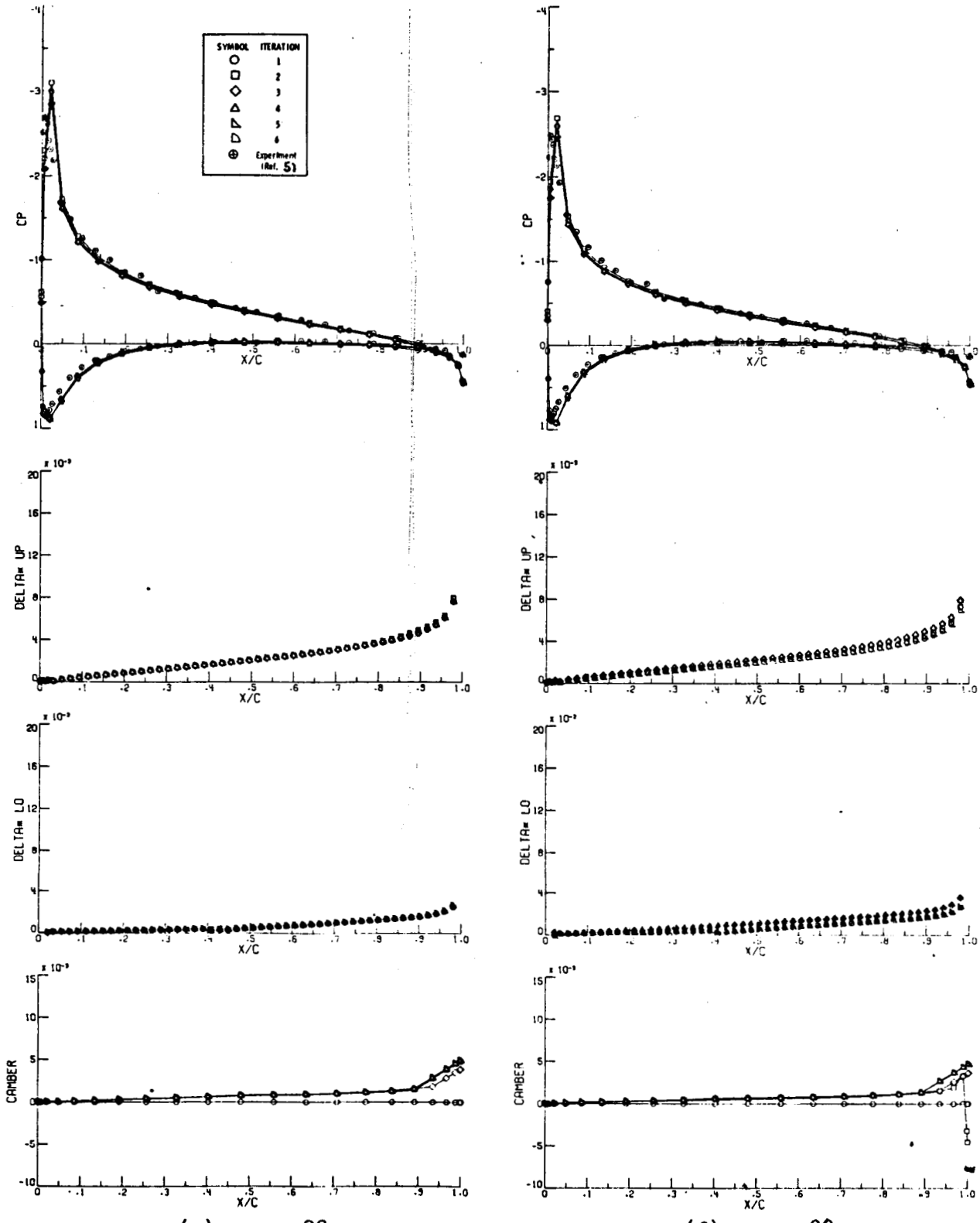

(e) η = .82

(f) η = .90

Figure 15. - Continued.

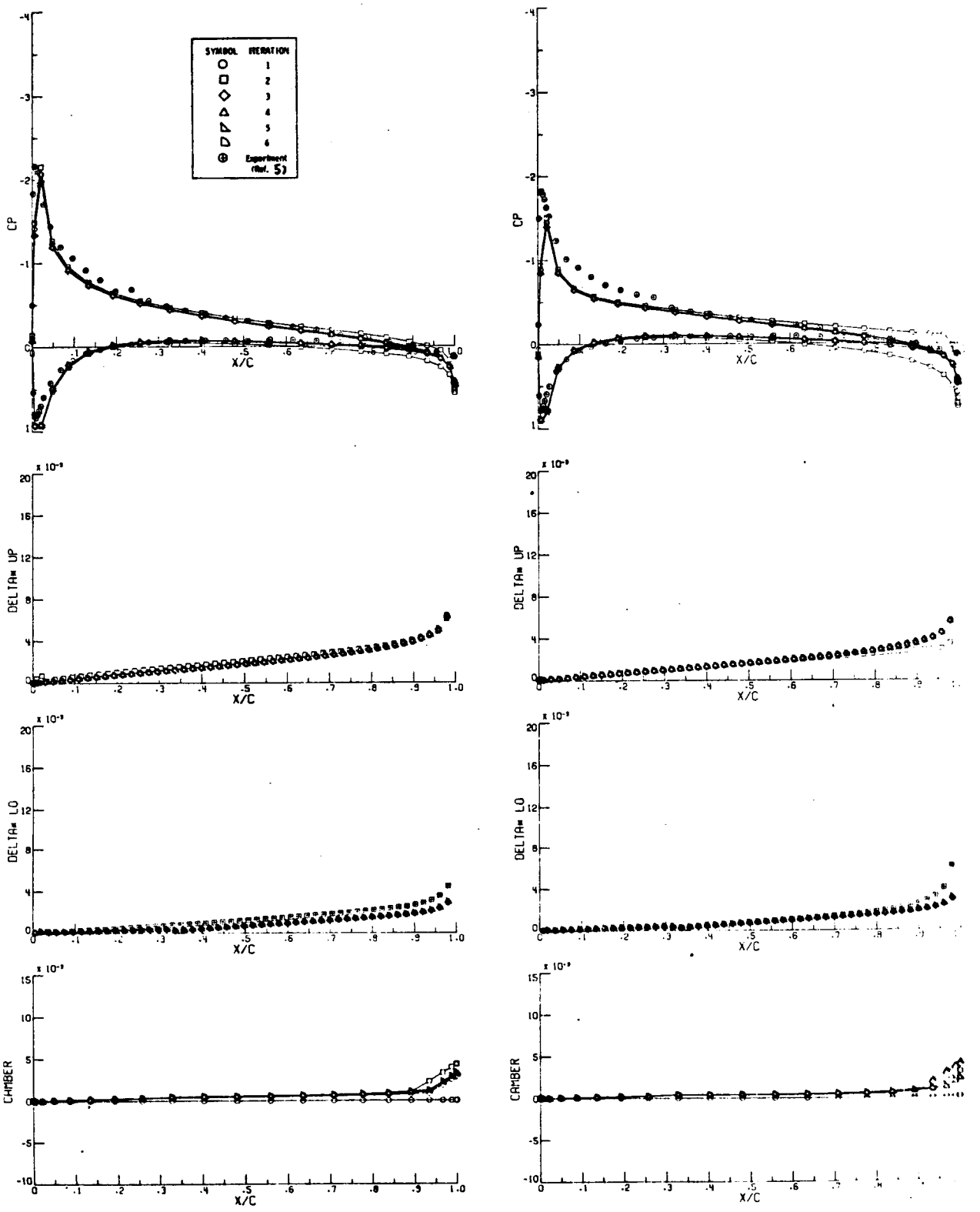

(g) η = .95

(h) η = .99

Figure 15. - Concluded.

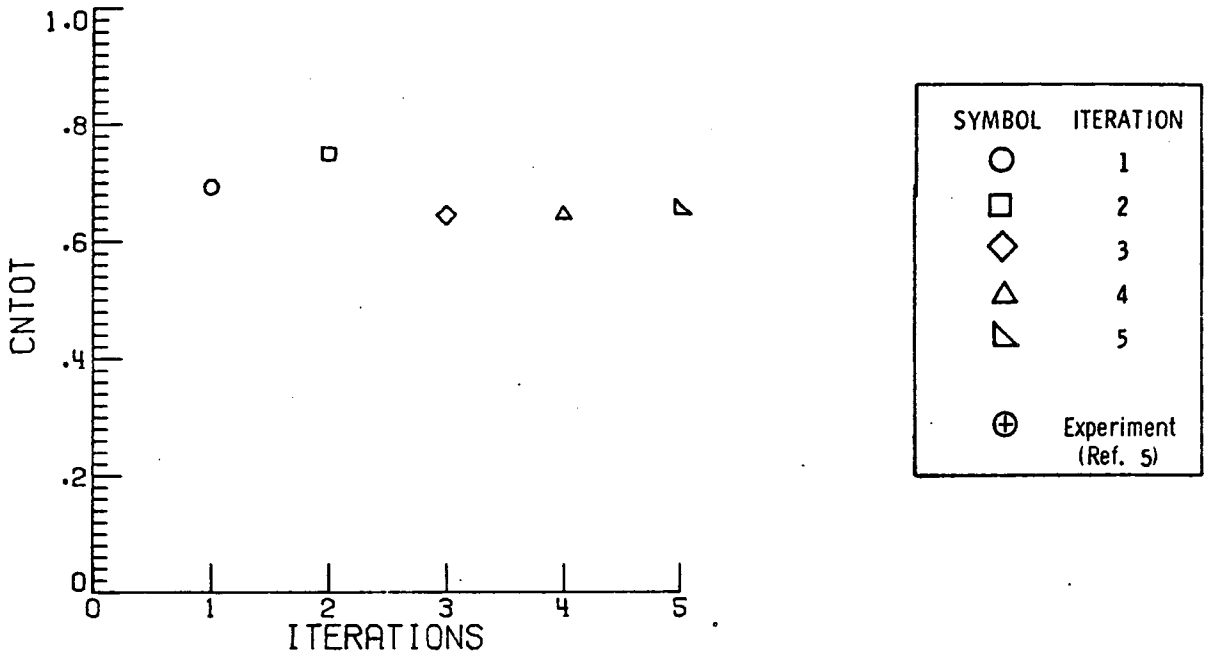

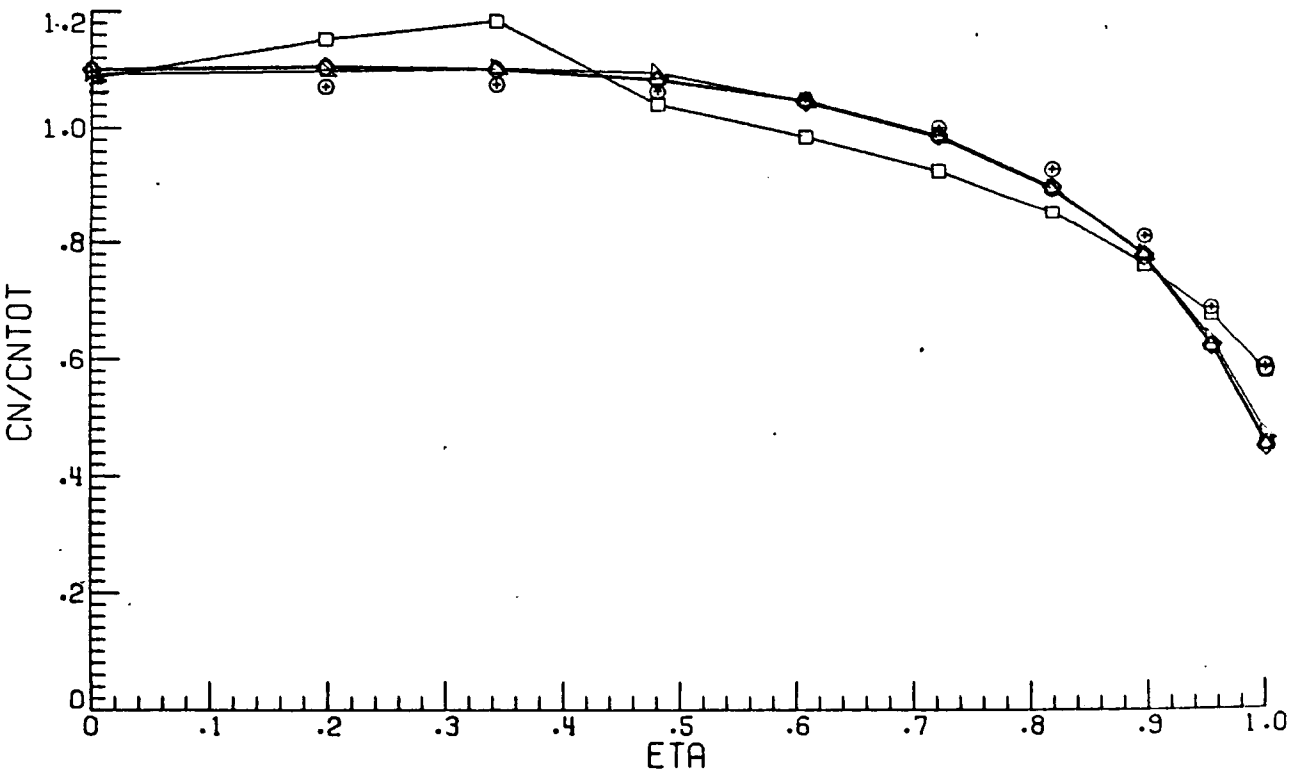

Figure 16. - Total and section normal-force coefficients versus iteration number and semispan station, respectively. $\Lambda = 20^{o}$, $\alpha = 8.84^{o}$.

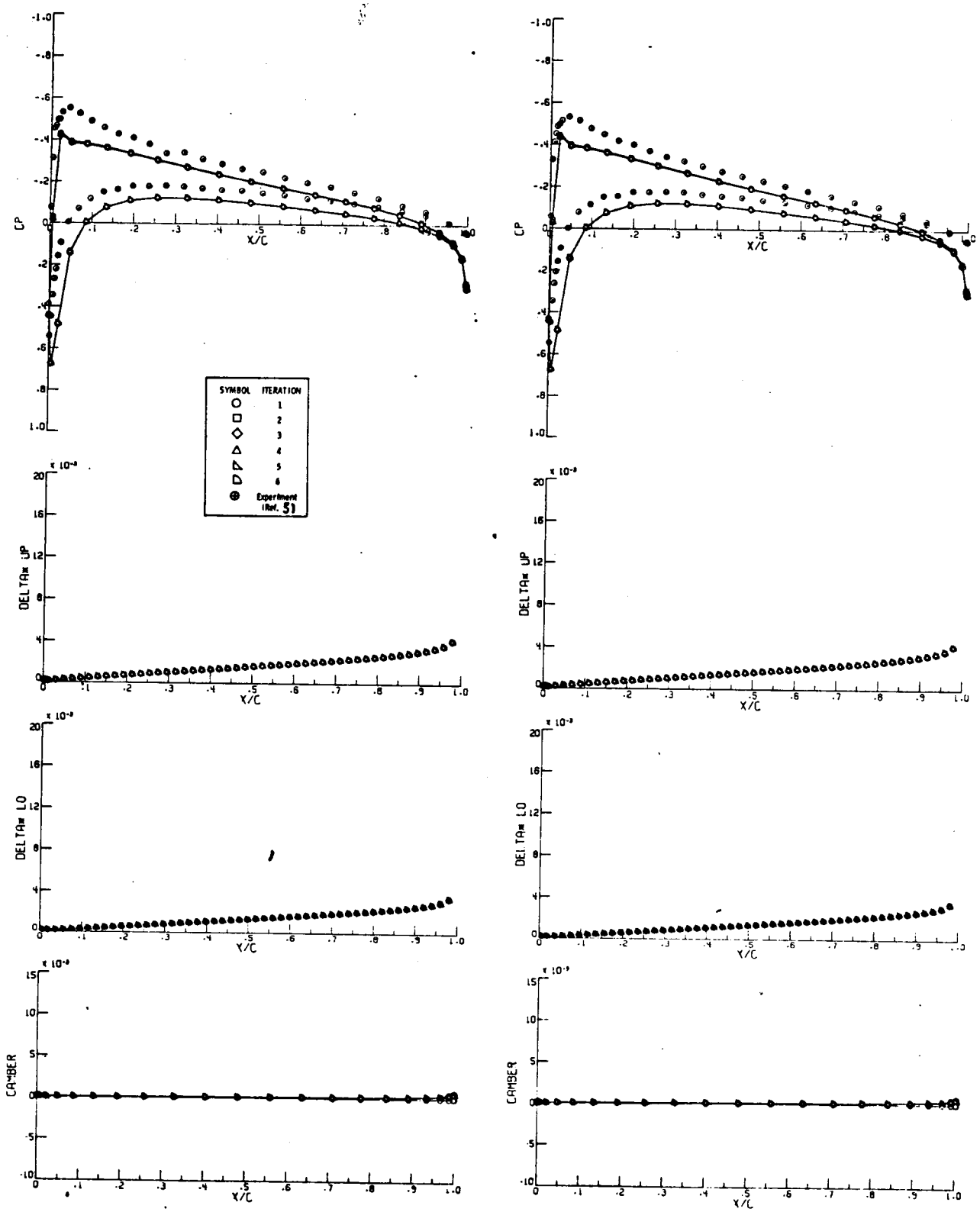

Figure 17. - Pressure distributions, displacement thickness, and camber line developments for five iterations of the strip method. $\Lambda = 40^{o}$, $\alpha = 2.48^{o}$.

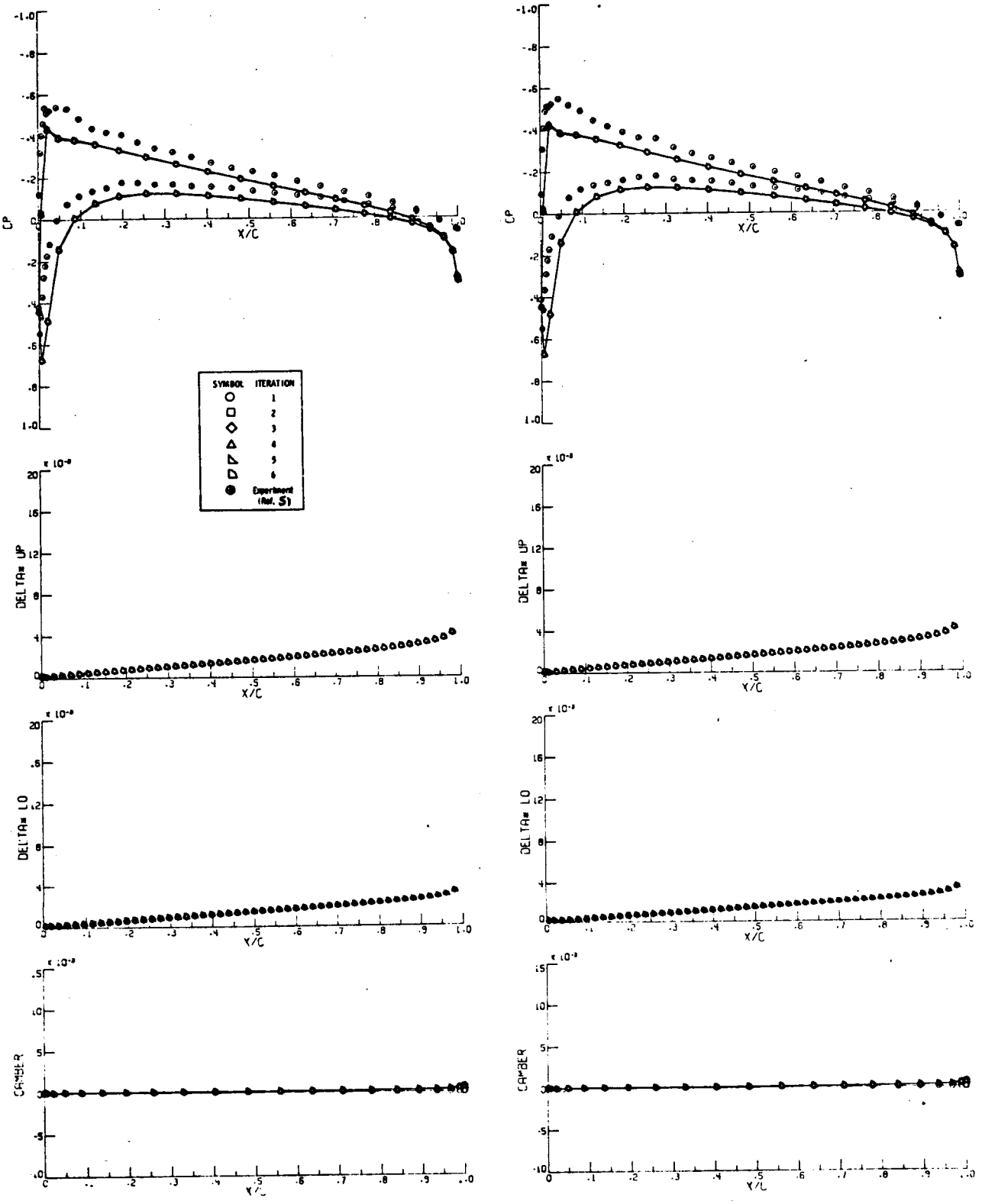

(c) η = .61

(d) η = .72

Figure 17. - Continued.

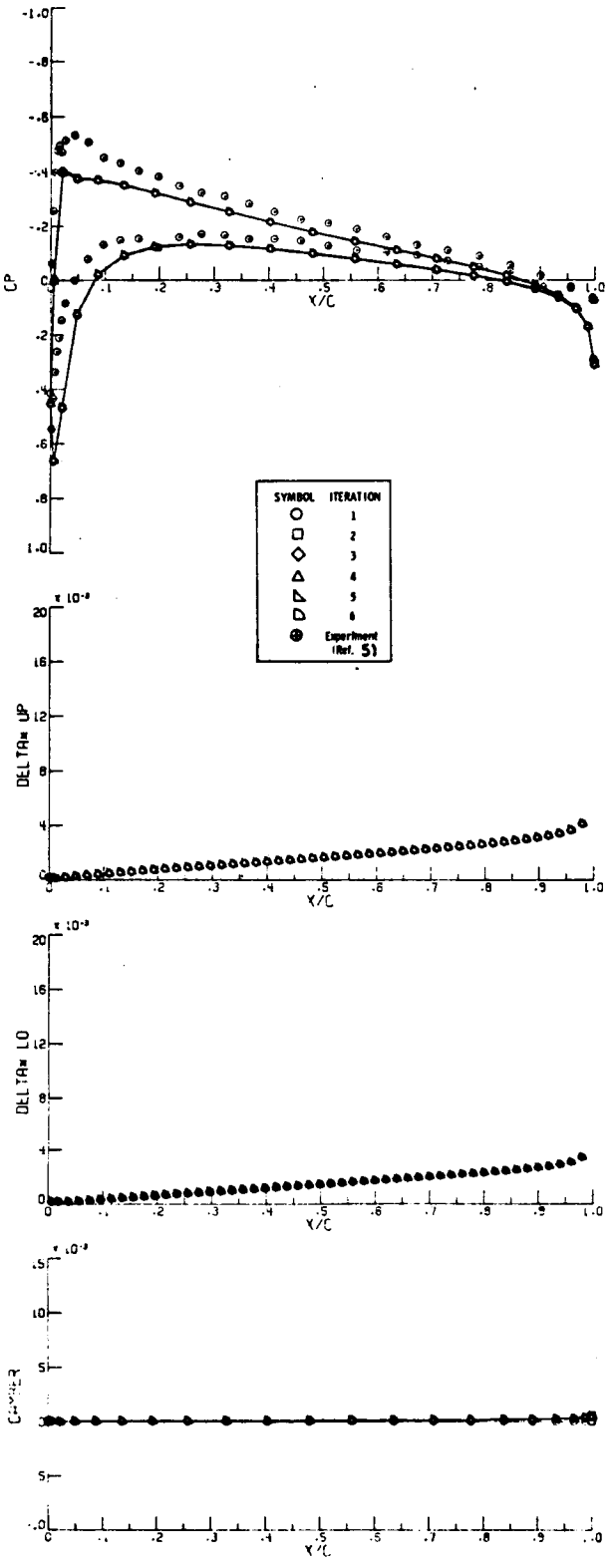

(e) η = .82

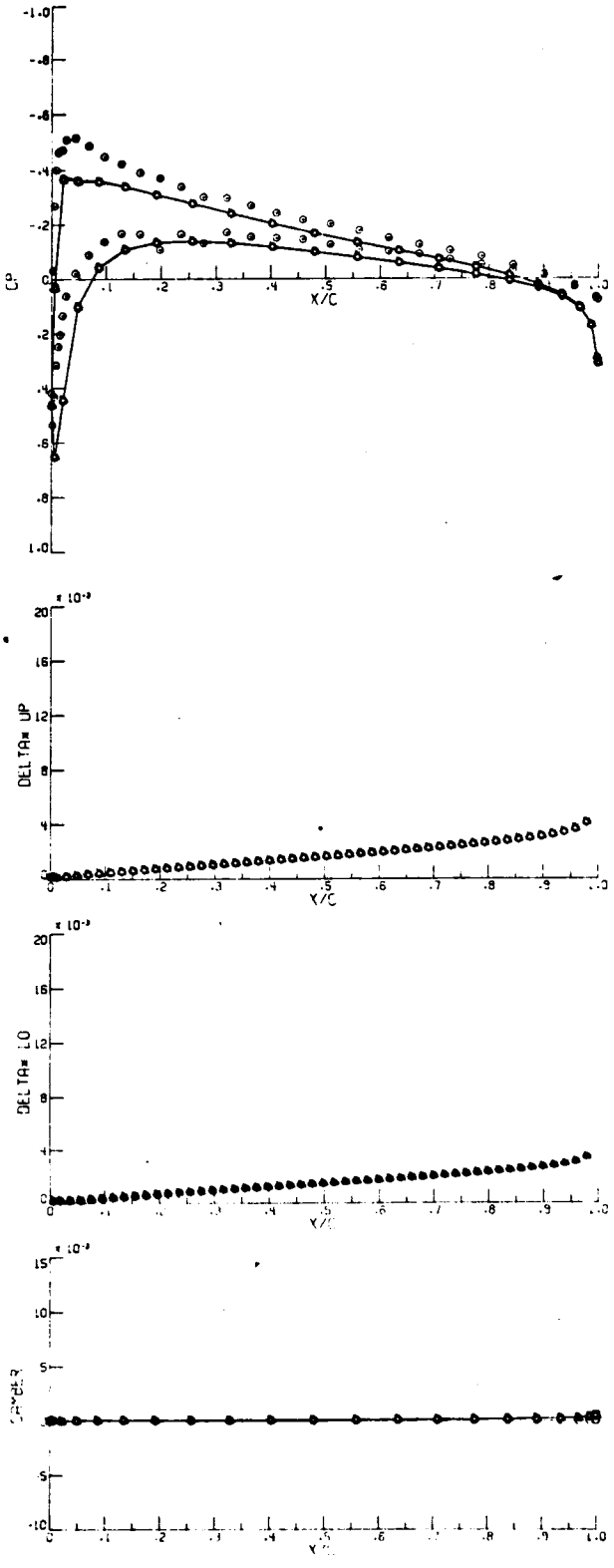

(f) η = .90

Figure 17. - Continued.

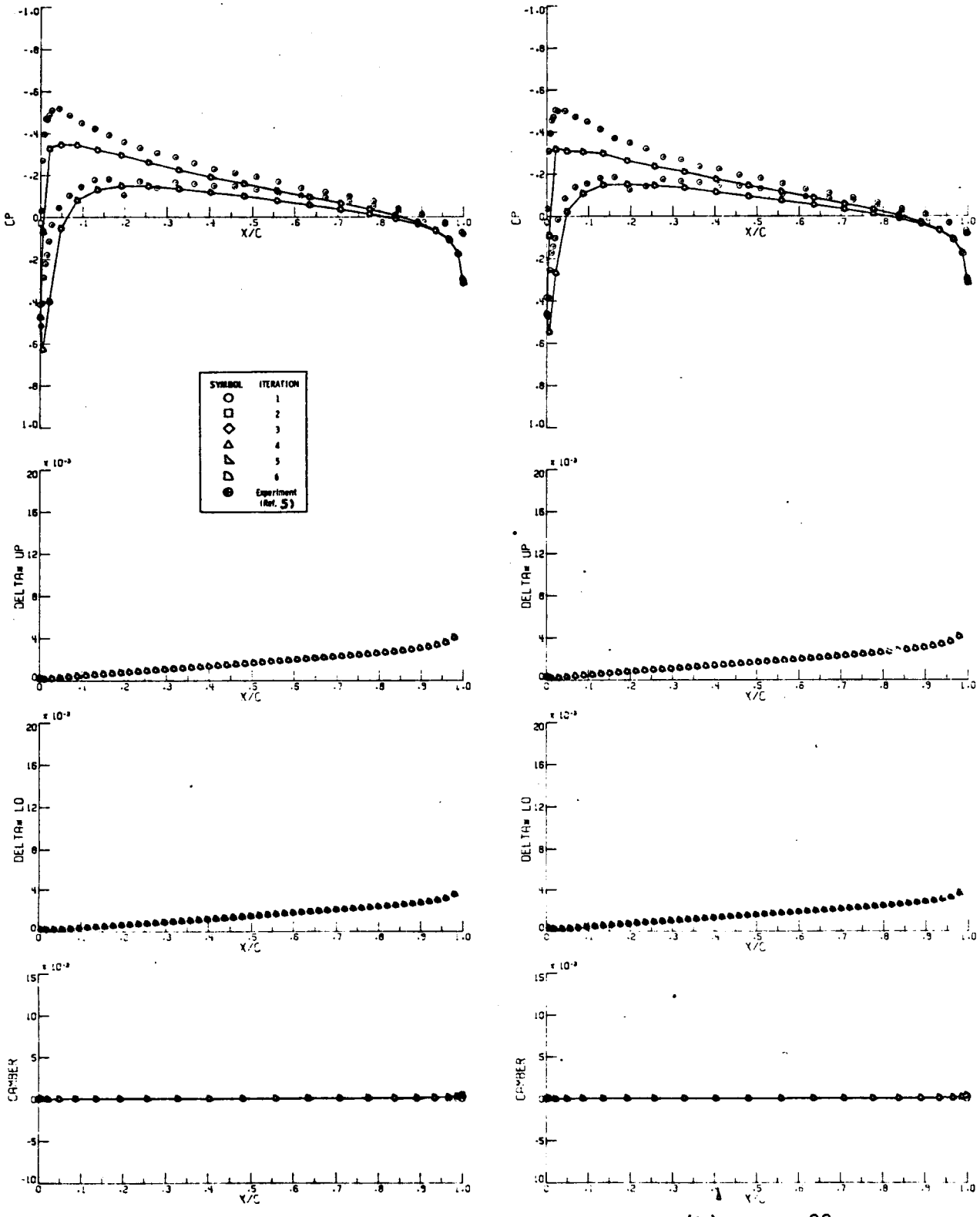

(g) η = .95

(h) η = .99

Figure 17. - Concluded.

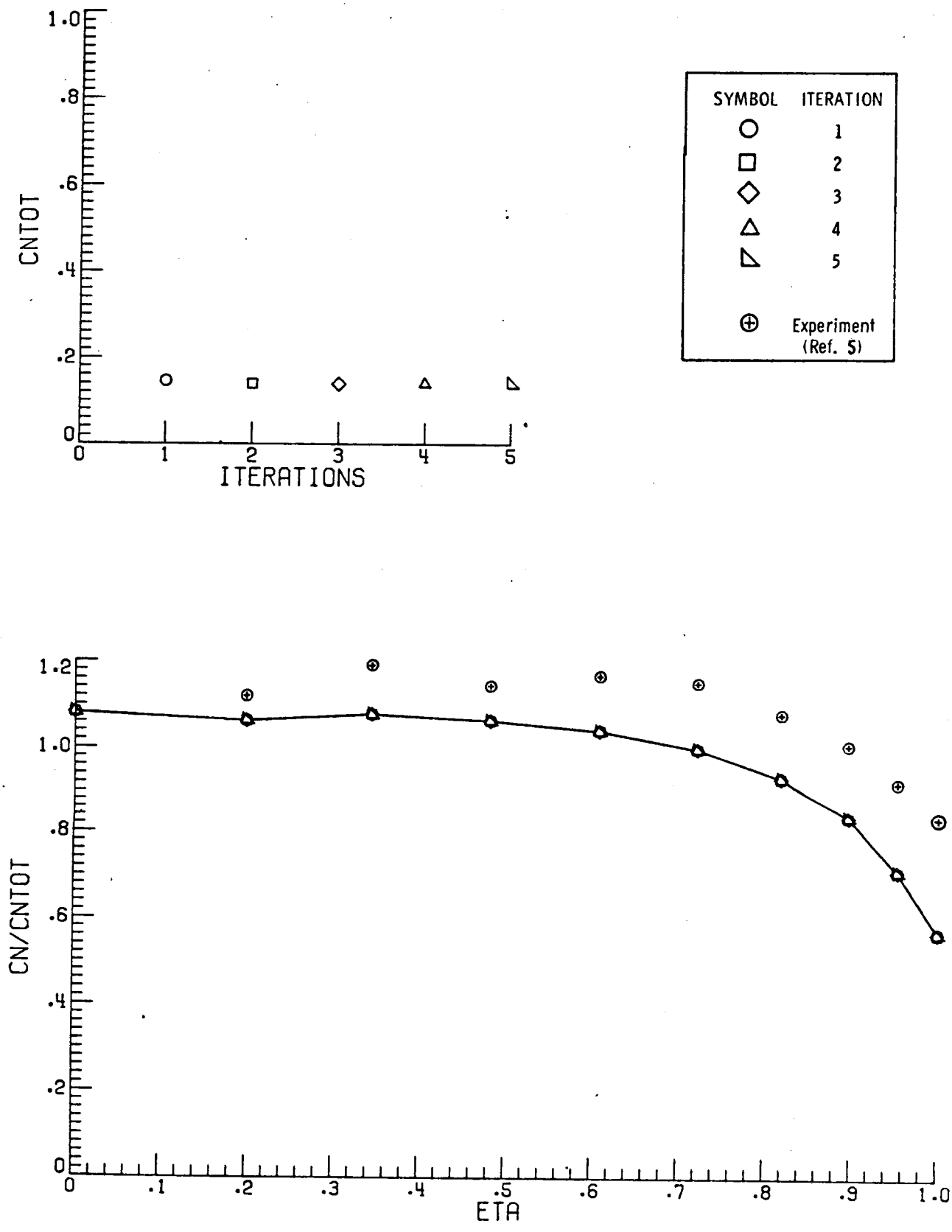

Figure 18. - Total and section normal-force coefficients versus iteration number and semispan station, respectively. $\Lambda = 40^{\circ}$, $\alpha = 2.48^{\circ}$.

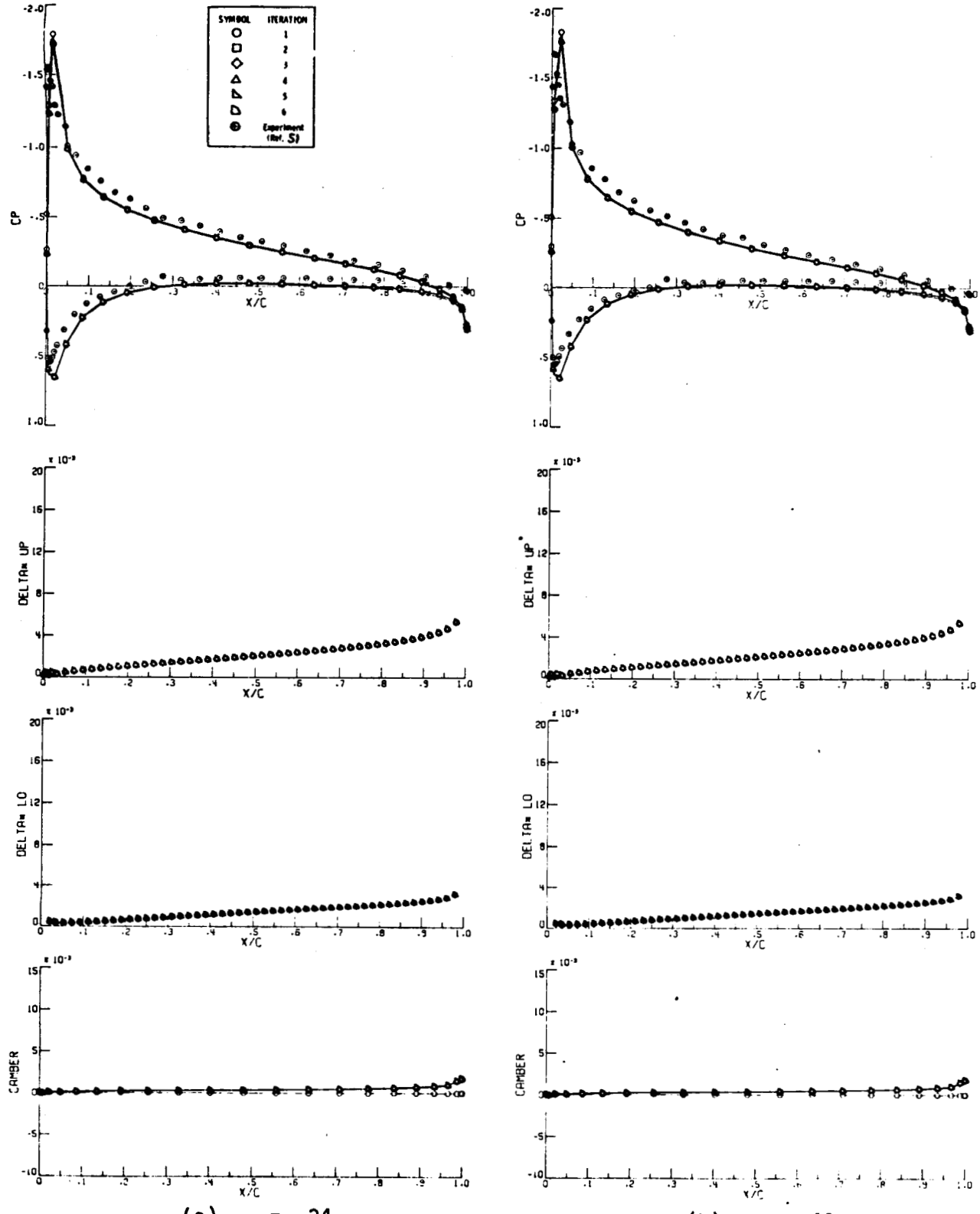

(a) η = .34 (b) η = .48

Figure 19. - Pressure distributions, displacement thickness, and camber line developments for five iterations of the strip method. $\Lambda = 40^{o}$, $\alpha = 6.65^{o}$.

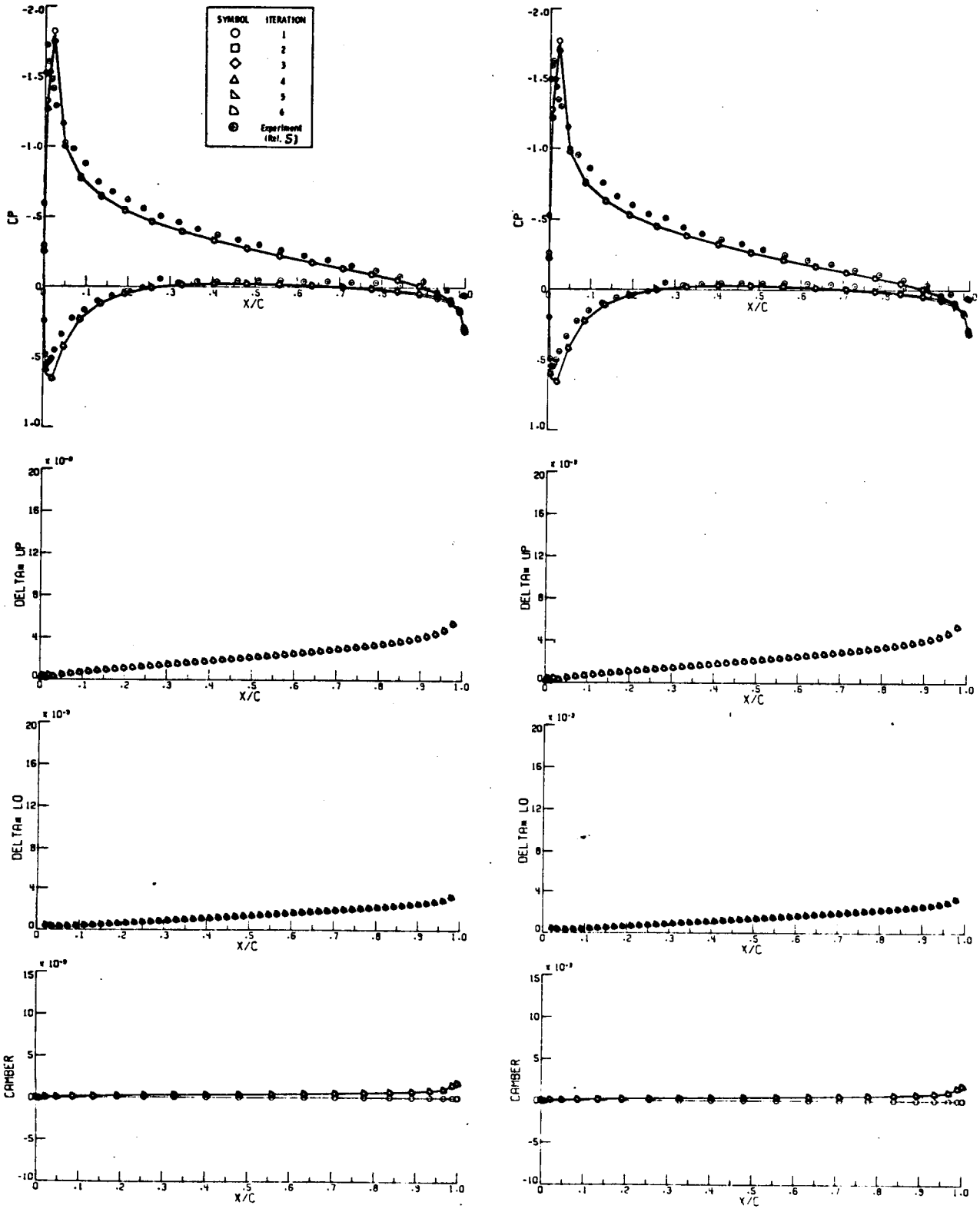

(c) η = .61

(d) η = .72

Figure 19. - Continued.

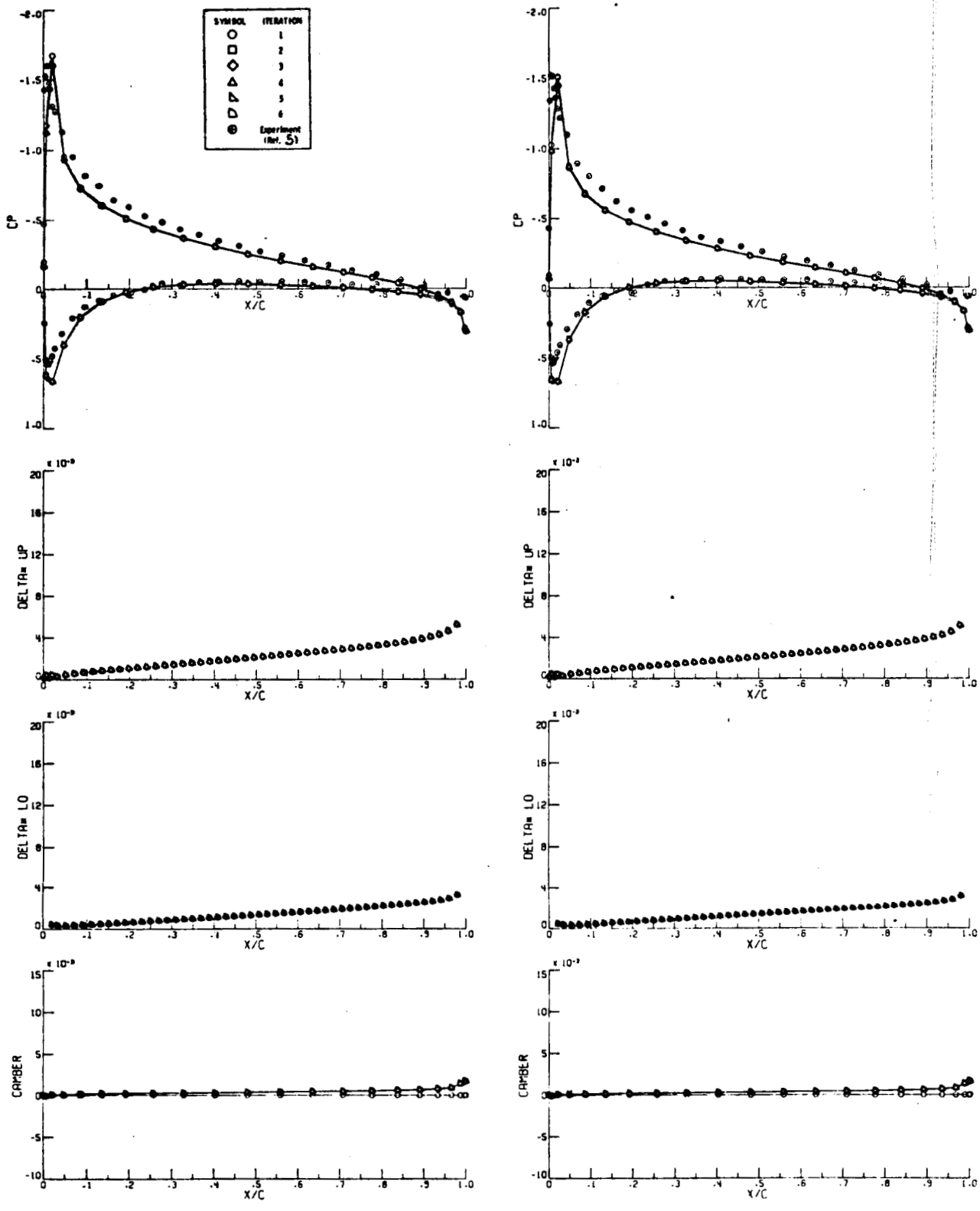

(e) η = .82

(f) η = .90

Figure 19. - Continued.

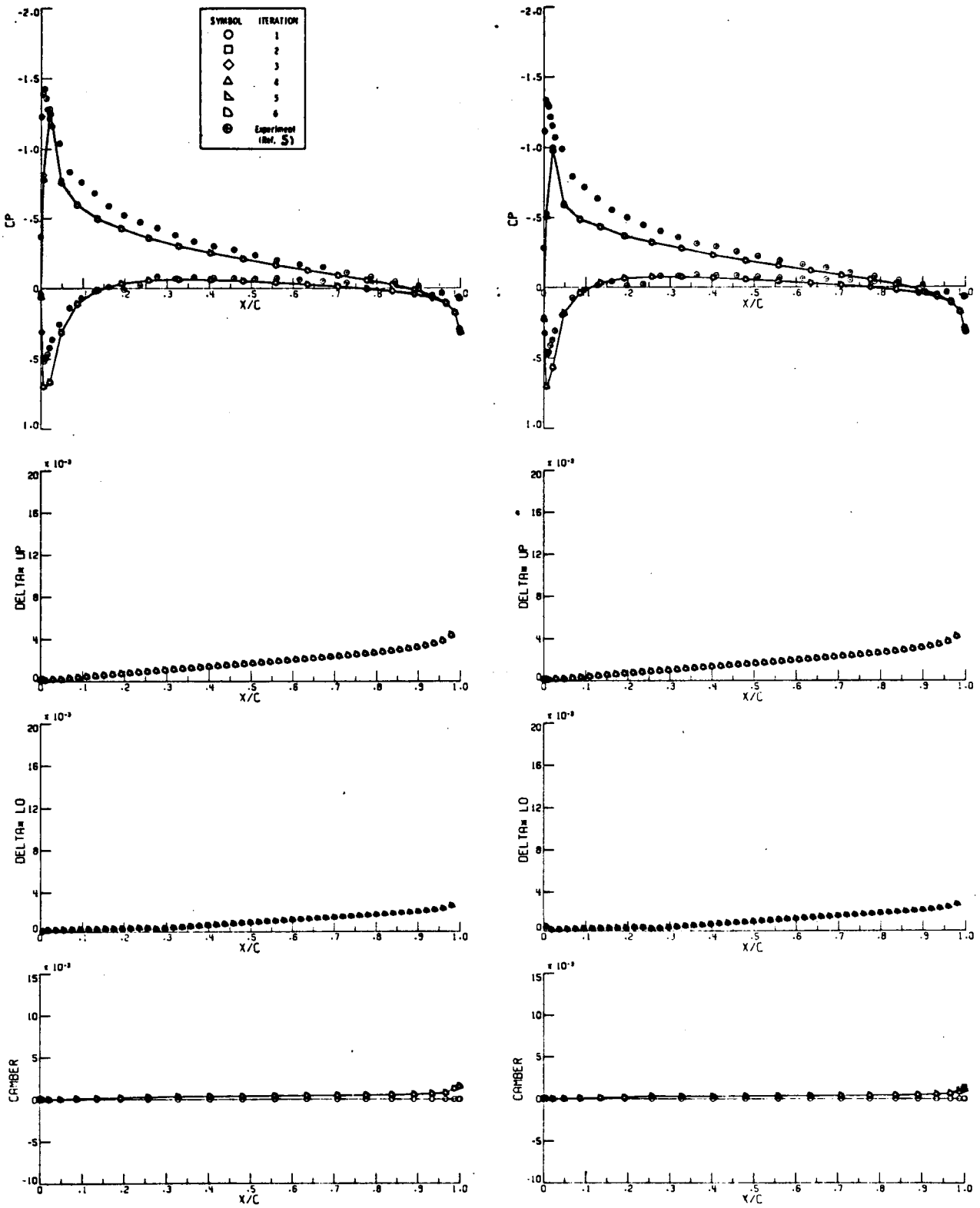

(g) η = .95

(h) η = .99

Figure 19. - Concluded.

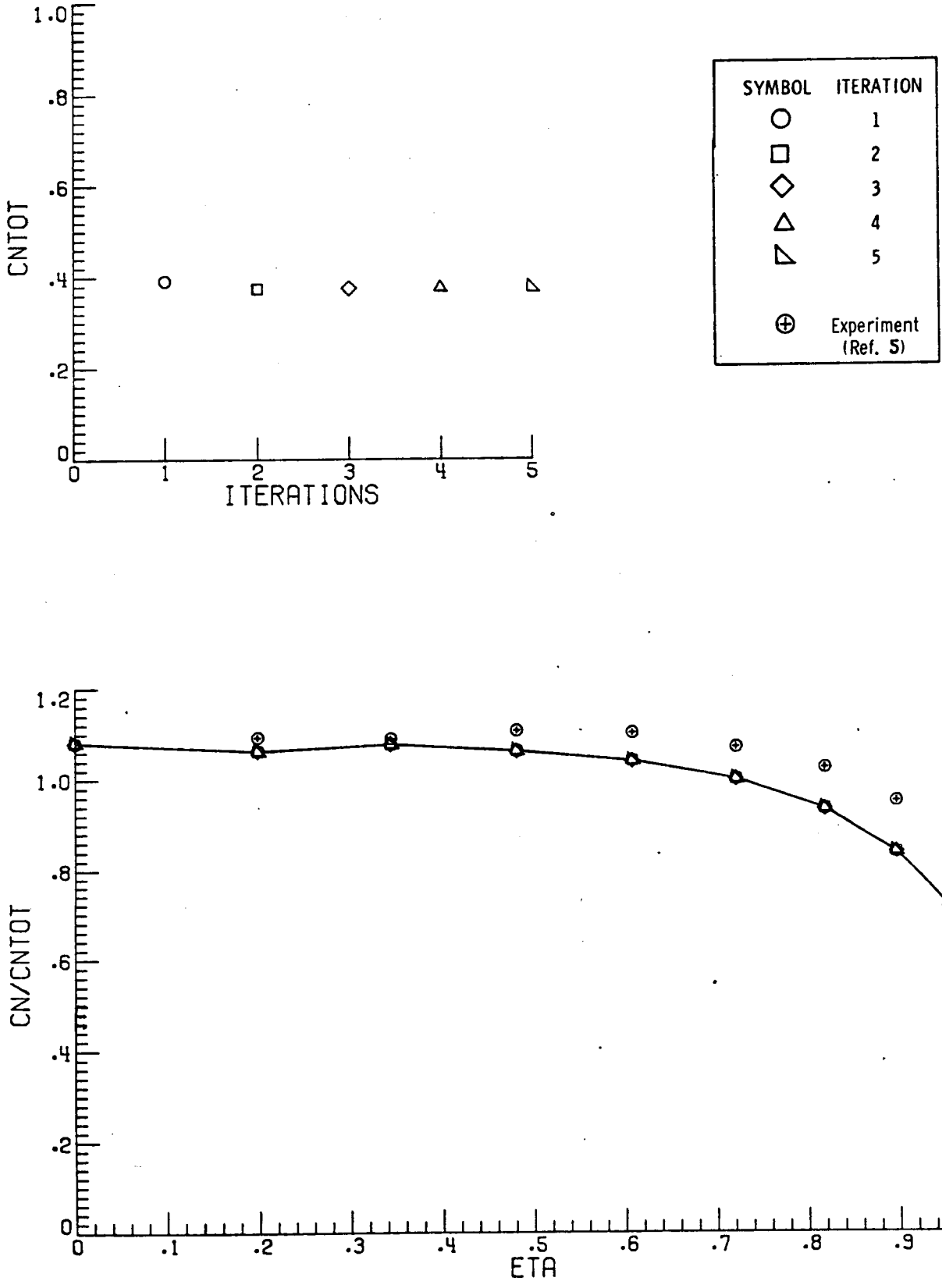

Figure 20. - Total and section normal-force coefficients versus iteration number and semispan station, respectively. $\Lambda = 40^{o}$, $\alpha = 6.65^{o}$.

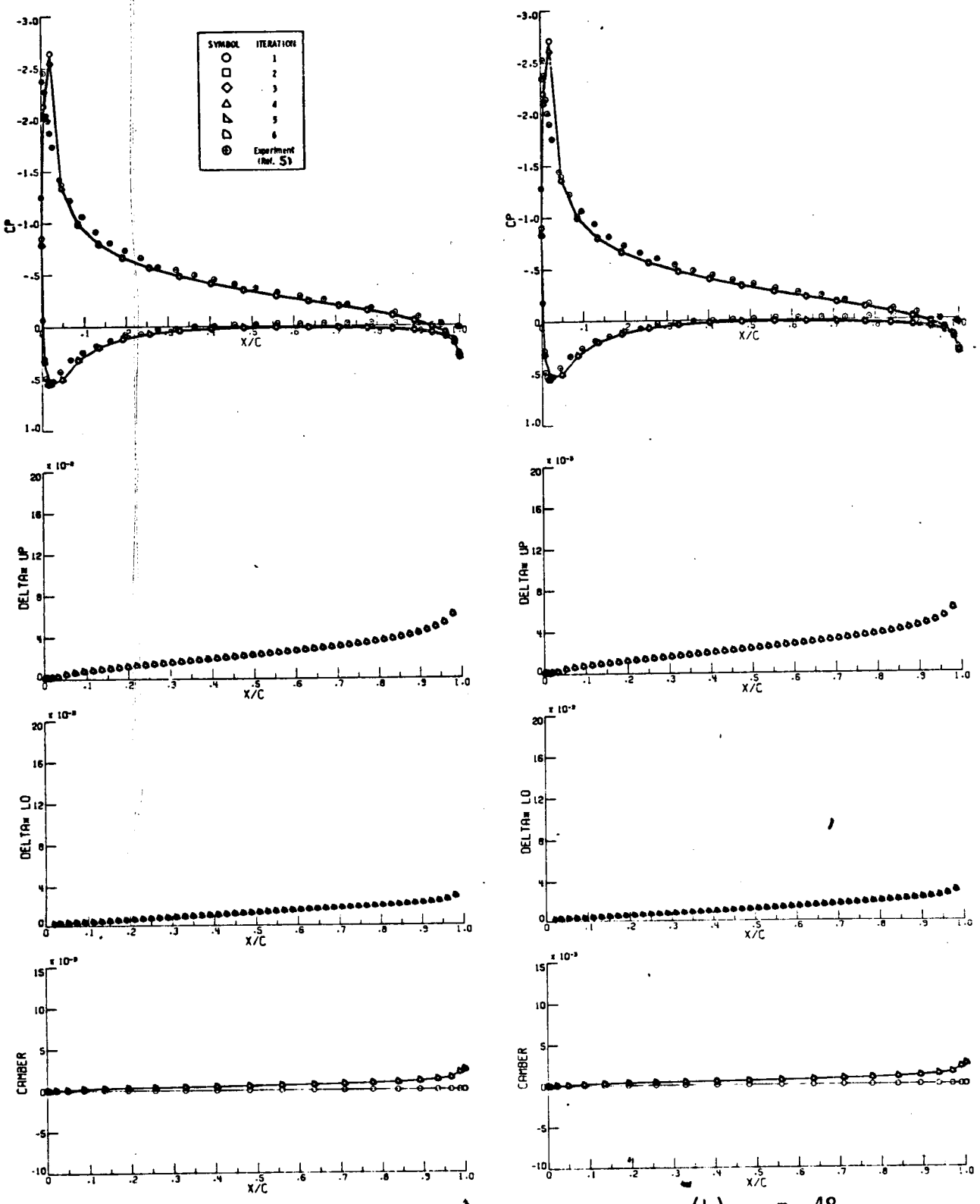

Figure 21. - Pressure distributions, displacement thickness, and camber line developments for five iterations of the strip method. $\Lambda = 40^{\circ}$, $\alpha = 8.73^{\circ}$.

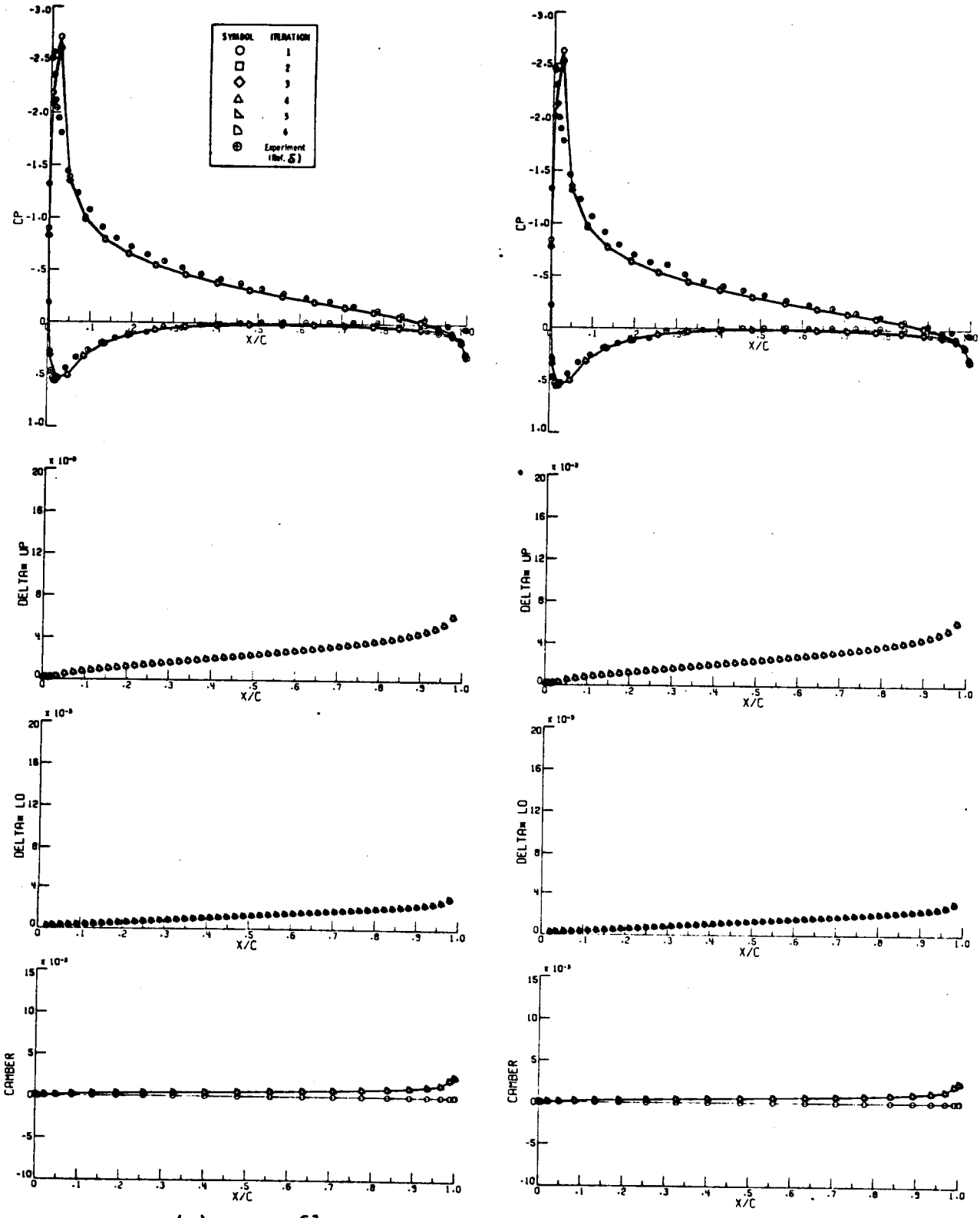

(c) η = .61

(d) η = .72

Figure 21. - Continued.

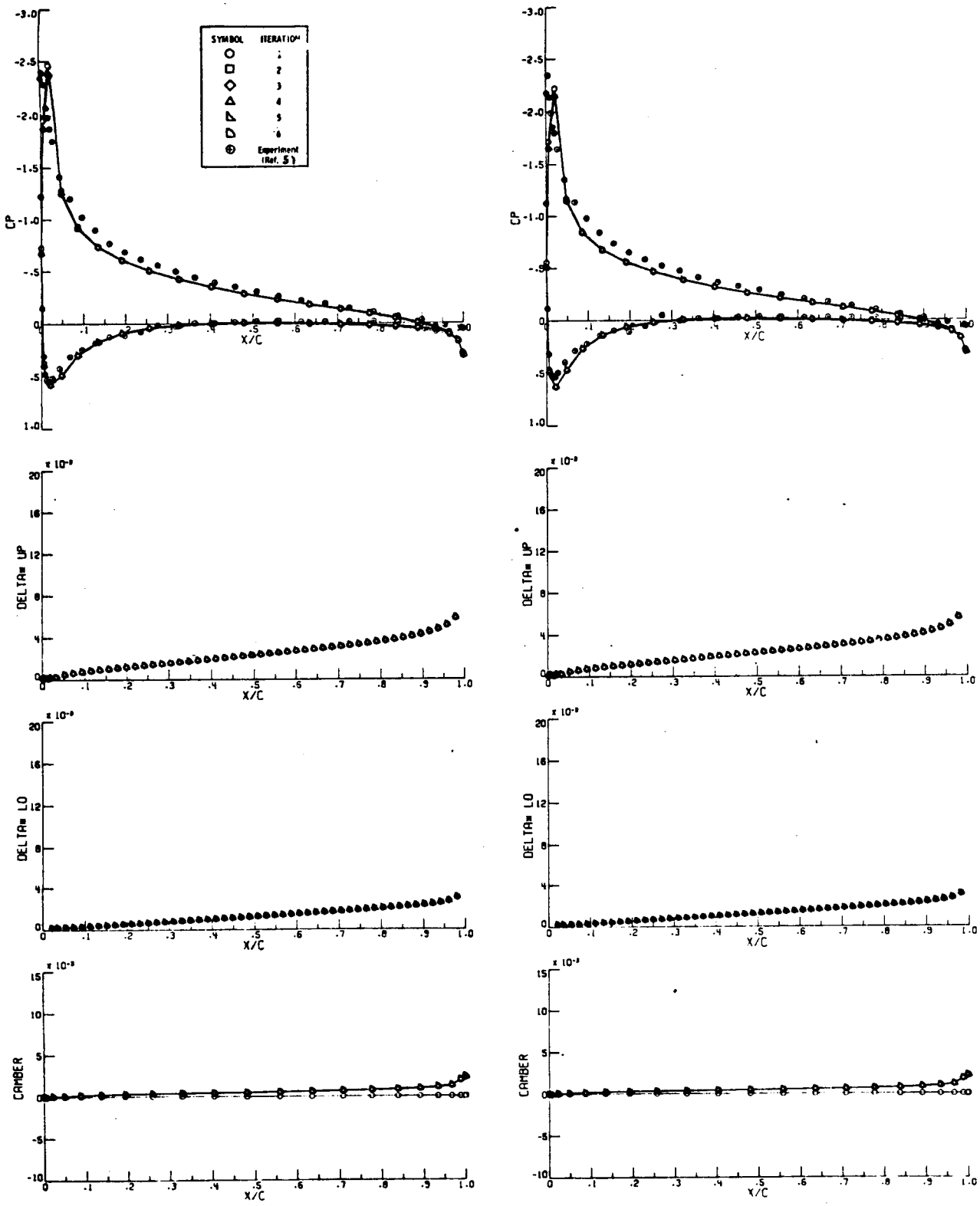

(e) η = .82

(f) η = .90

Figure 21. - Continued.

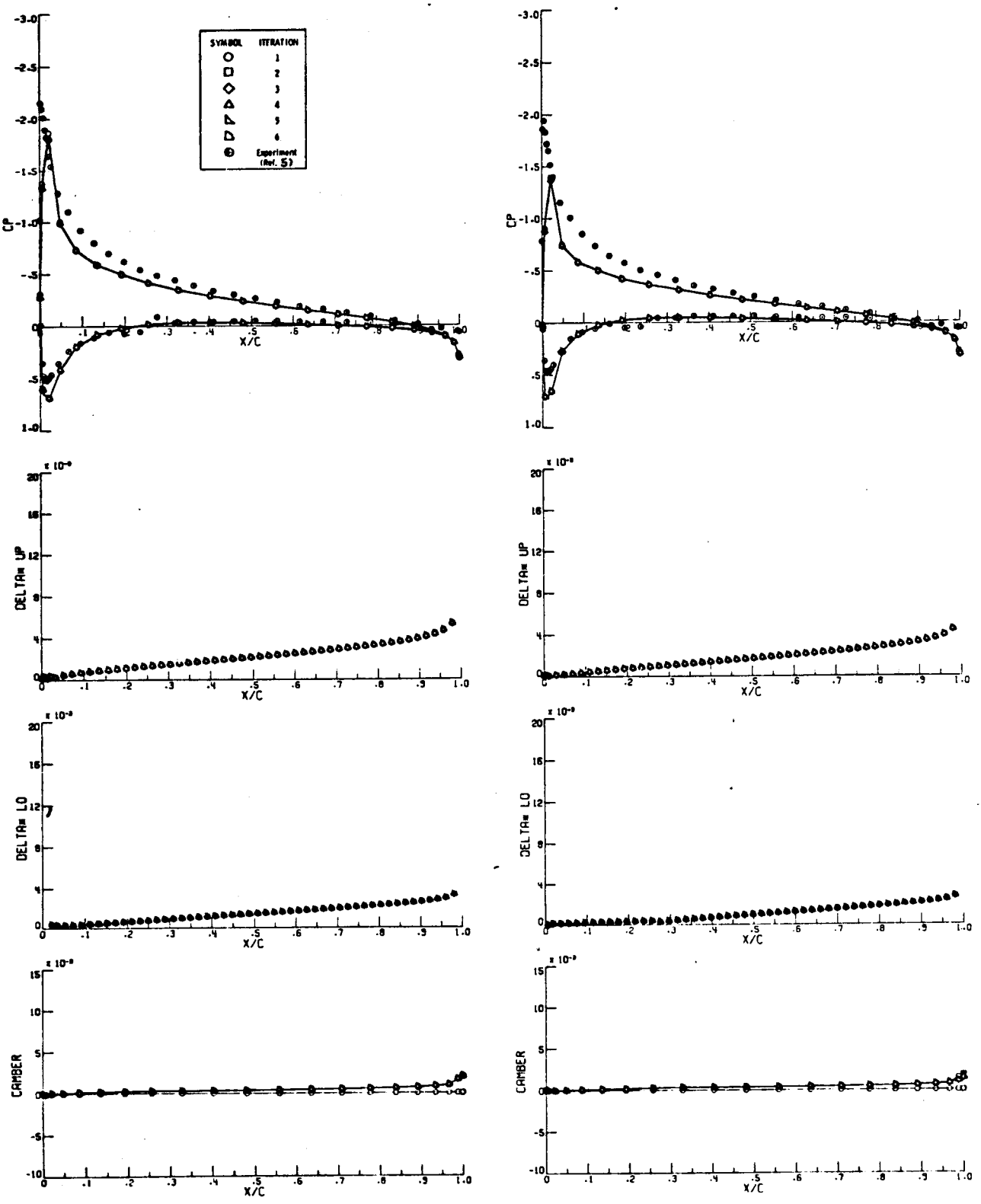

(g) η = .95

(h) η = .99

Figure 21. - Concluded.

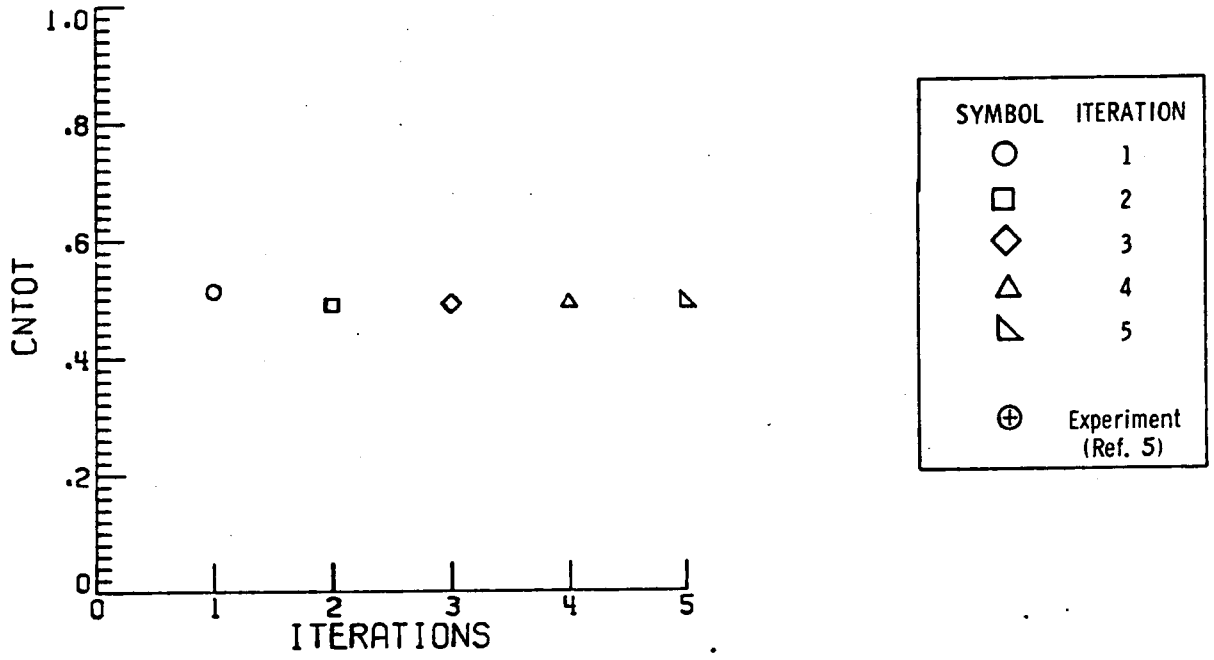

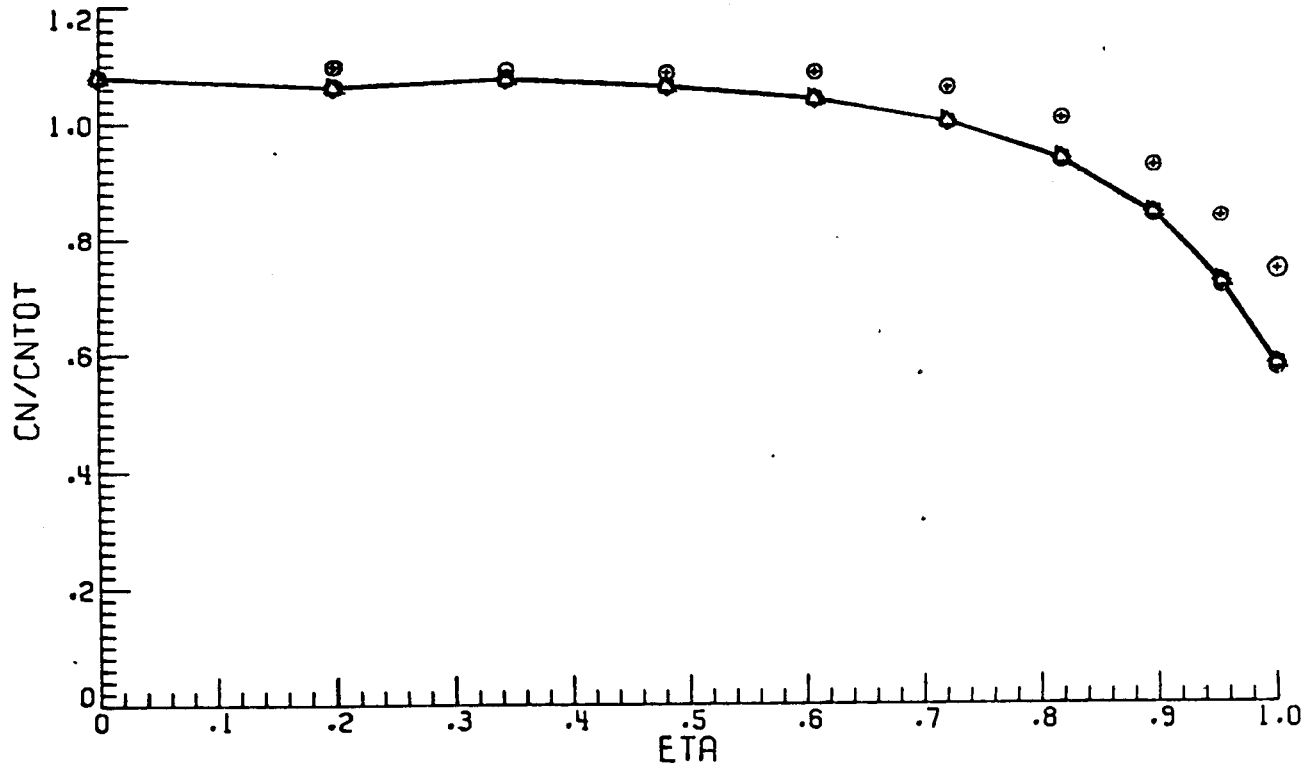

Figure 22. - Total and section normal-force coefficients versus iteration number and semispan station, respectively. $\Lambda = 40^{o}$, $\alpha = 8.73^{o}$.

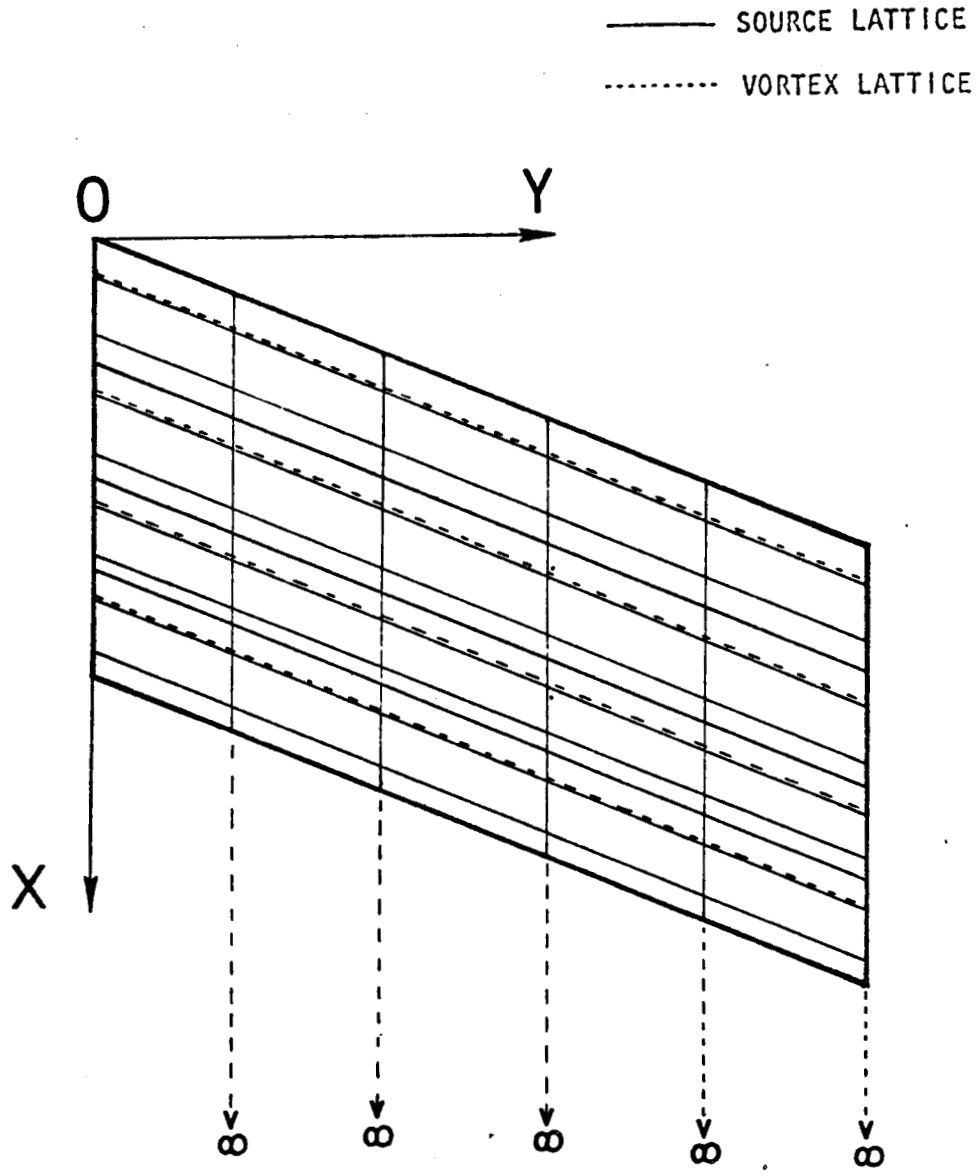

Figure 23. - Wing planform divided into a typical source and vortex-lattice grid.

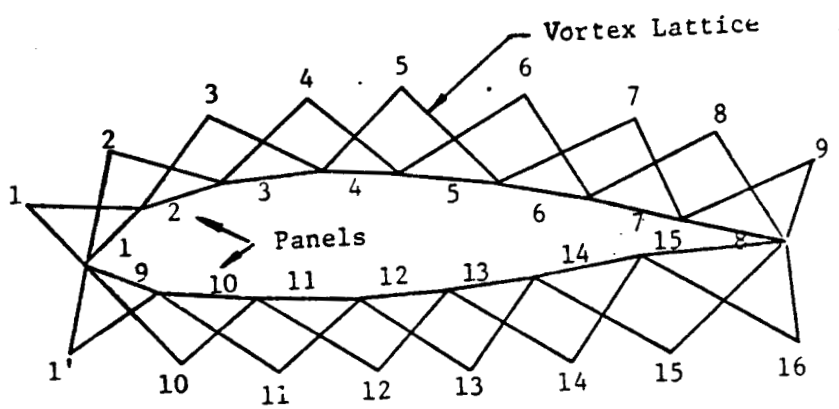

Figure 24. - Vortex distribution on airfoil.